

AD _____

Award Number: W81XWH-04-1-0078

TITLE: Periscopic Spine Surgery

PRINCIPAL INVESTIGATOR: Kevin R. Cleary, Ph.D.

CONTRACTING ORGANIZATION: Georgetown University
Washington, DC 20057

REPORT DATE: June 2008

TYPE OF REPORT: Annual

PREPARED FOR: U.S. Army Medical Research and Materiel Command
Fort Detrick, Maryland 21702-5012

DISTRIBUTION STATEMENT: Approved for Public Release;
Distribution Unlimited

The views, opinions and/or findings contained in this report are those of the author(s) and should not be construed as an official Department of the Army position, policy or decision unless so designated by other documentation.

REPORT DOCUMENTATION PAGE				Form Approved OMB No. 0704-0188	
Public reporting burden for this collection of information is estimated to average 1 hour per response, including the time for reviewing instructions, searching existing data sources, gathering and maintaining the data needed, and completing and reviewing this collection of information. Send comments regarding this burden estimate or any other aspect of this collection of information, including suggestions for reducing this burden to Department of Defense, Washington Headquarters Services, Directorate for Information Operations and Reports (0704-0188), 1215 Jefferson Davis Highway, Suite 1204, Arlington, VA 22202-4302. Respondents should be aware that notwithstanding any other provision of law, no person shall be subject to any penalty for failing to comply with a collection of information if it does not display a currently valid OMB control number. PLEASE DO NOT RETURN YOUR FORM TO THE ABOVE ADDRESS.					
1. REPORT DATE (DD-MM-YYYY) 01-06-2008		2. REPORT TYPE Annual		3. DATES COVERED (From - To) 22 DEC 2006 - 10 MAY 2008	
4. TITLE AND SUBTITLE Periscopic Spine Surgery				5a. CONTRACT NUMBER	
				5b. GRANT NUMBER W81XWH-04-1-0078	
				5c. PROGRAM ELEMENT NUMBER	
6. AUTHOR(S) Kevin R. Cleary, Ph.D. E-Mail: cleary@georgetown.edu				5d. PROJECT NUMBER	
				5e. TASK NUMBER	
				5f. WORK UNIT NUMBER	
7. PERFORMING ORGANIZATION NAME(S) AND ADDRESS(ES) Georgetown University Washington, DC 20057				8. PERFORMING ORGANIZATION REPORT NUMBER	
9. SPONSORING / MONITORING AGENCY NAME(S) AND ADDRESS(ES) U.S. Army Medical Research and Materiel Command Fort Detrick, Maryland 21702-5012				10. SPONSOR/MONITOR'S ACRONYM(S)	
				11. SPONSOR/MONITOR'S REPORT NUMBER(S)	
12. DISTRIBUTION / AVAILABILITY STATEMENT Approved for Public Release; Distribution Unlimited					
13. SUPPLEMENTARY NOTES					
14. ABSTRACT The Periscopic Spine Surgery project was envisioned to lay the ground work for developing the physician assist systems of the future. These systems will incorporate robotics, tracking, and visualization to improve the precision of instrument placement and manipulation in minimally invasive procedures. Key research accomplishments included: 1. Developed a prototype robotic system with force feedback to assist the physician in minimally invasive ultrasound interventions 2. Completed a new rotating needle driver to hold and spin the needle for biopsy procedures under robotic control 3. Developed a control methodology for the rehabilitation arm exoskeleton for modulating shoulder impedance during physical therapy 4. Demonstrated image-guided spinal vertebroplasty in a phantom model using our open source software package IGSTK 5. Completed an evaluation study of electromagnetic tracking in the clinical environment 6. Developed an image-guided system for optimized volumetric treatment planning and execution for radiofrequency ablation of liver tumors 7. Investigated PET/CT guided interventional papers including completing an initial study to evaluate the relative sensitivity of CT versus PET/CT in detecting suspicious lesions					
15. SUBJECT TERMS Minimally invasive procedures, technology development, medical robotics, electromagnetic tracking, workflow, open source software					
16. SECURITY CLASSIFICATION OF:			17. LIMITATION OF ABSTRACT	18. NUMBER OF PAGES	19a. NAME OF RESPONSIBLE PERSON
a. REPORT	b. ABSTRACT	c. THIS PAGE			USAMRMC
U	U	U	UU	103	19b. TELEPHONE NUMBER (include area code)

1 Table of Contents

2	Introduction	5
3	Report Body	5
3.1	Task 1: Needle Driver Robotics	5
3.1.1	Accomplishment 1: Robotically Assisted Ultrasound	5
3.1.2	Accomplishment 2: Rotating Needle Driver.....	7
3.2	Task 2: Rehabilitation Robotics	8
3.2.1	Accomplishment 1: Rehabilitation Arm Exoskeleton	8
3.2.2	Accomplishment 2: Haptic Control Interface	9
3.3	Task 3: Interventional Suite of the Future	9
3.3.1	Accomplishment 1: Open Source Software Package.....	10
3.3.2	Accomplishment 2: Image-Guided Vertebroplasty	11
3.3.3	Accomplishment 3: Abdominal Phantom Evaluation.....	11
3.3.4	Accomplishment 4: Electromagnetic Tracking Evaluation	12
3.3.5	Accomplishment 5: RFA for Liver Tumors.....	13
3.3.6	Accomplishment 6: PET/CT Guided Interventional Procedures	14
3.4	Task 4: Image-Guided Bronchoscopy	15
4	Key Research Outcomes	16
5	Reportable Outcomes	17
6	Conclusions	17
7	References	18
	Appendices (Papers)	20
7.1	Banovac 2007: An image-guided system for	20
7.2	Carignan 2008a: A haptic control interface	23
7.3	Carignan 2008b: Controlling shoulder	30
7.4	Choi 2007: Transbronchial biopsy	37
7.5	Ding 2008a: Accuracy analysis of	41
7.6	Ding 2008b: Robotically assisted ultrasound	49
7.7	Enquobahrie 2007: The image-guided surgery	58
7.8	Lin 2008: Phantom evaluation of an image-guided	72
7.9	Shah 2008: Robotically assisted needle driver:	80
7.10	Wilson 2008: A buyer's guide to	88
7.11	Wong 2007: PET/CT-guided interventional	101

List of Figures

Figure 1: Parallel mechanism robotic device holding ultrasound probe.....	6
Figure 2: Experimental setup with tissue phantom.....	6
Figure 3: Rotating needle driver and remote center of motion.....	7
Figure 4: The MGA Exoskeleton.....	8
Figure 5: Keiser Arm Curl 250 retrofitted with UltraMotion actuator.	9
Figure 6: IGSTK component based architecture.	10
Figure 7: In-vitro experimental setup in the interventional radiology suite.	11
Figure 8: Anthropomorphic phantom and experimental set-up	12
Figure 9: Electromagnetic tracking systems and their components.....	13
Figure 10: CT image of segmented liver tumor.....	14
Figure 11: PET/CT-guided visualization.	15
Figure 12: Wireframe model of EM tracked biopsy forceps	16

2 Introduction

This project is aimed at improving the state of the art of image-guided and minimally invasive procedures by developing a new generation of clinical techniques along with the computer-based hardware and software needed for their implementation. The focus of the project is to develop physician assist systems incorporating robotics, tracking, and visualization to improve the precision of instrument placement and manipulation in minimally invasive procedures. This goal is accomplished through a technology development process starting with phantom studies, then proceeding to animal studies, followed by the ultimate aim of human clinical trials.

The project is led by the Imaging Sciences and Information Systems (ISIS) Center of the Department of Radiology at Georgetown University. Project collaborators include the Department of Radiation Medicine at Georgetown, the Urology Robotics Group at Johns Hopkins Medical Institutions, the NSF sponsored Engineering Research Center for Computer Integrated Surgical Systems and Technology at Johns Hopkins University, and the Engineering School at the Catholic University of America, as well as several commercial collaborators. Commercial collaborators include Kitware Inc., ASI Instruments Inc., and Siemens Medical Systems. The funds provided under the research are leveraged with funds from other research supporters to create a synergistic environment for advancement of these techniques.

3 Report Body

This section describes the research accomplishments associated with each of the tasks in the statement of work. A brief overview will be given and the reader will be referred to the published papers in the appendix for more details. This is an annual report and includes research performed from December 21, 2006 to December 20, 2007. The award number is W81XWH-04-1-0078.

3.1 Task 1: Needle Driver Robotics

There were two major accomplishments during the last reporting period:

- 1) The development of a prototype system for robotically assisted ultrasound [Ding 2008b]
- 2) The addition of a rotating needle driver to the existing robotic platform from Johns Hopkins [Shah 2008]

3.1.1 Accomplishment 1: Robotically Assisted Ultrasound

The first major accomplishment was the development of a prototype robotic system to assist the physician in minimally invasive ultrasound interventions. In current practice, the physician must manually hold the ultrasound probe in one hand and manipulate the needle with the other hand, which can be challenging, particularly when trying to target small lesions. To assist the physician, the robot should not only be capable of providing the spatial movement needed, but also be able to control the contact force between the ultrasound probe and patient. To meet these requirements, we are developing a prototype

system based on an existing six degree of freedom parallel robot previously developed by Dr. Cleary. The system will provide high bandwidth, precision motion, and force control. Some results from this project are shown in Figures 1 and 2 and more details can be found in [Ding 2008b].



Figure 1: Parallel mechanism robotic device holding ultrasound probe

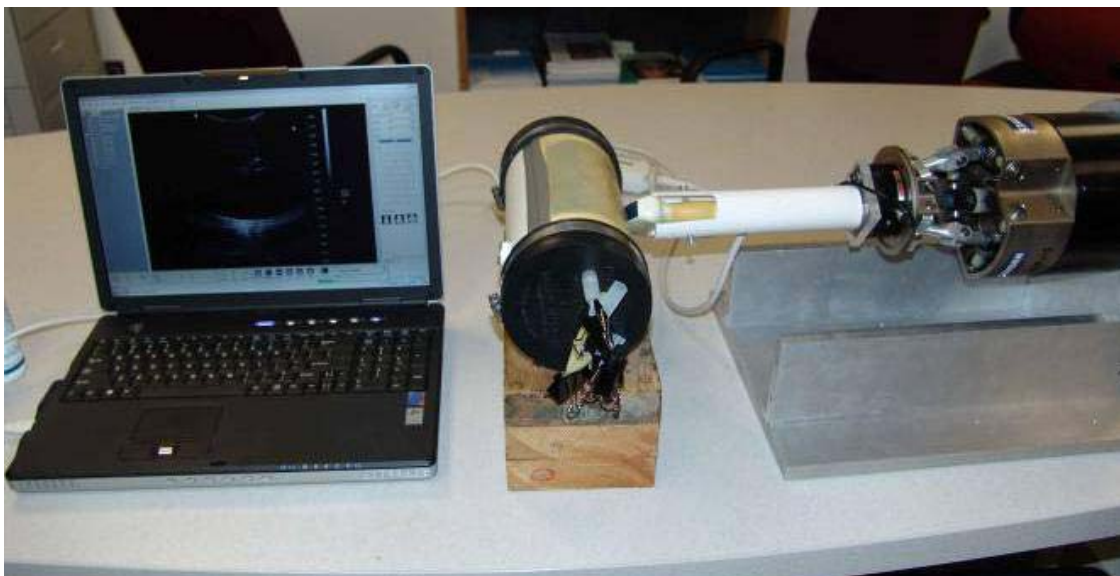


Figure 2: Experimental setup with tissue phantom (ultrasound image can be vaguely seen on laptop)

3.1.2 Accomplishment 2: Rotating Needle Driver

The second major accomplishment was the development of a rotating needle driver for the Johns Hopkins robotic system. The robotic system was an updated version of the “AcuBot” system built by the Urology Robotics Laboratory at Johns Hopkins Medical Institutions. The original AcuBot comprises the “PAKY” (Percutaneous Access of the KidneY) needle driver, the “RCM” (Remote Center of Motion) orientation module, and joystick control. A three degree of freedom Cartesian stage, passive positioning S-arm, and “bridge frame” enable the system to achieve a compact and flexible design for interventions at multiple points along the body.

Prior experiences using the AcuBot system in clinical trials for spinal nerve blocks showed the need for some system enhancements. The main focus of these enhancements was a complete redesign of the needle driver. Three new components were added to the needle driver: (1) a mechanism to spin the needle, (2) force sensors, and (3) a needle release mechanism. A picture is shown in Figure 3 and details are given in [Shah 2008].

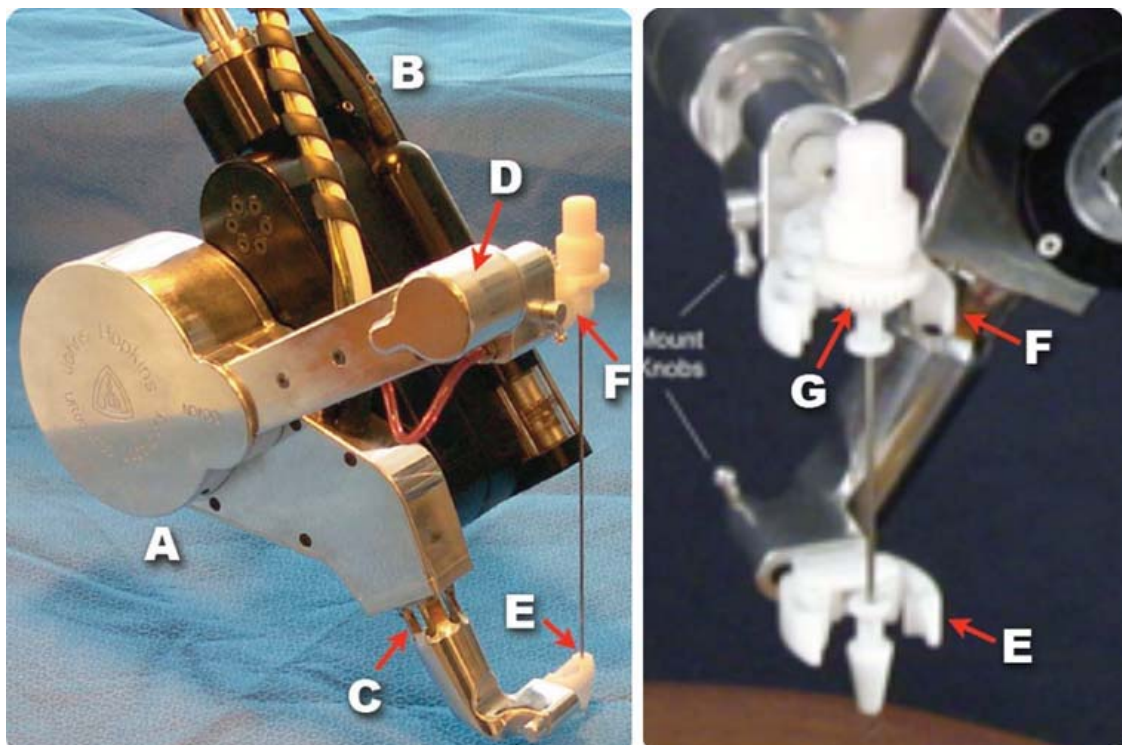


Figure 3: (left) Rotating needle driver (RND), b Remote center of motion (RCM) orientation module. c/d Force sensor, e/f Head and Barrel grippers, g Needle hub

3.2 Task 2: Rehabilitation Robotics

There were two major accomplishments during the last reporting period:

- 1) Continued development of a rehabilitation arm exoskeleton [Carignan 2008a]
- 2) Development of a haptic control interface for a motorized exercise machine [Carignan 2008b]

3.2.1 Accomplishment 1: Rehabilitation Arm Exoskeleton

For the rehabilitation arm exoskeleton (Figure 4), a control methodology was developed for modulating shoulder impedance during physical therapy. Setting the remote center of compliance at the shoulder allows the exoskeleton to enact resistance training protocols that strengthen the rotator cuff and other joint musculature supporting the shoulder complex. The rotational kinematics for the shoulder were derived, and then the torques applied at the shoulder were estimated using force sensors placed at the hand and elbow interfaces. Impedance and admittance control schemes were both developed for realizing isolateral strengthening exercises, and some preliminary experimental results were presented for implementation [Carignan 2008a].



Figure 4: The MGA Exoskeleton has five powered joints including a three-axis intersecting shoulder and a scapula elevation joint

3.2.2 Accomplishment 2: Haptic Control Interface

For the haptic interface (Figure 5), a powered arm curl machine for modulating resistance “on-the-fly” during strength training and rehabilitation was modified. Force signals from a load cell were input to an impedance loop based on the desired resistance law, which then outputs position commands to a servomotor. The kinematics between the actuator drive and arm curl angle were derived, and the admittance control implementation used for realizing the resistance laws were described. Preliminary experimental results were presented for viscous and inertial control laws [Carignan 2008b].



Figure 5: Keiser Arm Curl 250 retrofitted with UltraMotion actuator

During the last reporting period, dedicated funding for this task was obtained under Army grant W81XWH-08-2-0010, so this task will no longer be reported under this contract in future reports.

3.3 Task 3: Interventional Suite of the Future

This task was the focus of much of the work on this grant during the last reporting period. Here we report on the following accomplishments:

- 1) The continued development of our open source software package the image-guided surgery toolkit IGSTK [Enquobahrie 2007]
- 2) Demonstration of image-guided vertebroplasty using this software on a phantom spine model [Ding 2008a]

- 3) Abdominal phantom evaluation using this software and a custom torso phantom [Lin 2008]
- 4) Evaluation of electromagnetic tracking in several clinical environments [Wilson 2008]
- 5) Development of an image-guided system for treatment planning and navigation for radiofrequency ablation of liver tumors [Banovac 2007]
- 6) Performed studies to form a rationale for PET/CT-guided interventional procedures and assess relative benefits [Wong 2007]

3.3.1 Accomplishment 1: Open Source Software Package

IGSTK is an open source C++ software library that provides the basic components needed to develop image-guided surgery applications [Enquobahrie 2007]. It is intended for fast prototyping and development of image-guided surgery applications. The toolkit was developed through collaboration between academic and industry partners. Because IGSTK was designed for safety-critical applications, the development team has adopted lightweight software processes that emphasizes safety and robustness while, at the same time, supporting geographically separated developers. A software process that is philosophically similar to agile software methods was adopted emphasizing iterative, incremental, and test driven development principles. Realizing that the continued success and viability of an open source toolkit depends on a strong user community, the IGSTK team is following several key strategies to build an active user community. These include maintaining a users and developers' mailing list, providing documentation (application programming interface reference document and book), presenting demonstration applications, and delivering tutorial sessions at relevant scientific conferences.

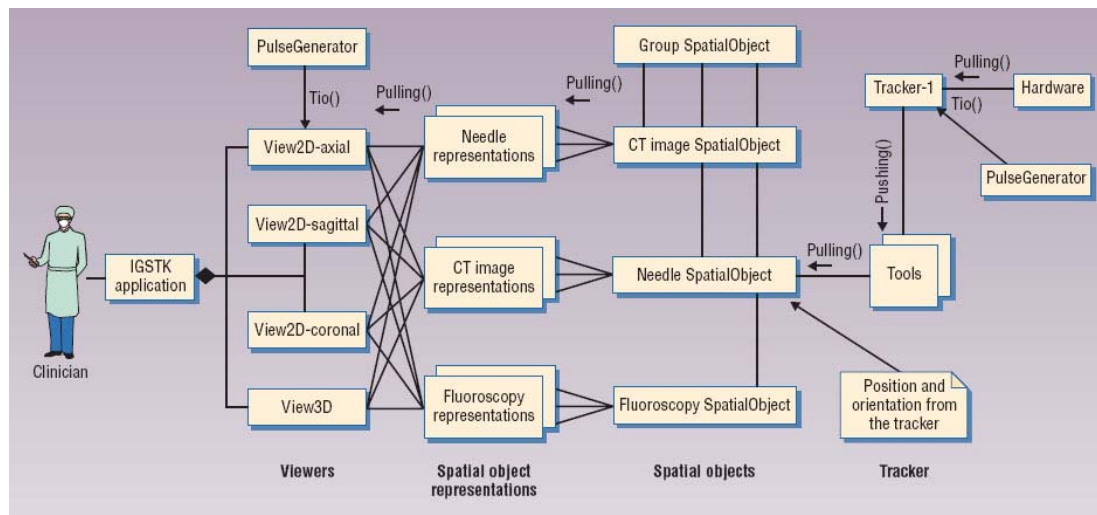


Figure 6: IGSTK component based architecture

3.3.2 Accomplishment 2: Image-Guided Vertebroplasty

The IGSTK software was used to conduct phantom experiments for vertebroplasty spinal therapy based on electromagnetic tracking of instruments in the interventional suite [Ding 2008a]. Vertebroplasty is a minimally invasive procedure in which bone cement is pumped into a fractured vertebral body that has been weakened by osteoporosis, long-term steroid use, or cancer. In this therapy, a trocar (large bore hollow needle) is inserted through the pedicle of the vertebral body which is a narrow passage and requires great skill on the part of the physician to avoid going outside of the pathway. In clinical practice, this procedure is typically done using 2D X-ray fluoroscopy. To investigate the feasibility of providing 3D image guidance, we developed an image-guided system based on electromagnetic tracking and our open source software platform the Image-Guided Surgery Toolkit (IGSTK). The system includes path planning, interactive 3D navigation, and dynamic referencing. The experimental setup is shown in Figure 7.



Figure 7: In-vitro experimental setup in the interventional radiology suite

3.3.3 Accomplishment 3: Abdominal Phantom Evaluation

Based on the work described above, we conducted two abdominal phantom studies (Figure 8) using our navigation system in a clinical environment [Lin 2008]. In the first study, a physician and medical resident performed a total of 18 targeting passes in the abdomen of an anthropomorphic phantom based solely upon image guidance. The distance between the target and needle tip location was measured based on confirmatory

scans which gave an average of 3.56 mm. In the second study, three foam nodules were placed at different depths in a gelatin phantom. Ten targeting passes were attempted in each of the three depths. Final distances between the target and needle tip were measured which gave an average of 3.00 mm. In addition to these targeting studies, we described our refinement to the standard four-quadrant image-guided navigation user interface, based on clinician preferences. We believe these refinements increase the usability of our system while decreasing targeting error.

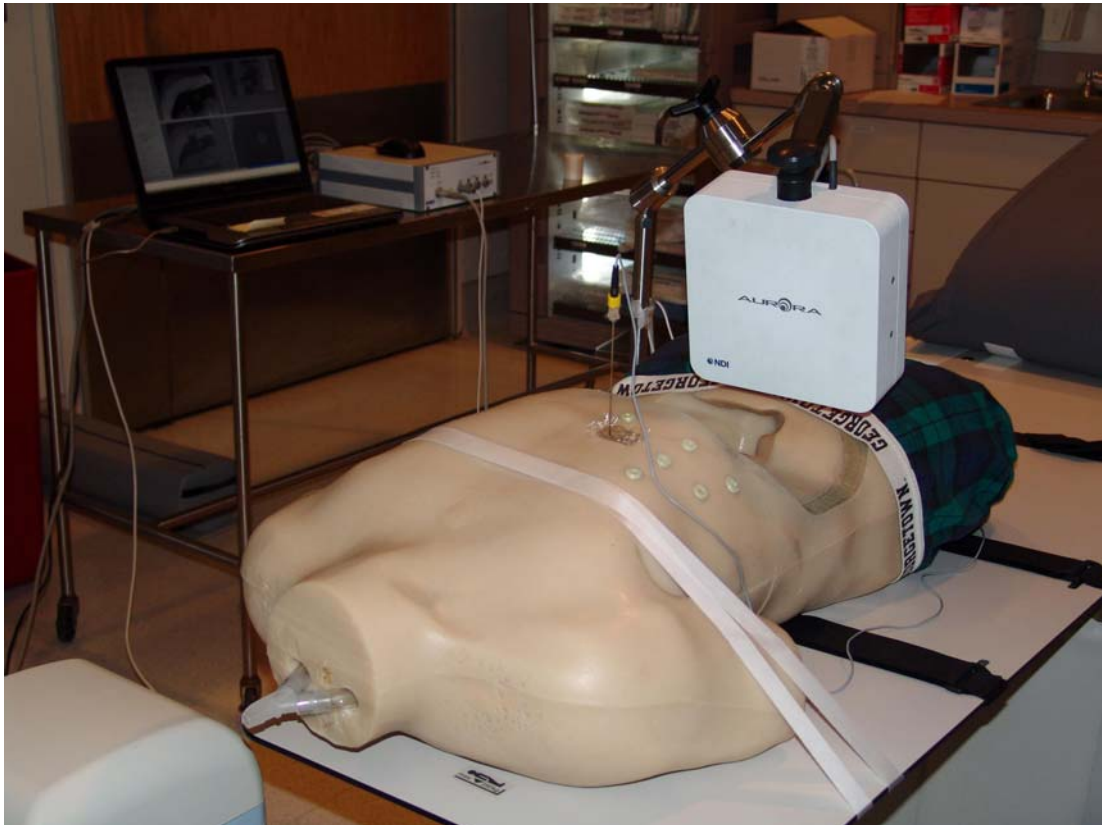


Figure 8: Anthropomorphic phantom and experimental set-up (phantom constructed by Dan Stoianovici, URobotics Laboratory, Johns Hopkins University)

3.3.4 Accomplishment 4: Electromagnetic Tracking Evaluation

As part of our research program, we conducted an evaluation of electromagnetic tracking in several clinical environments [Wilson 2008]. When choosing an Electromagnetic Tracking System (EMTS) for image-guided procedures, it is desirable for the system to be usable for different procedures and environments. Several factors influence this choice. To date, the only factors that have been studied extensively, are the accuracy and the susceptibility of electromagnetic tracking systems to distortions caused by ferromagnetic materials. In this paper we provide a holistic overview of the factors that should be taken into account when choosing an EMTS. These factors include: the system's refresh rate, the number of sensors that need to be tracked, the size of the

navigated region, system interaction with the environment, can the sensors be embedded into the tools and provide the desired transformation data, and tracking accuracy and robustness. We evaluated the Aurora EMTS (Northern Digital Inc., Waterloo, Ontario, Canada) and the 3D Guidance EMTS with the flat-panel and the short-range field generators (Ascension Technology Corp., Burlington, Vermont, USA) in three clinical environments. We showed that these systems are applicable to specific procedures or in specific environments, but that, no single system is currently optimal for all environments and procedures we evaluated.



Figure 9: Electromagnetic tracking systems and their components used in this study (left) Aurora and (right) 3D Guidance

3.3.5 Accomplishment 5: RFA for Liver Tumors

An image-guided system for optimized volumetric treatment planning and execution for radiofrequency ablation of liver tumors was developed [Banovac 2007]. Radiofrequency ablation of liver tumors is becoming an increasingly popular option for the treatment of cancer. However, the procedure has several technical challenges, mostly associated with precision targeting of the tumor and ensuring complete ablation coverage. In this paper we describe an image-guided system that we are developing for improved visualization and probe placement during these procedures. The system will include a pre-procedure optimization module and an intra-procedure guidance component. The system concept is explained and some preliminary results are given. While this system is designed for radiofrequency ablation of liver tumors, the methods are applicable to other organs and treatment methods.

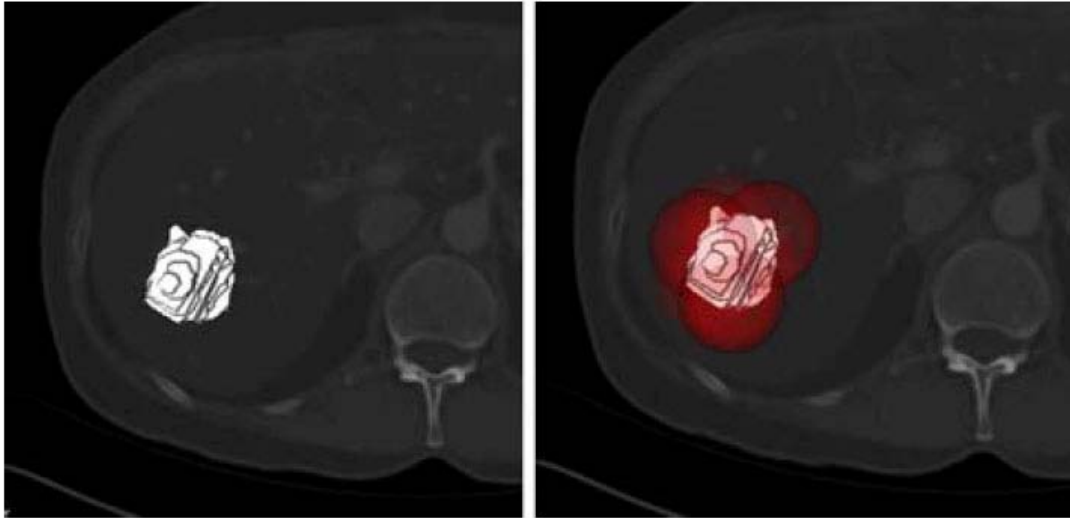


Figure 10: Example CT image from Georgetown University Hospital showing segmented liver tumor (white on left hand image) and overlapping sphere placement to cover tumor (red spheres on right hand image)

3.3.6 Accomplishment 6: PET/CT Guided Interventional Procedures

Positron-emission tomography (PET) and PET/CT (computed tomography) are becoming increasingly important for diagnosis and treatment of cancer. Clinically relevant changes can sometimes be seen on PET that are not seen on other imaging modalities. However, PET is not suitable for guiding biopsy as the images are not obtained in real-time. Therefore, our research group has begun developing a concept for PET/CT-guided interventional procedures. This paper presented the rationale for this concept, outlined our research plan, and included an initial study to evaluate the relative sensitivity of CT and PET/CT in detecting suspicious lesions [Wong 2007].

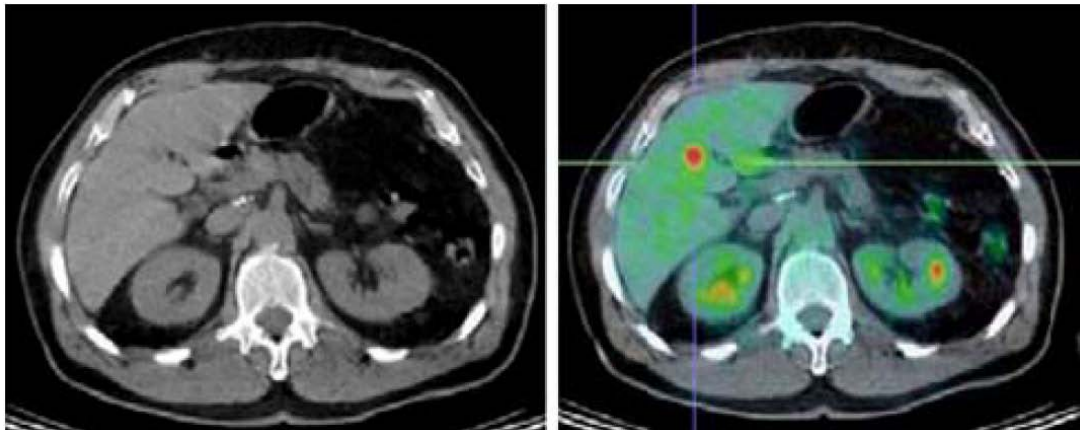


Figure 11: CT image (left) and PET/CT fused image (right). With CT alone, the tumor in the liver is inconspicuous, but with PET/CT the tumor is easily seen as the bright red spot indicated by the crosshairs (there is also a second lesion in the kidney at lower right on the PET/CT image). These images clearly illustrate the challenge of attempting image-guided biopsy using only CT or X-ray fluoroscopy for navigation).

3.4 Task 4: Image-Guided Bronchoscopy

The major accomplishment during this reporting period was the development of an electromagnetically tracked biopsy forceps [Choi 2007]. Transbronchial biopsy is a common method for tissue acquisition in diagnosis of various pulmonary diseases. However, the procedure has technical limitations when performed on peripheral nodules due to the small size of peripheral airways. To enhance the accuracy of the procedure, we developed an electromagnetically tracked biopsy forceps and evaluated the device with our image-guided system. Our initial experimental results served as a proof of concept of our system. Future work will include additional phantom studies and animal experiments.

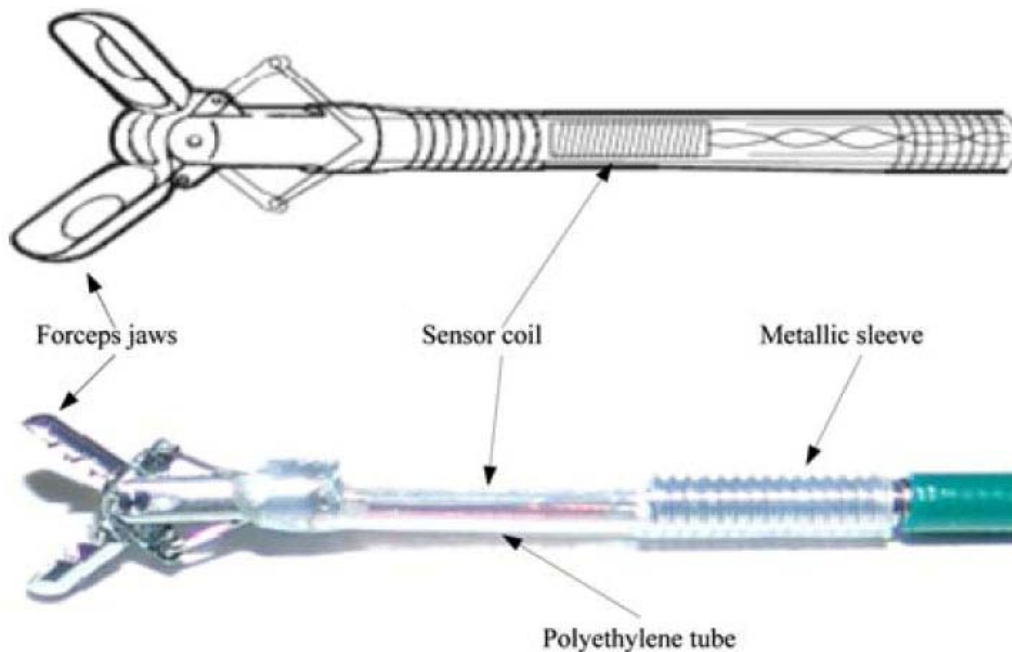


Figure 12: Wireframe model and a photograph of the EM tracked biopsy forceps

During the last reporting period, dedicated funding for this task was obtained under grant X81XWH-07-2-0104, so this task will no longer be reported under this contract.

4 Key Research Outcomes

This section provides a bulleted list of key research accomplishments during the entire project:

- Developed a prototype robotic system with force feedback to assist the physician in minimally invasive ultrasound interventions
- Completed a new rotating needle driver to hold and spin the needle for biopsy procedures under robotic control
- Developed a control methodology for the rehabilitation arm exoskeleton for modulating shoulder impedance during physical therapy
- Added a haptic control interface to powered arm curl machine for improved capabilities for physical therapy
- Demonstrated image-guided spinal vertebroplasty in a phantom model using our open source software package IGSTK
- Completed an evaluation study of electromagnetic tracking in the clinical environment
- Developed an image-guided system for optimized volumetric treatment planning and execution for radiofrequency ablation of liver tumors

- Investigated PET/CT guided interventional papers including completing an initial study to evaluate the relative sensitivity of CT versus PET/CT in detecting suspicious lesions

5 Reportable Outcomes

This section provides a list of reportable outcomes. The major product of this year is the list of papers given in Section 7 (References). Copies of these documents are provided in the appendix.

In addition, several proposals to the National Institutes of Health were submitted based on this work. Several small business grants were received with company partners, including one on precision mouse biopsy based on MR imaging.

Our research group also continued to be prominent at major conferences in the field, including the SPIE Medical Imaging meeting, the Medical Image Computing and Computer Aided Interventions (MICCAI) meeting, and the Computer Aided Radiology and Surgery (CARS) meeting.

6 Conclusions

The Periscopic Spine Surgery project has continued to lay the ground work for developing the physician assist systems of the future. These systems will incorporate robotics, tracking, and visualization to improve the precision of instrument placement and manipulation in minimally invasive procedures. We have begun to show the feasibility of electromagnetic position sensing and image overlay in the clinical environment and plan to apply for FDA approval soon. We have installed a new angiography suite at the hospital incorporating a flat panel detector and many of our future activities will be focused here. We have continued our work on respiratory motion compensation as a theme which cuts across many of our efforts. This project has enabled the Georgetown team to become a world leader in the emerging fields of computer aided surgery and medical robotics. Our goal continues to be to develop systems to add the physician in these demanding minimally invasive procedures with the ultimate aim of improving patient care.

7 References

- [Banovac 2007] Filip Banovac, Hernan Abeledo, Enrique Campos-Nanez, Bradford J. Wood, Teo Popa, Patrick Cheng, Kevin Cleary, “An image-guided system for optimized volumetric treatment planning and execution for radiofrequency ablation of liver tumors,” *Int J CARS* (2007) 2 (Suppl 1):S146–S151, DOI 10.1007/s11548-007-0089-1.
- [Carignan 2008a] Craig R. Carignan, Michael P. Naylor, and Stephen N. Roderick, “Controlling Shoulder Impedance in a Rehabilitation Arm Exoskeleton,” 2008 IEEE International Conference on Robotics and Automation, Pasadena, CA, USA, May 19-23, 2008: 2453-2458.
- [Carignan 2008b] Craig R. Carignan and Jonathan Tang, “A Haptic Control Interface for a Motorized Exercise Machine,” 2008 IEEE International Conference on Robotics and Automation, Pasadena, CA, USA, May 19-23, 2008: 2055-2060.
- [Choi 2007] Jae Choi, Lucian Gruionu, Teo Popa, Eric Anderson, Kevin Cleary, “Transbronchial biopsy based on electromagnetic tracked biopsy forceps,” *Int J CARS* (2007) 2 (Suppl 1): S143–S145.
- [Ding 2008a] Jienan Ding; Noureen Khan; Patrick Cheng; Emmanuel Wilson; Vance Watson; Kevin Cleary; Ziv Yaniv, “Accuracy analysis of an image-guided system for vertebroplasty spinal therapy based on electromagnetic tracking of instruments,” *Proceedings Vol. 6918, Medical Imaging 2008: Visualization, Image-Guided Procedures, and Modeling*, Michael I. Miga; Kevin R. Cleary, Editors, 69181K, DOI: 10.1117/12.772794.
- [Ding 2008b] Jienan Ding; Dan Swerdlow; Shuxin Wang; Emmanuel Wilson; Jonathan Tang; Kevin Cleary, “Robotically assisted ultrasound interventions,” *Proceedings Vol. 6918, Medical Imaging 2008: Visualization, Image-Guided Procedures, and Modeling*, Michael I. Miga; Kevin R. Cleary, Editors, 691827, DOI: 10.1117/12.772729.
- [Enquobahrie 2007] Andinet Enquobahrie, Patrick Cheng, Kevin Gary, Luis Ibanez, David Gobbi, Frank Lindseth, Ziv Yaniv, Stephen Aylward, Julien Jomier and Kevin Cleary, “The Image-Guided Surgery Toolkit IGSTK: An Open Source C++ Software Toolkit,” *Journal of Digital Imaging*, Springer, Vol. 20, Supplement 1, November 2007, 21-33, DOI 10.1007/s10278-007-9054-3.
- [Lin 2008] Ralph Lin; Peng Cheng; David Lindisch; Filip Banovac; Justin Lee; Kevin Cleary, “Phantom evaluation of an image-guided navigation system based on electromagnetic tracking and open source software,” *Proceedings Vol. 6918, Medical Imaging 2008: Visualization, Image-*

Guided Procedures, and Modeling, Michael I. Miga; Kevin R. Cleary, Editors, 691826, DOI: 10.1117/12.771254.

- [Shah 2008] S. Shah · A. Kapoor · J. Ding · P. Guion · D. Petrisor · J. Karanian · W. F. Pritchard · D. Stoianovici · B. J. Wood · K. Cleary, “Robotically assisted needle driver: evaluation of safety release, force profiles, and needle spin in a swine abdominal model” *International Journal of Computer Assisted Radiology and Surgery*, Springer, 2008, DOI 10.1007/s11548-008-0164-2.
- [Wilson 2008] Emmanuel Wilson; Ziv Yaniv; David Lindisch; Kevin Cleary, “A buyer's guide to electromagnetic tracking systems for clinical applications,” Proceedings Vol. 6918, Medical Imaging 2008: Visualization, Image-Guided Procedures, and Modeling, Michael I. Miga; Kevin R. Cleary, Editors, 69182B, DOI: 10.1117/12.770509.
- [Wong 2007] Kenneth Wong, Sara Petrillo, Filip Banovac, Joseph Rahill, Elliot Levy, Raj Shekhar, David Earl-Graef, Kevin Cleary, “PET/CT-guided interventional procedures: rationale, justification, initial study, and research plan,” *Int J CARS* (2007) 2 (Suppl 1):S150–S151, DOI 10.1007/s11548-007-0089-1.

Appendices (Papers)

Copies of the 11 papers selected for this report are reproduced in this section.

7.1 Banovac 2007: An image-guided system for ...

Reprint begins on the next page and is two pages.

An image-guided system for optimized volumetric treatment planning and execution for radiofrequency ablation of liver tumors

Filip Banovac^a, Hernan Abeledo^b, Enrique Campos-Nanez^b, Bradford J. Wood^c, Teo Popa^a, Patrick Cheng^a, Kevin Cleary^a

^aComputer Aided Interventions and Medical Robotics (CAIMR), Imaging Science & Information Systems (ISIS) Center, Georgetown University Medical Center, Washington, DC, USA

^bDepartment of Engineering Management and System Engineering, George Washington University, Washington, DC, USA

^cDiagnostic Radiology Department, NIH Clinical Center, Bethesda, MD, USA

Abstract Radiofrequency ablation of liver tumors is becoming an increasingly popular option for the treatment of cancer. However, the procedure has several technical challenges, mostly associated with precision targeting of the tumor and ensuring complete ablation coverage. In this paper we describe an image-guided system that we are developing for improved visualization and probe placement during these procedures. The system will include a pre-procedure optimization module and an intra-procedure guidance component. The system concept is explained and some preliminary results are given. While this system is designed for radiofrequency ablation of liver tumors, the methods are applicable to other organs and treatment methods.

Keywords Radiofrequency ablation · Liver tumors · Image guidance · Optimization · Planning

1. Introduction

Radiofrequency ablation (RFA) of liver tumors is a minimally invasive procedure that is becoming increasingly popular as a treatment option. Although RFA has become a widely used modality in the primary treatment of hepatocellular carcinoma (HCC) and liver metastases, the procedure has several technical challenges. One of the most significant challenges facing RFA is successfully targeting the tumor and providing adequate ablation coverage of the tumor. An improperly placed probe not only provides incomplete tumor ablation, but could also damage nearby delicate tissues or organs. Despite the availability of larger electrodes, many procedures require multiple ablations to maintain a 1 cm margin. Multiple ablations are difficult to execute as there is no way to visualize the overlapping areas or to distinguish ablated areas from non-ablated areas. Due to the lack of any real-time image guidance, repeated insertions and positioning of the electrode may be required to hit the target lesion. Unablated tissue containing residual tumor may result in tumor recurrence. Some studies have shown that complete necrosis of the tumor was achieved in only 29–47.6% of HCC lesions with diameters of 3.1 cm or greater [1, 2].

To meet these challenges, we are developing an image-guided system based on electromagnetic tracking for improved visualization and probe placement during RFA of liver tumors. The system will include segmentation of the tumor and the liver vasculature for improved visualization and path planning. The system will also include a pre-procedure module that will allow for volumetric computer-assisted 3D treatment planning. While this project is focused on liver tumors, the techniques developed will be applicable to many other diseases and organs.

Pre-treatment and post-treatment CT scans of a typical case are shown in Fig. 1. This 3 cm hepatocellular carcinoma is a recurrence of disease of a previously resected primary liver tumor. Repeat surgery was avoided by treating this tumor with percutaneous RFA. Note that there is a clean margin of dark and devascularized, dead tissue including the tumor itself and a surrounding 1 cm margin of normal tissue.

2. Methods

The integrated system will consist of two major components:

1. a pre-procedure planning component for liver and tumor segmentation and optimization of a treatment plan
2. an intra-procedure component for providing image guidance during the procedure

2.1. Pre-procedure planning and volumetric optimization

We intend to employ mathematical optimization methods to develop a general treatment planning methodology as described below. Our treatment planning approach will be guided by these five criteria:

1. Minimize the number of ablations. Fewer ablations mean shorter treatment times and less chance for complications.
2. Limit the number of probe insertions. Clinical considerations limit the number of perforations of the liver capsule by the RFA probe to at most 3 or 4 and preferably just 1 or 2. The optimization model will take into account the number of these perforations and favor reinsertions of the probe through the same entry point. The model will include the possibility of performing several ablations along the same linear trajectory, as is common in clinical practice.
3. Probe trajectory constraints. The model will account for physical constraints imposed by ribs, vessels, and other organs which may restrict possible trajectories.
4. Irregularly shaped tumors. The optimization model will be designed to use segmented image data from the patient and will not pre-suppose a particular tumor shape. This will make this treatment planning method much more general and increase the usefulness of the results.
5. Controlling unnecessary damage to healthy tissue. The burned volume from the overlapping probes will be estimated in the model with the goal of keeping it as small as possible while fully covering the tumor and margin. This will minimize damage to healthy tissue surrounding the tumor.

2.2. Integrated system and intra-procedure component

The integrated system will include the following components:

1. Segmentation module.
2. Treatment planning module.
3. Commercial electromagnetic tracking system (AURORA from Northern Digital Inc., Waterloo, Canada).
4. User interface so that the physician can view the segmentation results (and edit them if needed); specify the possible insertion points for the trajectory planning and observe/modify the trajectory planning results; and carry out the intervention.

Here we describe how we envision using the system in clinical practice. A flowchart of these steps is shown in Fig. 2.

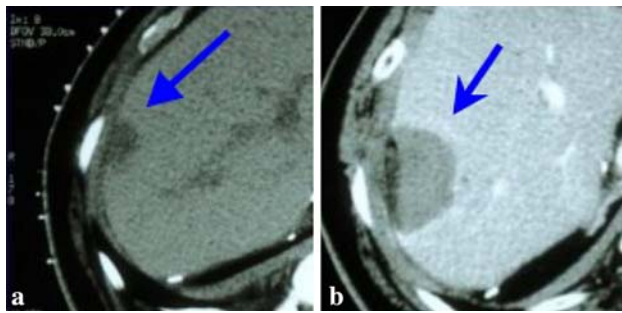


Fig. 1 **a** Before treatment note the low attenuation liver mass in the posterior segment of the right hepatic lobe abutting the liver capsule. **b** After treatment note a clean margin of dark, devascularized, ablated tissue including the original tumor and the surrounding tissue

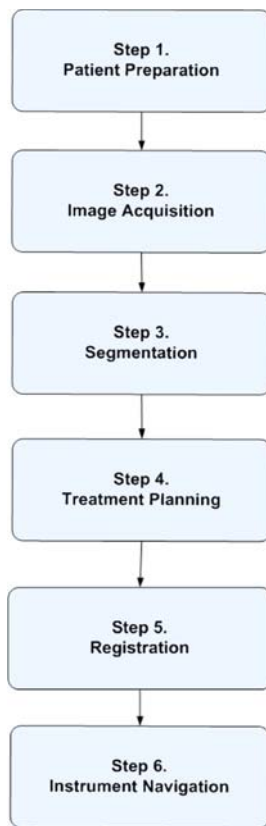


Fig. 2 Workflow for integrated system

The patient will be prepared by placing three or more fiducials above the liver. Contrast enhanced CT images will be obtained from the lung base through the abdomen and reconstructed to 1.0 mm. The relevant anatomy will be segmented, including the tumor and a 1 cm margin. Treatment planning to determine overlapping probe placement will be completed based on the constraints described in Sect. 2.1. The AURORA electromagnetic tracking system will be positioned near the patient and enabled. Image registration will be performed using paired point matching [3]. The system will then provide the physician with targeting assistance and image overlay so that the treatment plan can be carried out.

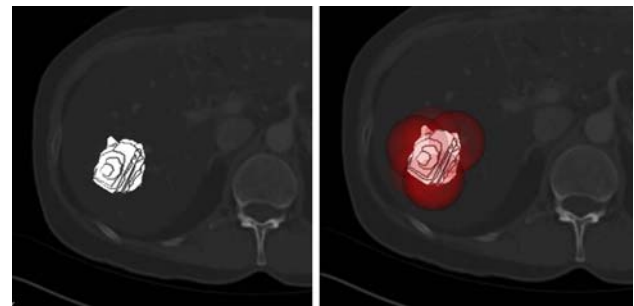


Fig. 3 Example CT image from Georgetown University Hospital showing segmented liver tumor (white on left hand image) and overlapping sphere placement to cover tumor (red spheres on right hand image)

3. Results

To date, we have some preliminary results for the volumetric treatment planning component. Testing was done on several synthetic data sets with known optimal solutions and on two CT data sets from actual liver hepatomas (with tri-axial diameters in cm of $3.1 \times 2.3 \times 5.4$ and $3.4 \times 3.5 \times 3.3$, respectively). Results using synthetic data show that solution quality is very good. Computational times range from seconds to less than 6 minutes in all cases. Assuming a 5 cm elliptical array based on the LaVeen RFA system, both hepatoma cases were executed with 1 cm surgical margin. The first case was covered with six ablations while the second tumor was covered with four ablations. An example result is shown in Fig. 3. For this example, a rough segmentation was done manually to outline the tumor, followed by treatment planning as shown.

Acknowledgments

This work was funded by US Army grant W81XWH-04-1-0078 and administered by the Telemedicine and Advanced Technology Research Center (TATRC), Fort Detrick, Maryland, USA. The content of this manuscript does not necessarily reflect the position or policy of the US Government. This study was also supported in part by the Intramural Research Program of the NIH.

References

1. Livraghi T, Goldberg SN et al (2000) Hepatocellular carcinoma: radio-frequency ablation of medium and large lesions. *Radiology* 214(3):761–768
2. Llovet J, Vilana R et al (2001) Increased risk of tumor seeding after percutaneous radiofrequency ablation for single hepatocellular carcinoma. *Hepatology* 33:1124–1129
3. Arun KS, Huang TS et al (1987) Least-squares fitting of two 3-D point sets. *IEEE Trans Pattern Anal Mach Intell* 9(5):698–700

Electromagnetic needle tracking and multi-modality imaging for biopsy and ablation guidance

J. Krücker^a, S. Xu^a, N. Glossop^b, Z. Neeman^c, J. Locklin^c, B.J. Wood^c

^aPhilips Research North America, Briarcliff Manor, NY, USA

^bTraxtal Inc., Toronto, ON, Canada

^cNIH Clinical Center, Bethesda, MD, USA

Abstract Purpose: To evaluate accuracy and demonstrate utility of electromagnetic (EM) tracking for guidance during soft-tissue ablation and biopsy procedures. **Methods** A prototype interventional navigation system using EM tracking for localization of needles and ultrasound probes was used to assist ultrasound and CT guidance of radiofrequency ablations and biopsies in 16

7.2 Carignan 2008a: Controlling shoulder ...

Reprint begins on the next page and is six pages.

Controlling Shoulder Impedance in a Rehabilitation Arm Exoskeleton

Craig Carignan and Michael Naylor

Abstract—A methodology is developed to enable compliance control of the shoulder joint in an arm exoskeleton developed for physical therapy. Setting the remote center of compliance at the shoulder will allow clinicians to enact resistance training protocols to strengthen the rotator cuff and other joint musculature supporting the shoulder complex. The rotational kinematics for the shoulder are first derived, and then the torques applied at the shoulder are estimated using force sensors placed at the hand and elbow interfaces. Impedance and admittance control schemes are both developed to realize isolateral strengthening exercises, and some preliminary experimental results are presented for implementation on an arm exoskeleton currently under development.

I. INTRODUCTION

In most manipulator applications, the remote center of compliance is located at the tool tip using force readings from a sensor located in the wrist. Likewise, exoskeletons developed for virtual reality (VR) applications usually reflect forces at the hand resulting from interaction with virtual environments [1]. This type of force reflection can be met by using a central controller to simultaneously move all of the exoskeleton joints to exert a desired force at the hand. However, this strategy is ineffective for rehabilitation applications where individual arm joints are being targeted for physical therapy.

In a rehabilitation arm exoskeleton, the remote center of compliance is any joint-muscle group in the arm being targeted for therapy. For example, during the shoulder abduction exercise shown in Fig. 1, the resistance about the shoulder abduction axis needs to be controlled by the exoskeleton over the range of motion. An additional complication is that a force-torque sensor placed at the wrist or hand does not alone provide enough information to determine the torques in the shoulder joint. Therefore alternative force sensor emplacement strategies also need to be investigated.

In this article, dual impedance-admittance control approaches are investigated for modulating impedance in the shoulder joint during exercise therapy. The shoulder-axis can either be fixed or vary with configuration of the arm. Impedance control schemes are explored that use force-torque sensors placed at the hand and elbow to estimate the



Fig. 1. The MGA Exoskeleton has five powered joints including a three-axis intersecting shoulder and a scapula elevation joint.

applied forces. Some preliminary test results are presented for implementing impedance control for realizing isolateral exercise protocols.

II. PREVIOUS WORK

Most arm exoskeletons built to-date were developed as either force-reflecting master arms for teleoperation or as haptic devices for virtual reality applications [1]. In VR applications, “contact” forces are imparted at the handle of the exoskeleton that replicate forces sensed by a slave arm or by interaction with a virtual environment. A basic form of impedance control is usually implemented in which the Cartesian forces at the handle are mapped into joint torque commands using the Jacobian [10]. This approach eliminates the need to compute the inverse kinematics and is stable at low impedances.

The main drawback of impedance control is that good force replication at the handle requires compensation of the natural dynamics of the exoskeleton, such as gravity loading and drive friction. A force loop wrapped around the force sensor can reduce unmodeled effects [2], but it can also easily destabilize the system. The *Exoskeleton Arm-Master* [1] and the *L-Exos Exoskeleton* [7] are classic examples of exoskeletons that use this approach.

An alternative approach called “admittance” control has primarily been used to control manipulators used as large-reach haptic devices [3], [5]. In this approach, the sensed force at the handle is used as the input to a desired impedance

This work was supported by the U.S. Army Telemedicine and Advanced Technology Research Center (TATRC), Ford Detrick, Maryland

C. Carignan is a research associate professor with the Imaging Science and Information Systems Center, Georgetown University, Washington DC 20057 USA crc32@georgetown.edu

M. Naylor was a faculty research associate with the Space Systems Laboratory, University of Maryland, College Park MD 20740 USA and is now a robotics engineer with Accuray, Inc., Sunnyvale, CA 94089 naylor@ssl.umd.edu

model, which outputs a desired motion to be imparted at the hand. The Cartesian position is mapped into joint position commands using the inverse kinematics, which are then input to a proportional-derivative (PD) servocontroller to drive the joints to the desired position.

The main advantage of the admittance approach is that the high gains of the joint position servo-loop are used to reject unmodeled dynamics without resorting to model feed-forward. However, it has the major drawback of instability for high admittance (low impedance), which is the opposite of impedance control [9]. The *Sensor Arm* [11] is an example of an exoskeleton implementing this approach, and the more recent *ARMin Exoskeleton* [12] appears to be able to operate in either admittance and impedance modes.

Almost all exoskeleton designs incorporate a six-axis force sensor at the gripper for determining forces applied at the hand [7]. Some designs use force-torque sensors mounted on the links to obtain forces at other locations along the arm. The *ARMin* reacts loads to the distal end of the forearm link through force-torque sensor attached to a wrist cuff [12]. The *Sensor Arm* [11] uses concentric rings connected by strain gauges to determine forces applied by the arm, where the inner ring is secured to the limb using an inflatable bladder. Attempting to use torque cells at the exoskeleton joints to derive torques in the human joints is fraught with difficulties because the exoskeleton joints do not align with the human joints. Thus this approach is rarely used.

III. SHOULDER KINEMATICS

The human shoulder (glenohumeral) joint is a ball-and-socket joint capable of abduction/adduction, flexion/extension, and medial/lateral rotation. For a serial manipulator to replicate this motion, three serially connected rotational joints with mutually intersecting axes are needed. In addition, the glenohumeral joint translates along the surface of a sphere as the humerus (upper arm) elevates, so the ability to replicated scapulo-humeral rhythm is key to realizing natural movement of the shoulder.

Figure 2 shows the kinematic configuration of the MGA Exoskeleton along with Denavit-Hartenburg (D-H) link frame assignments [6]. The D-H parameters for the kinematics are given in Table I except for the scapula joint 0 which is mounted perpendicular to the torso. The angle between the z_0 and z_1 axis is 30° , and the angle between the z_3 and z_4 axis is 45° . The scapula, upper arm, and forearm links all have passive sliding joints to accommodate variable subject geometry: $L_S = 14.0 - 25.6$ cm, $L_U = 27.3 - 31.3$ cm, and $L_F = 30.0 - 39.0$ cm. The displacement of the force sensors along the z -axis of their respective frames are $L_{SH} = 5.72$ cm and $L_{SE} = 7.62$ cm.

A. Arbitrary Shoulder Rotation

The shoulder rotation is defined as the orientation of the upper arm relative to the body frame $\{B\}$:

$${}^B R_U = {}^B R_0 {}^0 R_3 {}^3 R_U \quad (1)$$

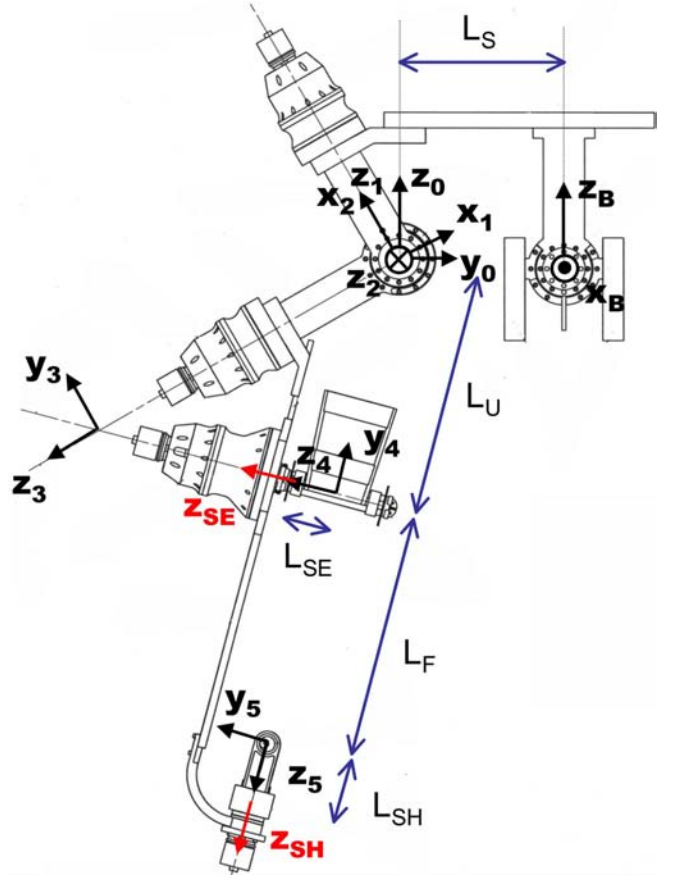


Fig. 2. CAD drawing of MGA Exoskeleton shoulder showing link frame assignments.

TABLE I
D-H PARAMETERS FOR THE MGA EXOSKELETON.

link i	a_{i-1} (cm)	α_{i-1} (deg)	d_i (cm)	θ_i^* home (deg)
1	0	+30	0	+90
2	0	-90	0	-105
3	0	+90	$\sqrt{2}L_U$	-90
4	0	-45	$-L_U$	0
5	0	-90	L_F	0

where ${}^B R_0 = R_X(-\theta_0)$ and frame $\{U\}$ is co-located with frame $\{3\}$ but rotated 45° about the x_3 axis, ${}^3 R_U = R_X(45^\circ)$. $R_X(\theta)$ is defined as the pure x-axis rotation

$$R_X(\theta) \equiv \begin{bmatrix} 1 & 0 & 0 \\ 0 & \cos(\theta) & -\sin(\theta) \\ 0 & \sin(\theta) & \cos(\theta) \end{bmatrix} \quad (2)$$

${}^0 R_3$ can be found by using the D-H Table to find the local link transformations ${}^i R_{i+1}$ and cascading the resulting rotation matrices for links 1-3. The direction of the humeral axis in the body frame $\{B\}$ is given by ${}^B \hat{z}_U$, the third column of ${}^B R_U$, which is used to compute the axis of rotation for internal/external rotation exercises.

The rotational velocity of the upper arm relative to the body frame $\{B\}$ is found from

$${}^B\omega_U = {}^B J_U \dot{\theta}_s \quad (3)$$

where $\theta_s \equiv [\theta_0 \ \theta_1 \ \theta_2 \ \theta_3]^T$ represents the vector of shoulder joint angles 0-3 and ${}^B J_U$ is 3×4 rotational Jacobian found from the forward kinematics.

B. Self-Motion Shoulder Rotation

In some instances, the desired axis of shoulder rotation might be along a straight line from the shoulder to the wrist as shown in Figure 3. Because the axis passes through the wrist, rotation about this axis or “elbow orbit” produces no motion of the wrist and is thus referred to as “self-motion”. The elbow “orbit” angle ϕ is defined as the angle that the plane formed by the points S, E, and W makes with the reference plane defined by the reference vector, \hat{v} , and the shoulder-wrist vector, p_w [8].

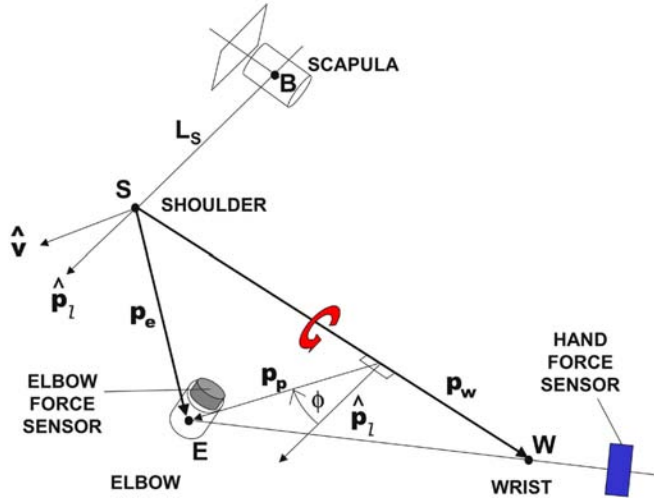


Fig. 3. Self-motion of the arm or “elbow orbit” occurs about a line from the shoulder to the wrist.

Let the vectors from the shoulder to the wrist and elbow be defined as p_w and p_e , respectively, and let \hat{v} denote an arbitrary fixed unit reference vector in frame 0. Now let the following auxiliary vectors be defined as

$$p_d \equiv \hat{p}_w(\hat{p}_w^T p_e) \quad (4)$$

$$p_p \equiv p_e - p_d \quad (5)$$

$$p_\ell \equiv (p_w \times \hat{v}) \times p_w \quad (6)$$

The roll angle of the SEW plane or “elbow orbit angle” is defined as the angle between p_p and p_ℓ

$$\tan \phi \equiv \frac{\hat{p}_w^T (p_\ell \times p_p)}{p_\ell^T p_p} \quad (7)$$

Using the forward kinematics to compute p_w and p_e , ϕ is determined by performing the vector operation in (7) numerically and then taking the arctangent of the result.

IV. SHOULDER TORQUES

For both monitoring and control purposes, it will be important to determine the torques being exerted by the exoskeleton about the shoulder joint. Since there is no direct way to measure these torques, force sensors located at the hand and elbow contact points can be used to estimate the torques. For general shoulder rotations, the shoulder torques can be decomposed into those perpendicular to the humeral axis and those about the humeral axis. The perpendicular torques are determined using the elbow sensor, and torques about the humerus axis are estimated using the hand sensor.

A. Azimuth/Elevation Torques

The shoulder azimuth and elevation torques are estimated by projecting the force and moment from the elbow sensor to frame $\{0\}$. The elbow sensor is fixed to the upper arm frame $\{U\}$ at a distance L_{SE} along the elbow pitch axis z_4 and oriented at an angle γ_{SE} about z_4 so that ${}^U p_{SE} = [0 \ 0 \ L_{SE}]^T$ and ${}^U R_{SE} = R_Z(\gamma_{SE})$ where

$$R_Z(\theta) \equiv \begin{bmatrix} \cos(\gamma) & -\sin(\gamma) & 0 \\ \sin(\gamma) & \cos(\gamma) & 0 \\ 0 & 0 & 1 \end{bmatrix} \quad (8)$$

is a pure rotation about the z-axis. The force f and moment n in frame $\{U\}$ are calculated from the elbow sensor force and moment readings f_{SE} and n_{SE} as follows [6]

$${}^U f_U = {}^U R_{SE} f_{SE} \quad (9)$$

$${}^U n_U = {}^U p_{SE} \times {}^U f_U + {}^U R_{SE} n_{SE} \quad (10)$$

The moment in frame $\{0\}$ is then found from (9) and (10) using

$${}^0 n_0 = {}^0 p_U \times {}^0 R_U {}^U f_U + {}^0 R_U {}^U n_U \quad (11)$$

which can then be converted to frame $\{B\}$ coordinates by pre-multiplying (11) by ${}^B R_0$.

B. Humeral Torque

The torque about the upper arm is found by taking the component of the hand force that is tangent to the humeral axis, i.e. the z_4 direction. The hand sensor is fixed to frame $\{5\}$ at a distance L_{SH} along the z_5 -axis and oriented at an angle γ_{SH} about z_5 so that ${}^5 p_{SH} = [0 \ 0 \ L_{SH}]^T$ and ${}^5 R_{SH} = R_Z(\gamma_{SH})$. The hand sensor force in frame $\{4\}$ coordinates is found from

$${}^4 f_5 = {}^4 R_5 {}^5 R_{SH} f_{SH} \quad (12)$$

The humeral torque can be determined from the z-component of the hand frame force and the lever arm provided by the perpendicular component of the forearm relative to the upper arm

$$\tau_{UA} = (L_F + L_{SH}) \sin(\theta_4) {}^4 f_5 \bullet \hat{z} \quad (13)$$

where θ_4 is the elbow flexion angle which is fully extended at 0° .

C. Elbow Orbit Torque

The z-component of the elbow force sensor in f_{SE} can also be used to determine the torque, τ_ϕ , exerted about the shoulder-wrist axis, p_w . The elbow orbit torque is calculated by taking the product of the z-component of the force and multiplying it by the moment arm

$$\tau_\phi \equiv |p_p| f_{SE} \bullet \hat{z} \quad (14)$$

where p_p is the minimum distance from the elbow to \overline{SW} found using (5).

V. ISO-LATERAL EXERCISE PROTOCOLS

Iso-lateral exercises are those that occur around a single rotation axis of the shoulder and closely resemble those performed manually with dumbbells, rubber tubing, and exercise machines [13]. Examples of shoulder rotation exercises include internal/external rotation and shoulder abduction/adduction as shown in Figures 4 and 5, respectively. In isotonic exercises, the motion of the shoulder joints is determined by the resistance about the desired shoulder axis of rotation. In self-motion exercises, the axis of rotation is automatically specified by the position of the wrist.



Fig. 4. Exoskeleton shown performing external/internal rotation at about 90° elbow flexion.

Some common iso-lateral exercises are shown in Table II. The second column indicates the plane of motion, and the third column indicates the axis of rotation. The final column specifies the azimuth and elevation of the humerus during the exercise. Azimuth corresponds to the rotation about the longitudinal axis z_B (0° is straight ahead) and elevation is the angle the humerus makes with the longitudinal axis (0° is straight down).

Exercises are implemented using the modular control architecture shown in Figure 6 [4]. The exercise protocol is first parsed into a control mode based on the desired activation of arm joint variables. This code then determines which controller should be activated for the possible combinations of arm groups: scapula, shoulder, elbow pitch,



Fig. 5. Exoskeleton shown at 90° shoulder abduction.

TABLE II
SHOULDER ISO-LATERAL EXERCISES.

Exercise	Plane of Motion	Rotation Axis	Azim./Elev.
Ab/Adduction	frontal	$[1, 0, 0]$	90°/0°-90°
Flex/Extension	sagittal	$[0, 1, 0]$	0°/0°-90°
Ab/Adduction	transverse	$[0, 0, 1]$	0°-90°/90°
Elevation	scapula	$[\sqrt{3}/2, 1/2, 0]$	60°/0°-90°
Int/Ext Rotation	\perp humerus	$\overline{SE}, {}^B z_U$	-/-
Elbow Orbit	\perp shoulder-wrist	$\overline{SW}, {}^0 p_5$	-/-

and elbow orbit. These groups can implement impedance and admittance modes depending upon the desired level of impedance and torque sensing accuracy. In particular, the shoulder impedance controller and elbow orbit admittance controller are discussed in more detail below.

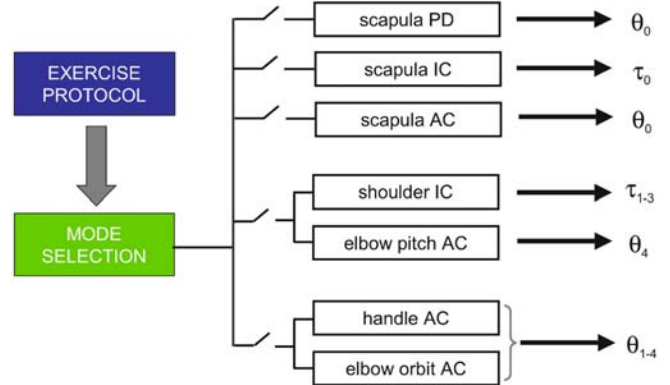


Fig. 6. Control modules are activated by the mode selector depending upon the exercise protocol (AC = admittance control, IC = impedance control, PD = proportional-derivative control).

A. Shoulder Impedance Module

The shoulder impedance controller is generally used for low resistance shoulder rotation exercises, particularly shoulder abduction and extension. The desired impedance is multiplied by the angular velocity of the glenohumeral (GH) joint shown in Figure 7 to produce a desired Cartesian torque T_{des} . The desired torque and “sensed” torque are then differenced to form a torque error and multiplied by a feedback gain K_F .

The desired torque and feedback error are then converted back to joint coordinates to produce a desired torque τ_{des} . The desired torque and feedforward compensation τ_{fwd} are then summed to form the control command to the motors.

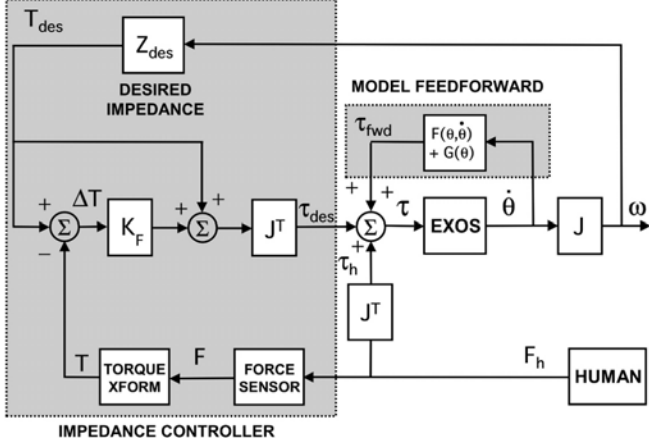


Fig. 7. Impedance controller used for shoulder axis rotation.

The desired stiffness and damping about the axis of rotation are set to the desired values in Z_{GH_d} while the impedances about the other two axes are set to very high values. Because the desired axis of rotation does not have to be aligned with a base frame axis, the z-axis of a rotation frame $\{C\}$ is aligned with the desired axis of rotation, and then ${}^B R_C$ is the transformation between the rotation frame and the body frame. Thus, the desired stiffness in Z_{GH_d} can be found from

$$K_{GH_d} = {}^B R_C K_C {}^B R_C^T \quad (15)$$

where K_C is the stiffness in the rotation frame. An analogous procedure is used to find the damping impedance B_{GH_d} where K_C is replaced by B_C in (15). If the rotation is about the humeral axis, then the z-axis of the compliance frame aligns with the humerus longitudinal axis so that ${}^B R_C = {}^B R_U$.

B. Elbow Orbit Admittance Module

The admittance controller shown in Figure 8 is used to drive the self-motion of the arm about the p_w axis while being used in conjunction with hand position commands. The elbow roll torque is derived from the elbow force sensor as derived in (14), which is then multiplied by the desired elbow orbit impedance to produce a desired elbow orbit velocity $\dot{\phi}_d$. The desired elbow orbit velocity is then converted to the nullspace component of the desired joint velocity using the inverse Jacobian, $J_{w\phi}^{-1}$. The nullspace velocity is then added to the particular solution of the desired joint velocity derived from the Cartesian hand velocity to form the total desired joint velocity $\dot{\theta}_d$. The desired velocity is then integrated and fed into a joint PD controller to drive the exoskeleton.

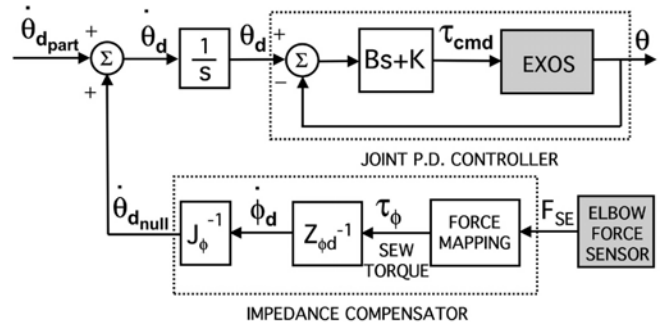


Fig. 8. The admittance controller utilizes force inputs from the elbow force sensor to compute the commanded elbow orbit rate based on the desired admittance.

VI. SHOULDER EXPERIMENTS

Several experiments were conducted to validate the operation of the shoulder impedance and admittance modules during simulated exercises. Since a feedforward model for the exoskeleton is still under development, a series of back-drive tests were conducted for the impedance module. The admittance module for elbow orbit was tested using a pair of load cells mounted on either side of the upper arm brace along the elbow axis. The scapula joint was maintained at 0° throughout these tests.

A. Impedance Control Experiments

The shoulder impedance controller was used to produce an internal/external rotation exercise by using Z_{GH_d} to select the axis of rotation along the humerus. The desired stiffness and damping about the humeral axis were set to zero while the off-axis values were set to 500 N-m/rad and 50 N-m/rad/sec, respectively. No feedforward model is currently available, so the natural dynamics of the exoskeleton were left uncompensated. During the test, the humerus was straight down by the side at 0° elevation parallel to z_B and the elbow was flexed at approximately 90° as shown in Figure 4.

The shoulder was first externally rotated, then internally rotated across the chest, and returned to the start position. The resulting angular velocity in base frame and humerus torque are shown in Figure 9. The rotation was primarily restricted to the z-axis as expected since it was parallel to the humeral axis. Since no torque was being commanded about the z-axis (due to the zero desired impedance) and the humeral axis was parallel to the gravity vector, the sensed torque was almost entirely due to the natural friction and inertial loading in the motor/drive mechanism. As seen in Figure 10, the rotation primarily occurs in the first shoulder joint which is oriented at a 30° angle with respect to the z_B -axis.

B. Self-Motion Experiments

In the next experiment, the subject executes a pure elbow orbit maneuver by “rolling” the elbow about the shoulder-wrist line in each direction at a constant velocity. The desired impedance was set to be a pure rotational damping of $Z_{\phi_{des}} = 50$ N-m/rad/sec about the shoulder-wrist axis

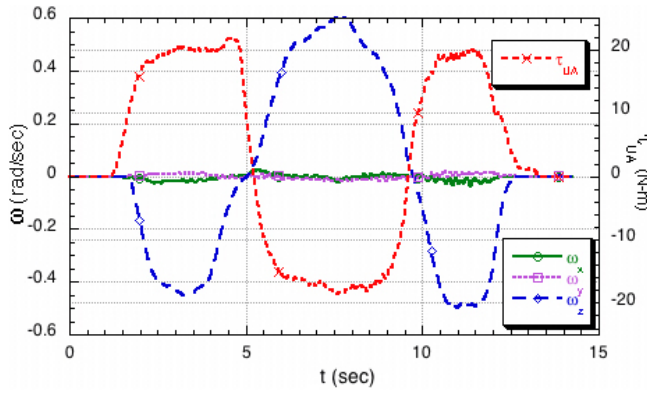


Fig. 9. Angular velocity and humerus torque during lateral/medial rotation.

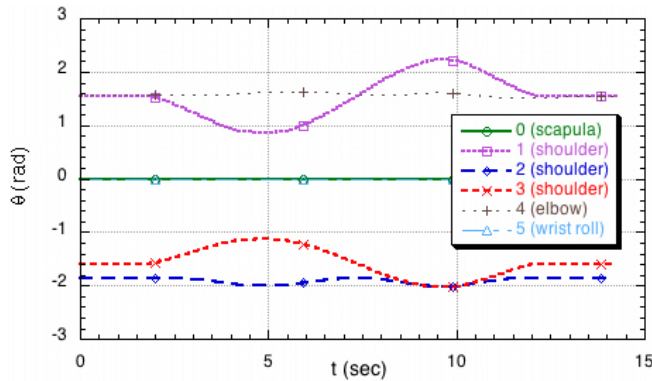


Fig. 10. Scapula and shoulder joint angles during shoulder ab/adduction.

so that the rotational velocity should be proportional to the exerted torque. The resulting elbow orbit angle and torque are shown in Figure 11. The torque alternates sign as the subject rotates the elbow first in one direction and then the other. The slope of the elbow orbit angle remains constant while the torque maintains the same value during the sequential rotations indicating a pure damping impedance.

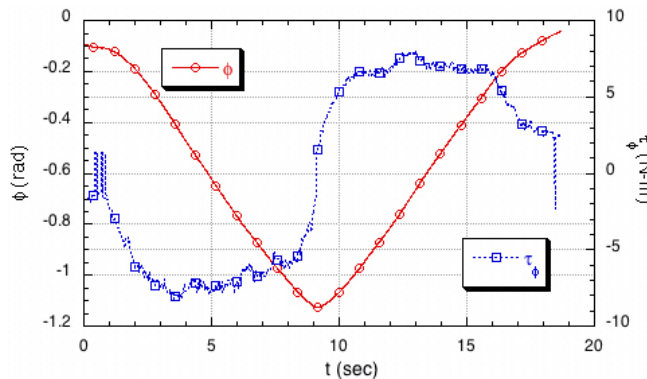


Fig. 11. Elbow orbit angle and torque for $b_\phi = 50$ N-m/rad/s during accommodation maneuver.

VII. CONCLUSION

Rotational kinematics were developed for controlling the shoulder joints of an arm exoskeleton for several isolateral

exercise protocols. A torque estimation scheme based on dual force sensors was also developed for calculating the torques applied on the glenohumeral joint by the exoskeleton. The impedance control tests revealed backdrive friction levels of approximately 40 N-m/rad/sec that will need to be compensated in the final design. The admittance controller demonstrated good ability to track a pure damping impedance for elbow orbit, which does not rely on model feedforward.

The elbow load cells are currently being replaced by a six-axis force-torque sensor to enable full determination of forces applied at the elbow for shoulder torque estimation. The full impedance parameters are being determined for a variety of exercise protocols that take into account the human strength potentials over the range of motion. Clinical trials will be conducted and compared with results from manual therapy after the control design is complete.

ACKNOWLEDGMENT

Thanks go to Mike Liszka, John Tang, Stephen Roderick, Emmanuel Wilson, and Mike Perna who made the MGA Exoskeleton possible. This project was sponsored by the U.S. Army Telemedicine and Advanced Technology Research Center (TATRC) under Grant #W81XWH-04-1-0078.

REFERENCES

- [1] G. C. Burdea, *Force And Touch Feedback For Virtual Reality*. New York: John Wiley and Sons, 1996.
- [2] C. Carignan and K. Cleary, "Closed-loop force control for haptic simulation of virtual environments," *The Electronic Journal of Haptics Research* (<http://www.haptics-e.org>), vol. 2, no. 2, pp. 1–14, Feb. 2000.
- [3] C. Carignan and D. Akin, "Achieving impedance objectives in robot teleoperation," in *Proc. of the IEEE Conference on Robotics and Automation*, 1997, pp. 3487–3492.
- [4] C. Carignan, J. Tang, S. Roderick, and M. Naylor, "A configuration-space approach to controlling a rehabilitation arm exoskeleton," in *Int. Conf. on Rehabilitation Robotics (ICORR)*, Noordwijk, Netherlands, June 2007, pp. 179–187.
- [5] C. Clover, G. Luecke, J. Troy, and W. McNeely, "Dynamic simulation of virtual mechanisms with haptic feedback using industrial robotics equipment," in *Proc. of the IEEE Conference on Robotics and Automation*, Apr. 1997, pp. 724–730.
- [6] J. Craig, *Introduction to Robotics: Mechanics and Control*, 2nd ed. Reading, Mass.: Addison-Wesley, 1989.
- [7] A. Frisoli, F. Rocchi, S. Marcheschi, A. Dettori, F. Salsedo, and M. Bergamasco, "A new force-feedback arm exoskeleton for haptic interaction in virtual environments," in *Proc. of the First Joint Eurohaptics Conference and Symposium on Haptic Interfaces for Virtual Environment and Teleoperator Systems*, 2005, pp. 195–201.
- [8] K. Kreutz-Delgado, M. Long, and H. Seraji, "Kinematic analysis of 7 DOF manipulators," *Int. Journal of Robotics Research*, vol. 11, no. 5, pp. 469–481, 1992.
- [9] D. Lawrence, "Impedance control stability properties in common implementations," in *Proc. IEEE Int. Conf. on Robotics and Automation*, 1988, pp. 1185–1190.
- [10] T. Massie and J. K. Salisbury, "The PHANTOM haptic interface: A device for probing virtual objects," in *Proc. ASME Winter Annual Meeting: Symposium on Haptic Interfaces for Virtual Environment and Teleoperator Systems*, vol. DSC 55-1, Nov. 1994, pp. 295–300.
- [11] A. Nakai, Y. Kunii, H. Hashimoto, and F. Harashima, "Arm type haptic human interface: Sensor arm," in *Intl. Conf. on Artificial Reality and Tele-Existence (ICAT)*, Tokyo, Japan, Dec. 1997, pp. 77–84.
- [12] T. Nef, M. Mihelj, G. Colombo, and R. Riener, "ARMin – robot for rehabilitation of the upper extremities," in *Proc. IEEE Int. Conf. on Robotics and Automation*, orlando, 2006, pp. 3152–3157.
- [13] L. Peterson and P. Renström, *Sports Injuries Their Prevention and Treatment*, 3rd ed. Champaign, IL: Human Kinetics, 2001.

7.3 Carignan 2008b: A haptic control interface ...

Reprint begins on the next page and is six pages.

A Haptic Control Interface for a Motorized Exercise Machine

Craig R. Carignan and Jonathan Tang

Abstract—A haptic interface is generated for a powered arm curl machine for modulating resistance “on-the-fly” during strength training and rehabilitation. Force signals from a load cell are input to an impedance loop based on the desired resistance law, which then outputs position commands to a servomotor. The kinematics between the actuator drive and arm curl angle are derived, and the admittance control implementation used for realizing the resistance laws is described. Preliminary experimental results are presented for viscous and inertial control laws.

I. INTRODUCTION

Resistance training has long been recognized as key to increasing muscular strength and endurance for both athletic performance and neuromuscular rehabilitation. The greatest increase in strength is attained through high resistances for short durations, while low resistances for long durations tend to produce high muscular endurance [1]. Until the 1970s, free weights (e.g. barbells and dumbbells) and Universal Gyms utilizing weight stacks driven by cable-pulleys were the primary means of resistance training. During the fitness craze in the 1980s, Nautilus, Cybex, and other companies introduced exercise machines into fitness centers for higher volume training. The cadre of resistance devices commercially available now includes pulley-weight machines, spring reaction devices (spring or pneumatic pistons), frictional devices (fans or brakes), and free weights.

Many of these machines offer some variability in resistance over the range of motion to account for the strength potential of the arm or leg in different configurations. This adjustability is usually attained through a series of cams and levers that make it harder to push (or pull) the “weight” in positions of greater biomechanical advantage. Although these devices may offer a level of adjustability, several researchers have experimentally demonstrated that the machine torque profiles do not match the human strength curve [4]. In addition, machines also have other issues:

- Inertial resistance is not optimal because weights can be “thrown” which causes uneven force over the range of motion.
- Maximum resistance should be applied at every position in order to increase strength throughout the range.
- Exercises should closely resemble the motion being trained or rehabilitated, to increase strength.

This work was supported by the U.S. Army Telemedicine and Advanced Technology Research Center (TATRC), Ford Detrick, Maryland

C. Carignan is a research associate professor and J. Tang is a robotics engineer with the Imaging Science and Information Systems Center, Georgetown University, Washington DC 20057 USA
crc32@georgetown.edu, jt96@georgetown.edu

- Concentric and eccentric motion are both effective at increasing strength.
- External movement of a disabled limb is still useful in restoring its function.

An actively-controlled exercise machine can help resolve many of these issues. Different types of resistances could be generated and varied over the range of motion. Bidirectional forces could be applied to realize eccentric as well as concentric exercise. A powered machine could be used as an assistive device in the beginning stages of physical therapy and then gradually change over to a resistive training device as strength increases. In addition, strength training could be tailored to individual strength curves, which could slowly be restored to normal following injury or surgery [13].

In this work, a commercial curl machine was motorized in order to actively control the resistance during elbow flexion exercises (see Fig. 1). Active control allows new resistance laws to be implemented that have noninertial and eccentric characteristics and may be hard to generate physically. Resistance can also be automatically adjusted over the range of motion and tuned to individual strength characteristics. In addition, data from onboard sensors can be used to produce performance measures and track patient progress.



Fig. 1. Keiser Arm Curl 250 retrofitted with UltraMotion actuator.

This article begins with a brief review in Section II of previous work in actively-controlled exercise machines. The actuator and drive system used in this study are described

in Section III and a kinematic model is developed. The hardware and control system architecture are outlined in Section IV. Preliminary experimental results for inertial and damping resistances are given in Section V. Conclusions on the implementation of the approach along with some directions for future research are given in Section VI.

II. PREVIOUS WORK

The idea of allowing a user to dynamically “tune” machine resistance is not new. Keiser, Inc. has developed a product line that uses pneumatic pistons instead of weights to provide resistance. The exerciser pushes buttons on the handle to either increase or decrease air pressure in the piston, causing a corresponding increase or decrease in resistance. However, the subject primarily uses this feature as an alternative to moving a pushpin on a weight stack and rarely changes resistance over the course of a repetition.

A motorized version of this concept is the leg extension machine developed at the University of Connecticut [7]. An electric motor that drives two sprockets is used by the machine to engage a cam that increases or decreases the angle of motion of a weighted lever arm. This innovation allows the user to adjust the resistance at any instant during a movement by operating a switch mounted on a grasp handle. Although adjustable, the resistance is still inertial, and the device relies on the human to control the amount of weight.

Automatic control of exercise machines has also been explored. A microprocessor-controlled leg press machine was developed at Georgia Tech in the 1980s [2]. The device used hydraulic pistons that were able to exert up to 300 N of force and drive the lift bar in both vertical and horizontal directions. Thus, the machine was capable of not only tuning the force, but also allowing paths in a plane rather than along a fixed arc or straight line.

Advanced concepts for “smart” exercise machines were under development at UC Berkeley in the mid 1990s and tested on a crank apparatus [10]. Investigators implemented a controller in the form of a nonlinear dynamic damper that would interact passively (stably) with the user. The controller made use of a force-velocity biomechanical model to try to extract maximum power during an exercise and thus elicit more efficient training. These concepts were later implemented into tunable brakes for a Nordic Track machine and a stair stepper exercise machine but did not advance to the commercial development stage [14].

III. DRIVE SYSTEM MODELING

In this study, an arm curl machine was chosen for the prototype exercise device. In addition to being a common upper body exercise, elbow flexion also involves only three major muscle groups: biceps brachii, brachialis, and brachioradialis [9]. Isolation of muscle groups will facilitate clinical evaluation of the machine. To accelerate the development process, a commercial exercise machine was retrofitted with an active drive system rather than building a new device from scratch. This strategy allowed the development to focus on controls and software rather than the hardware.

The commercial version of the Keiser Arm Curl 250 machine using a pneumatic piston to push on a lever which then pulls on the arm curl bar using a rubber belt attached at the other end of the lever as shown in Figure 2. To achieve the high control bandwidths required for this application, the piston assembly was replaced with an UltraMotion actuator, which consisted of a lead screw with 0.125 in (0.3175 cm) pitch driven by an electric motor. The lead screw had a 20 cm stroke (greater than the original piston) and was capable of moving approximately 45 cm/sec unloaded, and 20 cm/sec with a 445 N load.



Fig. 2. View of arm curl machine showing the linear actuator connected to lever and belt drive.

Because of the complexity of the cam, lever, and drive belt assembly and absence of mechanical drawings, the mapping between the lead screw displacement and the elbow flexion angle was determined experimentally. The motor was commanded to move in increments of 5000 encoder counts, and then the angle of the curl bar was read off a protractor suspended from the bar as shown in Figure 3. The results are plotted in Figure 4.

Since the relationship is nonlinear, a third order polynomial curve was fit to the data ($R=0.99997$) resulting in the following approximation between the elbow flexion angle ϕ (rad) and the lead screw displacement x (m)

$$\phi(x) = \phi_0 + 0.3337 + 17.275x - 58.407x^2 + 506.07x^3 \quad (1)$$

where ϕ_0 is the constant offset between the curl bar angle and arm flexion angle. The Jacobian, defined as $J \equiv \partial\phi/\partial x$, relates the elbow flexion velocity to the lead screw velocity and can be found by differentiating (1) with respect to x resulting in

$$J(x) = 17.275 - 116.81x + 1518.2x^2 + 0.0010069x^3 \quad (2)$$

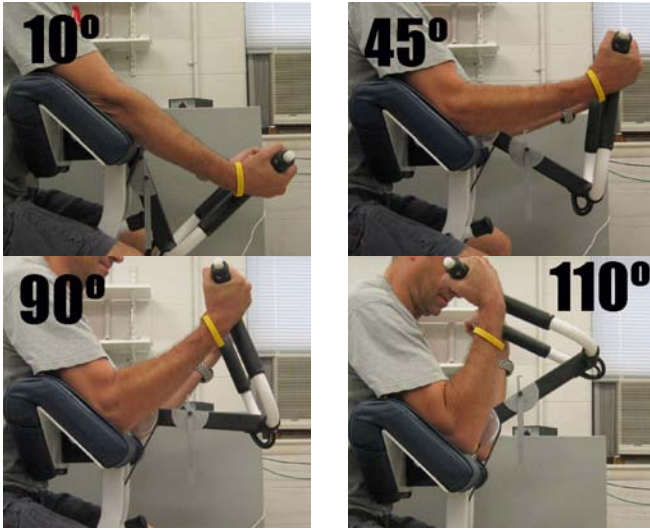


Fig. 3. Bicep curl repetition starting from near full extension through maximum flexion at about 110°. Protractor on arm curl bar was used to generate Figure 4.

The plot of the Jacobian versus the piston displacement is shown in Figure 5. As can be seen from the graph, the lead screw has minimum effect on the flexion angle at approximately 4 cm. By invoking the same duality found in manipulator kinematics [6], the Jacobian also relates the lead screw force F to the flexion torque τ

$$\dot{\phi} = J(x)\dot{x} \quad (3)$$

$$F = J(x)\tau \quad (4)$$

Thus (4) and (2) can be used to determine the torque produced by a given force at the lead screw. The graph in Fig. 6 shows the torque produced by a 500 N force at the piston versus the maximum isokinetic strength profile for elbow flexion [3] scaled to the same maximum peak value. (Note that since the original pneumatic piston on the Keiser machine produces constant force, the former is also the natural strength profile of the machine.) The plots illustrate the large discrepancy in elbow angle at which the maximum torque occurs. However, as stated in the introduction, maximum resistance should be applied at every position throughout the range of motion in order to increase strength, i.e., the human strength profile is optimum. The next section will describe the implementation of haptic interfaces for realizing common resistance laws at the elbow flexor joint.

IV. HAPTIC CONTROL INTERFACE

An UltraMotion lead screw actuator with an Animatics 1720 DC motor was used in place of the pneumatic piston in the original machine (see Fig. 7). The motor drives the lead screw via a rubber pulley with gear ratio 1:1 attached to the shaft. The angle of the motor is determined using a 2000 line incremental encoder mounted on the motor shaft. The encoder is read using the SmartMotor microprocessor which runs a servoloop at 2000 Hz based position commands sent over an RS232 line from the PC.

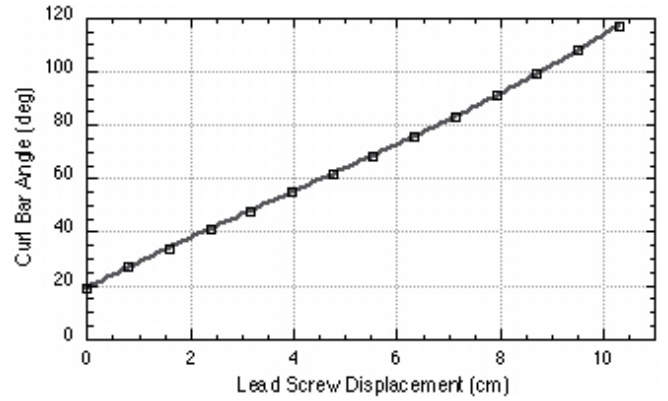


Fig. 4. Angle of curl bar versus the lead screw displacement.

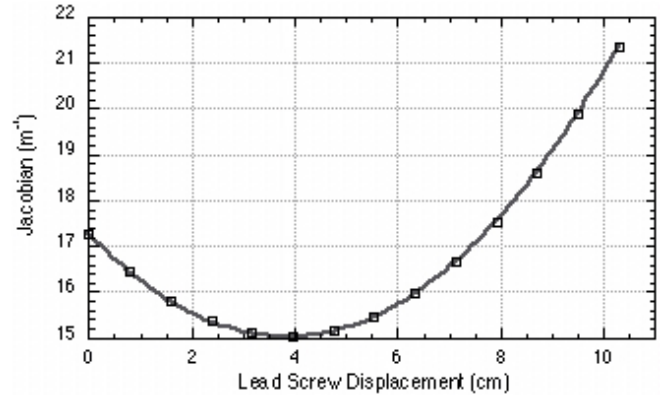


Fig. 5. Jacobian relating elbow flexion velocity to lead screw velocity.

A Sensotec Model 31 tension/compression load cell with 250 lb (1100 N) capacity was used to measure the force at the output of the actuator and was mounted between the output of the lead screw and the coupling to the lever arm on the machine (bottom left of Fig. 7). The load cell voltage and encoder were read directly by a National Instruments PCI-6013 16-bit data acquisition card in the PC rack and processed to produce position commands to be sent back to the SmartMotor by binary data transfer over the RS232 line.

The dual-loop admittance controller shown in Figure 8 was implemented using a PC and onboard microprocessor to control the drive assembly [12], [5]. This approach uses an outer loop wrapped around a force sensor to obtain the desired compliance, while a proportional-derivative (PD) servocontroller is used to drive the lead screw to the target position. Although model feedforward would help reduce the effect of friction and inertia in the drive system, the high PD gains in the servo controller reject most of these disturbances.

The impedance (outer) loop operates by using the force signal from the load cell F_s scaled by the desired admittance to produce a desired velocity \dot{x}_d command for the lead screw. The desired velocity is then integrated and multiplied by the gear ratio between the motor and lead screw drive η (0.3175 cm/rev) to obtain the desired angular position of the motor θ_d . The commanded motor position is then sent from the PC over the serial line to the SmartMotor servocontroller to

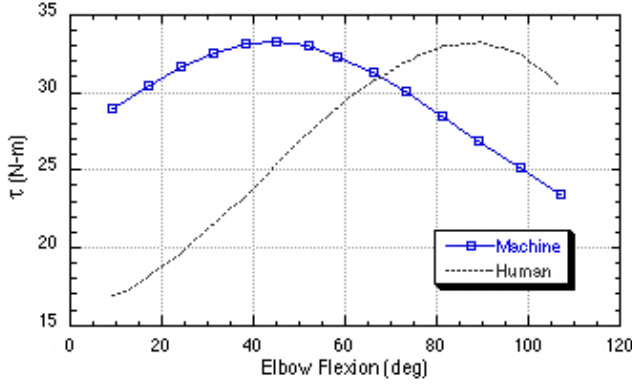


Fig. 6. Elbow flexion torque versus angle for constant force of 500 N applied at the lead screw. The human strength profile is shown for comparison. The force at the hand can be found by dividing the torque by the moment arm of 0.35 m.



Fig. 7. Keiser pneumatic piston (top) versus Ultramotion lead screw actuator driven by SmartMotor (bottom).

drive the lead screw to the desired position.

The resistance law is determined by the desired relationship between the applied force F and the velocity v at the handle. In general terms, this resistance is known as the mechanical “impedance” $Z(s)$ [8] and is represented in the frequency domain as:

$$F(s) = Z(s)V(s) \quad (5)$$

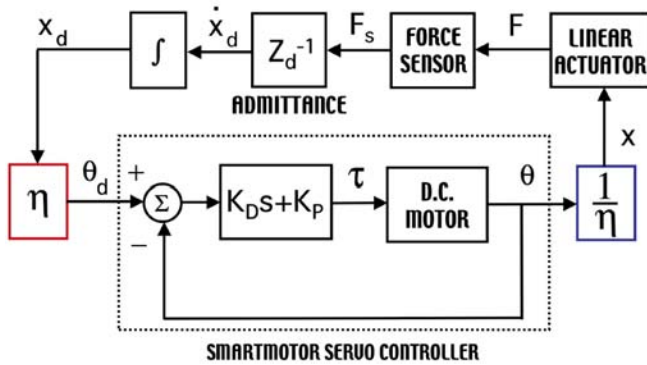


Fig. 8. Admittance control block diagram.

For the pure damper shown in Figure 9, the resistance law is given by

$$F(t) = b_d v(t) \quad (6)$$

$$Z(s) \equiv b_d \quad (7)$$

where b_d is the desired viscous damping coefficient. For the cable-pulley-weight system shown in Figure 10, the resistance law is given by

$$F(t) = m_d \dot{v}(t) - f_w \quad (8)$$

$$Z(s) \equiv m_d s \quad (9)$$

where m_d is the desired mass, g is the gravitational acceleration, and $f_w = m_d g$. (Note that the constant weight of the mass is not included in the impedance.) By contrast, the impedance for a pure spring would be the desired stiffness times the integral operator, $Z(s) = k_d/s$.

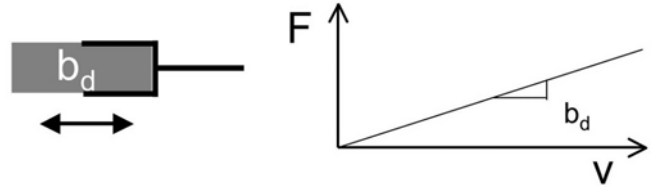


Fig. 9. Damping or “dashpot” resistance profile.

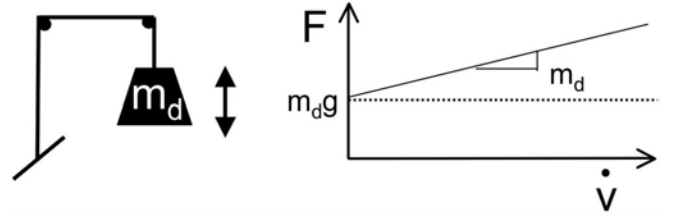


Fig. 10. Cable-weight resistance profile.

These fundamental impedance types can also be superposed to form more complex resistance laws such as the mass-spring-dashpot

$$Z(s) = m_d s + b_d + k_d/s \quad (10)$$

The next section presents some experimental results for inertial and damping impedances.

V. ADMITTANCE CONTROL EXPERIMENTS

Two sets of preliminary experiments were conducted to validate operation of the exercise machine. In the first set, the admittance was set to be a pure resistive damper with an added bias force. In the second set, the admittance at the linear actuator was set to simulate a weight stack driven by a cable-pulley system. The sample rate of the PC was 150 Hz, and the SmartMotor sample rate was 2 KHz. A low pass filter with a bandwidth of 10 Hz was used to filter out force sensor noise and encoder noise due to backlash in the system.

A. Viscous Damping

In these experiments, the desired impedance was a pure damper $b_d = 2500$ N/m/s. A bias force of 200 N was also applied that exponentially rises to its final value with a decay constant of 0.5 cm. Thus, the desired force was

$$F_{des} = -2500\dot{x} - 200(1 - e^{-200(x-x_0)}) \quad (11)$$

The elbow flexion angle and lead screw velocity versus time are shown in Fig. 11. The flexion angle peaks at about 100° , and the velocity of the piston reaches a top speed of about 7 cm/s which is well within even its fully loaded capability.

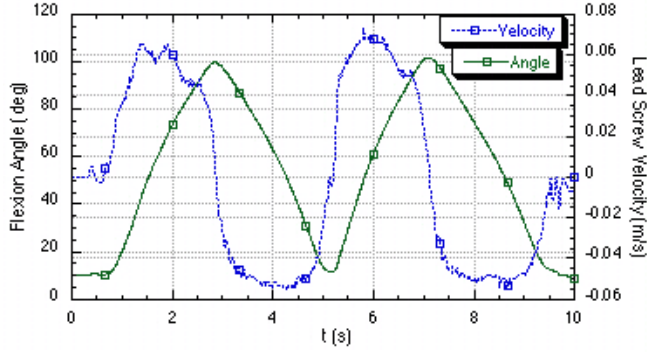


Fig. 11. Arm flexion angle and lead screw velocity during two repetitions with the damping controller.

The lead screw force versus time for two repetitions is shown in Fig. 12 alongside the velocity for reference. The bias force rises rapidly to 200 N, with the remainder of the applied force due to the damping impedance. The viscous damping peaks at about 150 N when the velocity reaches about 6 cm/s, which is consistent with a set damping of 2500 N/m/s. After the elbow begins extension (eccentric motion), the viscous force changes to the same direction as the bias force causing a large drop off in the force curve. As seen in the plot, the lead screw force tracks the desired force in (11) very closely throughout the motion.

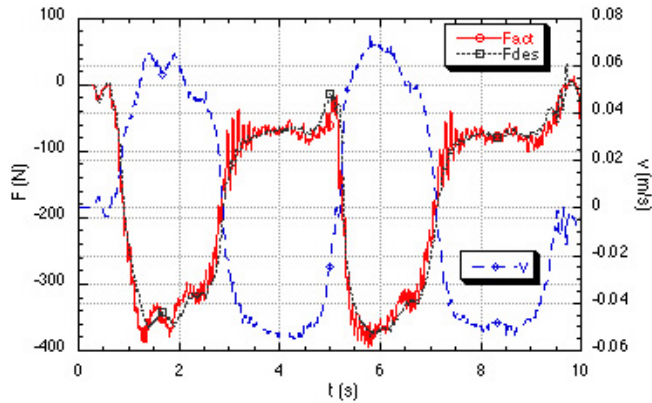


Fig. 12. Lead screw force and velocity versus time for the damping control law.

The resulting torque about the elbow versus the flexion angle for the two cycles is shown in Fig. 13. The top curve

is the concentric (flexion) phase, and the bottom curve is the eccentric (extension) phase. The concentric force peaks at approximately 70° which is midway between the human and machine peaks shown previously in Fig. 6.

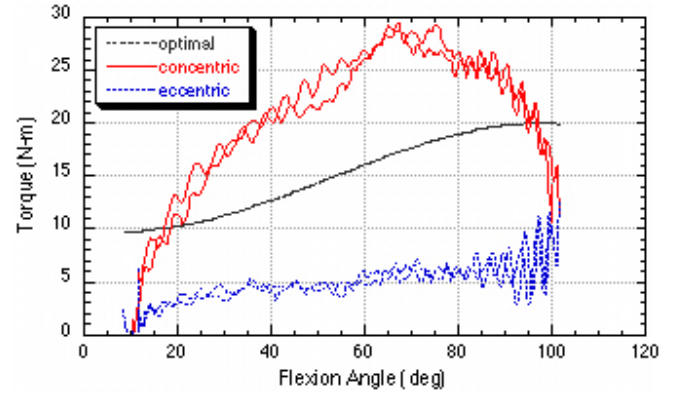


Fig. 13. Flexion torque versus angle for concentric and eccentric phases of the damping control experiment.

B. Cable-Pulley-Weight Simulation

In these experiments, the machine was used to simulate an arm curl resistance provided by a mass on a cable-pulley system. Due to the sample rate limitations of the RS232 port, the controller was not stable for simulated masses below about 200 kg. Even a 6:1 reduction in force between the force applied at the lead screw and handle (moment arm = 0.355 m) would still result in too large of a weight to pull at the handle. Thus, the inertial mass, m_d , was set equal to 500 kg in (9), and the bias force f_w was set equal to 500 N, which is approximately equivalent to a 50 kg weight. Thus, the desired force was

$$F_{des} = -500\ddot{x} - 250 \quad (12)$$

The resulting elbow flexion angle and lead screw force versus time for a pair of arm curl repetitions is shown in Figure 14. The force averages about 250 N (the simulated weight), and the oscillations are characteristic of the undesirable acceleration and deceleration of the mass during elbow flexion and extension seen on many cable-pulley machines. From a subjective point of view, the controller provided a very realistic simulation of a cable-pulley machine although it was impossible to validate that forces were tracked correctly in the absence of acceleration measurements.

The resulting elbow torque as a function of the flexion angle is shown in Fig. 15. The concentric torques at the start of the motion are larger than in the eccentric phase due to the forces needed to accelerate the mass from rest but are correspondingly lower near the peak when the mass reverses direction. The eccentric torques are higher on average in the cruise phase because of the inertial deceleration forces. The torque peaks at approximately 70° which is significantly less than the isokinetic human strength profile superposed on the same graph.

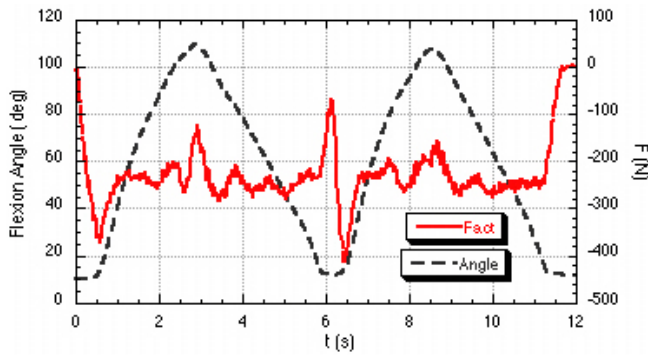


Fig. 14. Flexion angle and lead screw force versus time for cable machine test.

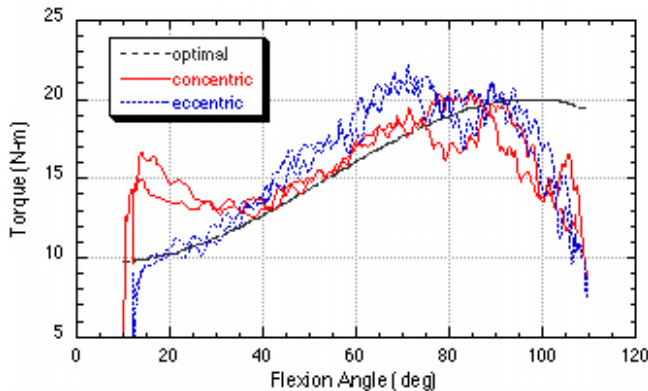


Fig. 15. Flexion torque versus angle for cable machine test.

VI. CONCLUSIONS

A powered exercise machine was developed by retrofitting a commercial arm curl machine with a motorized lead screw drive. An optical encoder and load cell provided sensory feedback to a dual-loop admittance controller implemented on a PC and microprocessor. A 10 Hz low-pass filter was used to suppress electrical noise introduced into the system through the force sensor. Sample rates of the compliance loop were limited to 150 Hz by the RS232 communications link with the SmartMotor, which places an upper bound on the admittance gains that could be simulated. Fortunately, resistance training typically requires high impedance, which drives admittance toward the low end of the spectrum.

Experiments conducted with constant damping and force bias produced a smooth controlled motion, comparable to that of the original machine. The forces produced by the admittance controller accurately tracked the desired forces indicating that the desired damping was achieved. The peak torque occurs at a larger flexion angle than that of a constant force piston, but the peak still falls short of the isometric strength peak near 90°. This is because of the zero boundary condition of the damping resistance at maximum flexion and extension when the velocity goes to zero.

The machine was also used to simulate inertial resistance training using a cable-pulley-weight system. The experiment produced a very realistic haptic interface to the user, even faithfully replicating the “throwing” motion of the weight

stack on a cable often cited as a significant disadvantage of inertial training. Although our goal was to simply emulate an inertial trainer, the oscillations could be reduced or even eliminated by adding some damping to the desired impedance.

Our goal was to show that a motorized exercise machine could be used to achieve a wide variety of resistance laws, and this was demonstrated using damping and inertial resistance laws to simulated classes of well-known passive machines. The next step is to utilize this capability to develop resistance laws that closely match the human strength profile. As was shown here, it is not possible to match the human strength curve using linear impedances due to the hyperpolic-like relationship between muscle force and velocity first noted by Hill [11]. We are currently investigating the variable damping approach developed the team at UC Berkeley in the 1990s [10] for implementation on the arm curl machine, which may require reconfiguring the controller in an impedance implementation.

ACKNOWLEDGMENT

Thanks go to Stephen Roderick and Jean-Marc for their software help and to Mike Perna who made new fittings for the machine. This project was sponsored by the U.S. Army Telemedicine and Advanced Technology Research Center (TATRC) under Grant #W81XWH-04-1-0078.

REFERENCES

- [1] E. Aaberg, *Strength, Speed & Power*. Indianapolis: Alpha Books, 2002.
- [2] W. Book and D. Ruis, “Control of a robotic exercise machine,” in *Proceedings of the Joint Automatic Control Conference*, 1981, pp. WA-2A.
- [3] T. S. Buchanan, S. L. Delp, and J. A. Solbeck, “Muscular resistance to varus and valgus loads at the elbow,” *ASME Journal of Biomechanical Engineering*, vol. 120, pp. 634–639, Oct. 1998.
- [4] L. Cabell and C. J. Zebas, “Resistive torque validation of the nautilus multi-biceps machine,” *Journal of Strength and Conditioning Research*, vol. 13, no. 1, pp. 20–23, 1999.
- [5] C. Carignan and D. Akin, “Achieving impedance objectives in robot teleoperation,” in *Proc. of the IEEE Conference on Robotics and Automation*, 1997, pp. 3487–3492.
- [6] J. Craig, *Introduction to Robotics: Mechanics and Control*, 2nd ed. Reading, Mass.: Addison-Wesley, 1989.
- [7] F. Hatfield, “A new weights machine with dynamically adjustable resistance,” *Sportscience*, vol. 3, no. 1, 1999. [Online]. Available: <http://www.sportsci.org/jour/9901/fch.html>
- [8] N. Hogan, “Impedance control: An approach to manipulation,” *J. of Dynamics Systems, Measurement, and Control*, pp. 1–24, Mar. 1985.
- [9] E. Kneighbaum and K. M. Barthels, *Biomechanics: a qualitative approach for studying human movement*, 4th Ed. Boston: Allyn and Bacon, 1996.
- [10] P. Li and R. Horowitz, “Control of smart exercise machines,” *IEEE/ASME Transactions on Mechatronics*, vol. 2, no. 4, pp. 237–258, dec 1997.
- [11] R. Lieber, *Skeletal Muscle Structure and Function*. Baltimore: Williams and Wilkins, 1996.
- [12] J. Maples and J. Becker, “Experiments in force control of robotic manipulators,” in *Proc. of the IEEE Conference on Robotics and Automation*, Apr. 1986, pp. 695–702.
- [13] K. R. Saul, W. M. Murray, V. R. Hentz, and S. L. Delp, “Biomechanics of the steindler flexorplasty surgery: A computer simulation study,” *The Journal of Hand Surgery*, vol. 28A, no. 6, pp. 979–986, Nov. 2003.
- [14] J. Shields and R. Horowitz, “Adaptive step rate control of a stair stepper exercise machine,” in *Proceedings of the American Control Conference*, Philadelphia, jun 1998, pp. 1058–1062.

7.4 Choi 2007: Transbronchial biopsy ...

Reprint begins on the next page and is three pages.

Transbronchial biopsy based on electromagnetic tracked biopsy forceps

Jae Choi^a, Lucian Gruionu^b, Teo Popa^a, Eric Anderson^c, Kevin Cleary^a

^aImaging Science and Information Systems (ISIS) Center, Department of Radiology, Georgetown University Medical Center, Washington, DC, USA

^bFaculty of Engineering and Technological Systems Management, University of Craiova, Craiova, Romania

^cDivision of Pulmonary, Critical Care, and Sleep Medicine, Department of Medicine, Georgetown University Medical Center, Washington, DC, USA

Abstract Transbronchial biopsy is a common method for tissue acquisition in diagnosis of various pulmonary diseases. However, the procedure has technical limitations when performed on peripheral nodules due to the small size of peripheral airways. To enhance the accuracy of the procedure, we developed an electromagnetically tracked biopsy forceps and evaluated the device with our image-guided system. Our initial experimental results served as a proof of concept of our system. Future work will include additional phantom studies and animal experiments.

Keywords Transbronchial biopsy · Electromagnetic tracking · Virtual bronchoscopy · Biopsy forceps

1. Introduction

Transbronchial biopsy is a common method used to collect tissue for diagnosing pulmonary disease and for staging lung cancer. However, the procedure has technical limitations when performed on peripheral nodules because bronchoscopes in clinical use have diameters that exceed those of the peripheral airways. Hence, it is difficult to reach a target nodule at the lung periphery.

Currently, pulmonologists plan the transbronchial biopsy approach by examining a number of Computed Tomography (CT) images before the procedure. Then, they manipulate a flexible fiberoptic bronchoscope into segmental and subsegmental bronchi as far as the diameter of the bronchoscope permits. Finally, they insert a biopsy forceps through the working channel of the bronchoscope, and perform the biopsy blindly. Consequently, more than half of the procedures fail to reach peripheral targets [1]. When these failures occur, pulmonologists must repeat the procedure or follow up with more invasive methods, such as CT-guided percutaneous needle biopsy or surgical biopsy, that have increased complication rates.

We propose to overcome these limitations and enhance the accuracy of transbronchial biopsy by developing a minimally invasive image-guided system that uses an innovative electromagnetically tracked biopsy forceps. To achieve this goal, we developed a prototype system and electromagnetically tracked forceps and we evaluated this system in phantom studies.

2. Methods

2.1 Electromagnetically tracked (EM) biopsy forceps

Our EM configuration consists of a field generator that creates time dependent electromagnetic fields, the five degree of freedom sensor (a tiny wire coil, 0.8 mm diameter with 8 mm length) placed inside of the forceps, a control unit, and a sensor interface unit that measures the voltage induced in the coils by the changing field. The system can then calculate the position and orientation of the coil in 3D space relative to the field generator. We used the Aurora EM tracking system from Northern Digital Inc (NDI, Waterloo, Ontario, Canada) in this experiment.

The biopsy forceps are from ConMed Corporation (Utica, NY, USA). The exterior metallic sleeve of the biopsy forceps has been replaced for a 2 cm long region (Fig. 1) with a hollow medical grade polyethylene tube of the same exterior diameter (1.8 mm). The sensor coil is placed inside of this tube, close to the jaws, in a fixed position relative to the tube. The sensor axis is parallel with the pulling wire of the forceps. The sensor's electrical wires go through the tube and forceps handle, and are connected to the

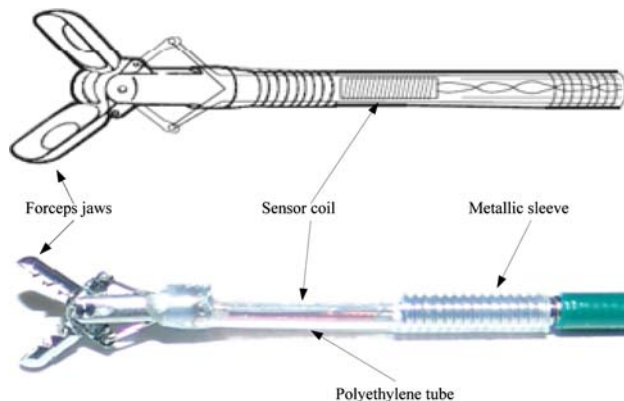


Fig. 1 Wireframe model and a photograph of the EM tracked biopsy forceps

Aurora control unit through the sensor interface. The forceps can be used through a 2 mm minimum bronchoscope working channel like the regular biopsy forceps.

2.2 Image-guided system

We constructed a prototype image-guided system including volume visualization, virtual endoscopy, electromagnetic tracking, and registration [2]. This system accommodates the forceps and provides a user-friendly interface to assist the pulmonologist in targeting these difficult-to-reach lesions. The system also provides an image overlay of the forceps within the CT image volume. The software provides the clinician with 6 views (3 multiplanar views, volume visualization view, virtual bronchoscopy, and optical bronchoscope view). Using this image-guided system, the tracked forceps can be advanced to the simulated tumor site.

2.3 Experiments

To test the accuracy of the forceps, a phantom study was conducted in the interventional suite at Georgetown University Medical Center (Figure 2). Two transbronchial biopsy simulations with a rubber-made bronchial tree model were performed. The workflow of the procedure was as follows:

1. Two target fiducials were placed on the bronchial tree of the phantom as reference targets.
2. A CT scan was taken. A lung volume with 1 mm axial reconstruction was acquired.
3. The registration of the CT space and electromagnetic space was performed by first selecting four surface fiducials in the CT images and then touching each corresponding fiducial with the actively tracked forceps.
4. We performed two transbronchial trials by advancing the forceps to the target fiducial site.
5. For each biopsy, a 3D rotational angiography (DynaCT) image was acquired to measure the accuracy of the biopsy, as determined by the distance between the biopsy device and the target fiducial.

3. Results

Table 1 shows the result of our experiments. We performed two DynaCT scans, and the distances calculated from DynaCT were 11.40 mm (Experiment 1) and 8.33 mm (Experiment 2). Figure 3 shows the visualization from the DynaCT scan for the second experiment. Respectively, we obtained distances of 16.78 and 10.93 mm from our image-guided software. The error range was

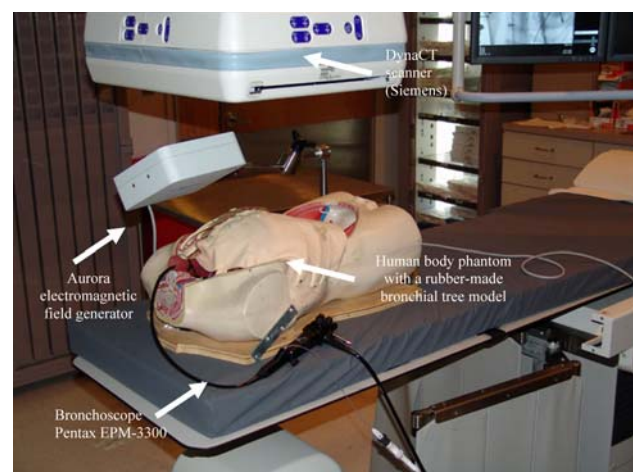


Fig. 2 Experiment Setup. A rubber bronchial tree was put in a human body phantom. We used a Pentax bronchoscope EPM-3300 for the experiment and an Aurora EM tracking system. DynaCT rotational angiography was used to acquire a volume to measure the distance from the biopsy forceps to the target fiducial

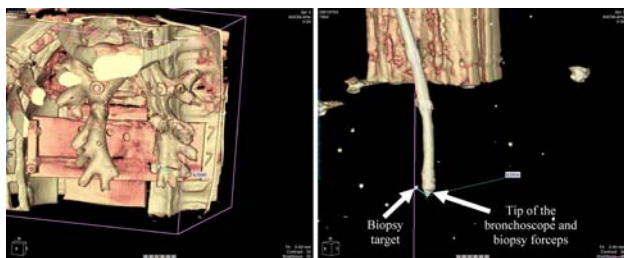


Fig. 3 Visualization from DynaCT scan for the second experiment. The *left figure* visualizes the airway and skin surface, and the *right figure* visualizes the bronchoscope, biopsy forceps, and target fiducial

Table 1 Summary of our experiments (units: mm)

	Distance from CT images	Distance from DynaCT	Distance difference
Experiment 1	16.78	11.40	5.34
Experiment 2	10.93	8.33	2.60

2.60–5.34 mm in this experiment. The RMS (root-mean-square) registration errors were 2.26 and 1.84 mm, respectively.

While these errors were larger than we expected, the overall test showed the feasibility of our approach. Possible reasons for the error include nearby metal in the interventional radiology suite and movement of the airway model.

4. Conclusion

This paper presented our initial experimental results of using a newly developed device, an electromagnetically tracked biopsy forceps. We customized an off-the-shelf biopsy forceps by placing an EM sensor coil inside the biopsy forceps. To test the accuracy of the device, we constructed an image-guided system that included volume visualization, virtual bronchoscopy module, image registration, and electromagnetic tracking. Our initial results show that this device may enhance the accuracy of transbronchial biopsy.

In future work, we hope to improve the accuracy of the tracking by image registration. Specifically, by using the EM tracking system, the search space of the image registration algorithm can be narrowed, which may make it possible to interactively perform registration between the optical video bronchoscopic images and virtual bronchoscopic images. The combination of EM tracking and image registration algorithm might also compensate for respiratory motion during the procedure.

Acknowledgments

This work was funded by US Army grant W81XWH-04-1-0078 and administered by the Telemedicine and Advanced Technology Research Center (TATRC), Fort Detrick, MD, USA. The content of this manuscript does not necessarily reflect the position or policy of the US Government.

References

1. Hopper K, Lucas T, Gleeson K (2001) Transbronchial biopsy with virtual CT bronchoscopy and nodal highlighting. *Radiology* 221:531–536
2. Choi J, Anderson E, Cleary K, Mun S (2005) Real-time virtual assistance for transbronchial needle aspiration: feasibility study. *Chest* 128:327S–328S

7.5 Ding 2008a: Accuracy analysis of ...

Reprint begins on the next page and is seven pages.

Accuracy Analysis of an Image-Guided System for Vertebroplasty Spinal Therapy based on Electromagnetic Tracking of Instruments

Jienan Ding^{ab}, Noureen Khan^{ac}, Patrick Cheng^a, Emmanuel Wilson^a, Vance Watson^a, Kevin Cleary^a, Ziv Yaniv^a

^aImaging Science and Information Systems (ISIS) Center, Dept. of Radiology,
Georgetown University Medical Center, Washington, DC, USA

^b Dept. of Mechanical Engineering, Tianjin University, Tianjin, China

^c School of Medicine, Case Western Reserve University, Cleveland, OH, USA

ABSTRACT

Vertebroplasty is a minimally invasive procedure in which bone cement is pumped into a fractured vertebral body that has been weakened by osteoporosis, long-term steroid use, or cancer. In this therapy, a trocar (large bore hollow needle) is inserted through the pedicle of the vertebral body which is a narrow passage and requires great skill on the part of the physician to avoid going outside of the pathway. In clinical practice, this procedure is typically done using 2D X-ray fluoroscopy. To investigate the feasibility of providing 3D image guidance, we developed an image-guided system based on electromagnetic tracking and our open source software platform the Image-Guided Surgery Toolkit (IGSTK). The system includes path planning, interactive 3D navigation, and dynamic referencing. This paper will describe the system and our initial evaluation.

Keywords: image guidance, vertebroplasty, electromagnetic tracking

1. INTRODUCTION

Each year osteoporosis accounts for an estimated annual incidence of 700,000 fractures; of these, approximately 260,000 are vertebral compression fractures. Vertebroplasty is an increasingly popular medical procedure for treatment of this condition, with 14,152 cases reported in the U.S. in 2001 and case volume increasing to 24,558 in 2003(+73.5%).¹ In conventional vertebroplasty, 2D X-ray projection images are used to guide a trocar consisting of a solid stylet and hollow cannula through the pedicle and into the fractured vertebra. The vertebral body is then stabilized by injecting bone cement through the cannula. This is a difficult procedure to perform, since the trocar is inserted through a relatively narrow pedicle relying solely on 2D X-ray projection images. To gain an understanding of the underlying anatomical structures and the trocar's location physicians acquire many X-ray images. This exposes the patient to ionizing radiation and increases the physician's cumulative exposure. To overcome these drawbacks, we propose to use an image guidance system utilizing electromagnetic tracking, and a pre-operative cone-beam CT. This system replaces the intermittent use of 2D projection images with a dynamic 3D visualization of the anatomical structures and tracked instruments.

We have previously evaluated the use of image guidance for vertebroplasty.² In that work we used CT images and electromagnetic tracking to provide navigation information. Registration of image space to patient space was based on using three tracked needles as registration fiducials. The guidance system displayed the standard axial, sagittal, and coronal views, along with a three dimensional view. The system was successfully used by an experienced interventional radiologist to perform 14 needle insertions in seven vertebrae of an anthropomorphic phantom.

In this paper we describe a new open source version of this software which provides improved guidance using novel volume re-slicing views and a targeting view that are tailored for needle insertion procedures. We evaluate the fiducial localization accuracy when using needles as the registration fiducials and we evaluate the target registration error of our system using an anthropomorphic phantom.

E-mail: zivy@isis.georgetown.edu

2. MATERIALS AND METHODS

We developed an image guidance system for vertebroplasty based on the Image-Guided Surgery Toolkit (IGSTK).³ IGSTK is an open source component based C++ software library which provides an open framework to allow researchers to develop customized image-guided applications with minimal effort. We used the following toolkit components: 1) tracker interface; 2) DICOM image reader; 3) paired-point registration; and 4) visualization components. The library utilizes a state machine architecture for robustness and includes detailed error logging. Our application's Graphical User Interface (GUI) was developed using the Fast Light Toolkit (FLTK), which is one of the GUI toolkits that are compatible with IGSTK.

The navigation system follows the common workflow in which the physician imports a volumetric image data set, plans the trocar insertion trajectory, registers the image data to the patient, and navigates to the target using tracked tools that are overlaid onto the image data.

All volumetric data was obtained in-situ using a cone-beam CT system, the Axiom Artis dFA (Siemens AG, Medical Solutions, Erlangen, Germany). Images are 256x256x221 with a 0.8mm isotropic spacing. The system is installed in the interventional radiology suite, and enables the acquisition of 3D images in-situ. The data is then directly downloaded to a DICOM server running on the navigation system's computer. The use of cone-beam CT does not change any aspect of the navigation system, as compared to the use of standard CT. What it does change is the procedure workflow, which is greatly improved, as there is no need to transport the patient to the CT suite and then back to the interventional suite. In turn this greatly effects the acceptance of such systems into clinical practice.⁴

Tracking was performed with the Aurora system (Northern Digital Inc., Waterloo, Canada). The tracked tools included two 22 gauge MagTrax needles (Traxtal Inc., Toronto, ON, Canada). These are five degree (5D) of freedom tools, with the needle pose known up to a rotation around the needle shaft. To perform the vertebroplasty we use a modified KyphX Osteo Introducer (Kyphon Inc., Sunnyvale, CA, USA), with an embedded 5D Aurora sensor coil. Figure 1(a) shows these components.

All experiments were performed using an anthropomorphic spine phantom comprised of a torso and vertebral column (Sawbones worldwide, Pacific Research Laboratories Inc., Vashon, Washington, USA). The spine was fixed in place inside the torso using urethane foam as shown in Figure 1(b). This was necessary as we have empirically found that the fixation provided by the phantom's structure is not sufficient for performing vertebroplasty. Without this additional fixation the vertebral body exhibited considerable motion, approximately 10mm, which is beyond the motion observed in clinical interventions.

We now describe our novel user interface followed by our needle based registration approach.

2.1 Graphical User Interface

To improve the quality of the image guidance we have designed a Graphical User Interface (GUI), that is tailored for needle based interventions. Preoperatively, we display the standard axial, sagittal, and coronal views. The physician manually identifies a target point on the vertebra and an entry point on the pedicle. The direction defined by these two points defines the desired path. Intraoperatively, once the patient is registered, we provide three re-sliced views, axial, off-axial and off-sagittal. The off-axial and off-sagittal views are re-slice planes that follow the needle axis. That is, these are axial and sagittal views that are tilted so that the needle shaft is in plane. This approach is based on our observations of current clinical practice for needle based biopsies under interventional CT. In these procedures the physician usually tries to align the needle to the fixed imaging plane. We provide similar views by aligning the imaging plane to the needle.

The re-slice plane is obtained as follows. Given the needle shaft direction, \mathbf{u} , and needle tip location \mathbf{p} , both in the image coordinate system, the off-axial re-slice plane is defined as:

$$\mathbf{n}^T(\mathbf{q} - \mathbf{p}) = 0$$

where $\mathbf{n} = \mathbf{u} \times \mathbf{x}$. Note that when $\mathbf{u} \times \mathbf{x} \simeq \mathbf{0}$ we set $\mathbf{n} \equiv \mathbf{z}$. The off-sagittal plane is obtained similarly. Figure 2 illustrates this concept.

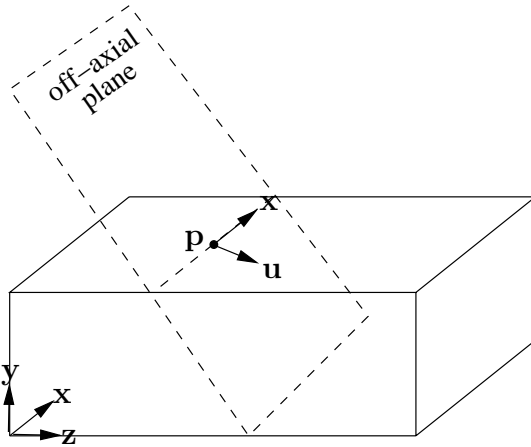


(a)

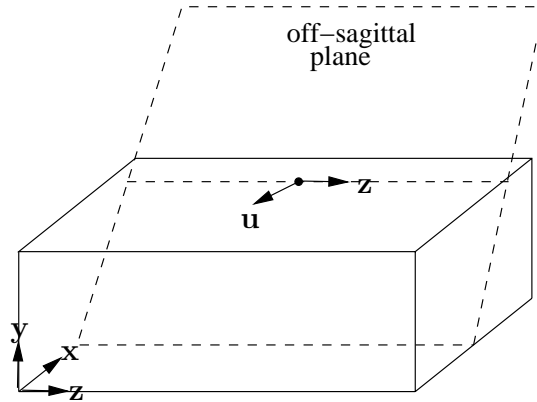


(b)

Figure 1. Hardware components used in the evaluation of the vertebroplasty image-guided navigation system: (a) Electromagnetic system field generator, tracked needles and vertebroplasty trocar, and (b) anthropomorphic phantom, torso and vertebral column.



(a)



(b)

Figure 2. Off axis views: (a) tilting the axial (xy plane) and (b) tilting the sagittal (yz plane) so that the needle shaft is in the viewing plane.

Finally, we also provide a targeting view. The target is displayed as a green sphere, the needle tip as a red ring, and the needle hub as a yellow ring. To align the needle to the planned path the physician centers all three elements. Once the needle is aligned the physician advances the needle using a depth gage which displays the distance between the needle tip and the target. Figure 3 shows our GUI.

2.2 Registration method

To perform registration we use two MagTrax needles. The needles are inserted into the perispinal "musculature" lateral to the spinous process of the vertebra of interest. This is done percutaneously, minimizing trauma to the patient. Once the needles are firmly lodged they form a rigid body with the vertebra. In our system, this pair of needles serves a dual purpose. They are used as fiducials for registration, and once registration is performed the two 5D needles serve as a single 6D dynamic reference frame.

Our image to patient registration is similar to the approach presented in.⁵ It is based on the use of fiducial

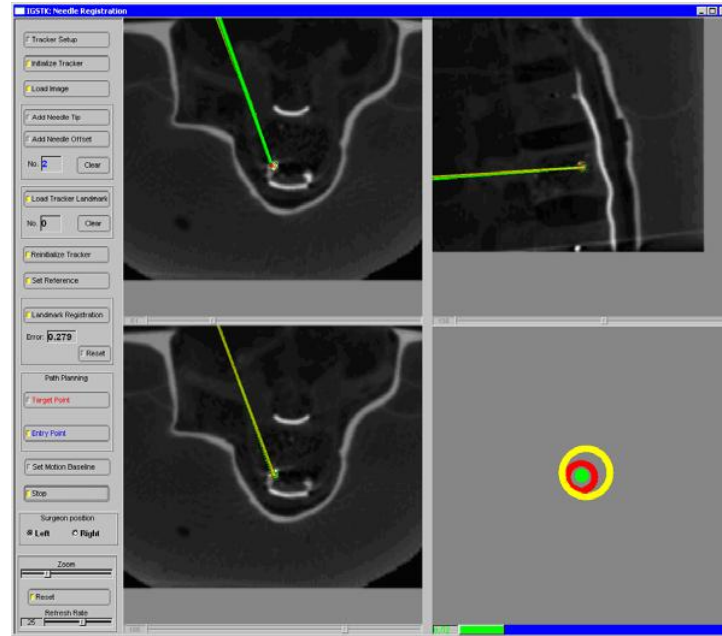


Figure 3. Graphical user interface for vertebroplasty guidance. Axial view (top-left), off-sagittal view (top-right), off-axial (bottom-left), and targeting view (bottom-right).

location and orientation. This enables us to use two fiducials instead of the three required for 3D/3D rigid registration when fiducial location is the only input.

We next describe our registration approach in detail.

First, the two needles are calibrated. The offset between the electromagnetic coil embedded in the needle shaft and the needle tip is estimated using pivot calibration.⁶ In our case, the sensor coil's main axis is aligned with the needle shaft, thus the offset to the needle tip is along a single axis.

Then the needles are inserted percutaneously and a cone-beam CT data set is acquired. The physician manually identifies the needle tip and a point on the needle shaft in the 3D image. This defines the shaft direction \mathbf{u} in the image coordinate system. We then obtain a virtual fiducial point on the needle shaft at a distance of 20mm from the needle tip. Thus, each needle provides us with two points. The choice of a 20mm offset from the needle tip is based on the physical characteristics of our needles. The needle shaft is only locally rigid with respect to the sensor coil. As our sensors are embedded approximately 10mm from the needle tip, we define our virtual point 10mm in the opposite direction from the needle tip. This 20mm segment around the sensor coil does behave as a rigid body.

Finally, we position the electromagnetic field generator next to the patient, read the sensors' locations and orientations and compute the locations of the two needle tips and two virtual points. Rigid registration is then computed automatically using these four points as input to a quaternion based analytic solution.⁷ Figure 4 illustrates the registration point identification in image space and in physical space.

3. EXPERIMENTAL RESULTS

Given that our navigation system uses an electromagnetic tracking system we first need to assess its accuracy in the specific interventional environment. We have previously found that accuracy is highly dependent upon the interventional environment.⁸ In that study we also evaluated the Aurora system in the interventional radiology environment. We concluded that the system's accuracy is sufficient for our procedure, with a median positional

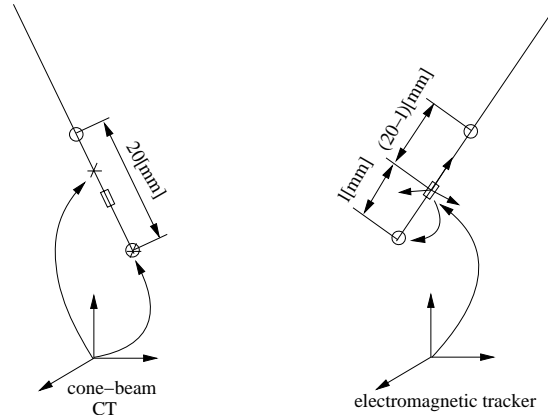


Figure 4. In image space, left coordinate system, the user manually identifies needle tip and needle shaft (x marks) and the registration points (circles) are computed. In physical space, right coordinate system, the location of the sensor coil is obtained and the registration points (circles) are computed using the offset l obtained via pivot calibration.

	data set 1		data set 2	
	tip ($\sigma_x, \sigma_y, \sigma_z$)	shaft ($\sigma_x, \sigma_y, \sigma_z$)	tip ($\sigma_x, \sigma_y, \sigma_z$)	shaft ($\sigma_x, \sigma_y, \sigma_z$)
needle 1	(0.29, 0.75, 0.24)	(0.5, 0.82, 0.39)	(0.39, 1, 0.39)	(0.48, 1.1, 0.97)
needle 2	(0.3, 1.2, 0.61)	(0.87, 1.3, 0.74)	(0.43, 0.83, 0.4)	(0.54, 0.87, 0.55)

Table 1. Standard deviations for fiducial localization, as identified by three operators. The fiducials are the needle tip, and a virtual fiducial located $20mm$ away from the tip on the needle shaft. All measurements are in millimeters.

error of $0.53mm$ and standard deviation of $0.43mm$. This accuracy was obtained when the C-arm based cone-beam CT system was away from its imaging position, which is the setup in which our navigation system is used.

An important aspect of any image guidance system that uses fiducials is the fiducial localization. In our application, we are using tracked fiducials, which enable automatic fiducial localization in physical space. In image space we manually identify the fiducials in the image. In our case the needle tip is well defined, but the point on the needle shaft is a virtual fiducial and is expected to have a higher localization variability. It should be noted that the localization of the virtual fiducial is dependent on the localization of the needle shaft and needle tip. That is, if the needle shaft's true location is identified the virtual fiducial localization will have the same variability as the needle tip localization.

To assess the variability of fiducial localization in the images we performed the following experiment. The MagTrax needles were inserted into the phantom next to the vertebra of interest and a cone-beam CT data set was acquired. We acquired two such data sets. We then analyzed the possible localization variability by having three engineers localize the fiducials (four needle points) ten times in each of the images.

While the needle tip is well defined, the virtual fiducial on the needle shaft is indirectly identified by the operator by marking a point on the needle shaft. We thus expected that the variability in the virtual fiducial localization would be greater than needle tip localization. When analyzing the data we observed that the variability in virtual fiducial localization is comparable to needle tip localization, albeit with a slightly greater variability. Table 1 summarizes this experiment.

The complete system was then evaluated using the anthropomorphic phantom described above. To provide well defined targets we embedded $2mm$ steel ball bearings into the vertebral column in clinically viable locations that correspond to valid trocar positions. The system was then used to perform navigated vertebroplasty. Figure 5(a) shows our experimental setup.

To evaluate the accuracy of our system and the possible procedure variability we had a second year medical student, a fellow, and an attending physician each perform five navigated interventions. An intervention was

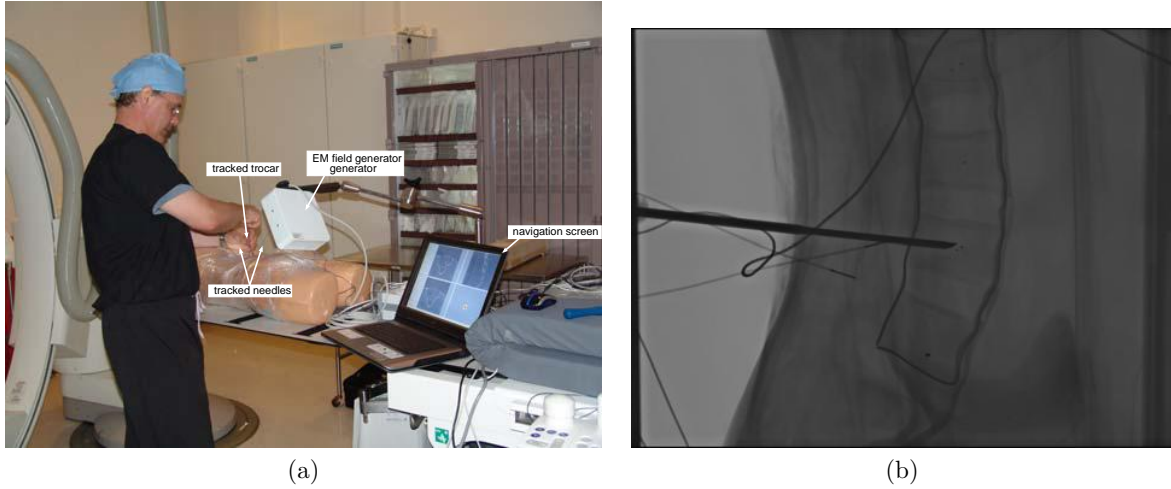


Figure 5. In-vitro experimental setup in the interventional radiology suite, and a lateral projection image acquired after successful navigation which shows the trocar inside the pedicle with its tip near the target ball bearing.

Experiment	student	fellow	attending
1	1.3	0.94	0.6
2	1.44	0.96	1.47
3	2.28	1.2	1.6
4	2.36	1.53	1.63
5	2.62	1.75	1.66
mean(std)	2.0(0.59)	1.28(0.36)	1.39 (0.45)

Table 2. Accuracy results for in-vitro navigated vertebroplasty procedure. Distances were measured between trocar tip and embedded ball bearing using cone-beam CT images. All measurements are in millimeters.

judged as a success if the trocar was completely inside the pedicle, otherwise it was considered a failure. Figure 5(b) shows a lateral image used for qualitative evaluation. We then quantitatively evaluated the accuracy of a successful intervention as the distance between the trocar tip and the target ball bearing center. This distance was measured using a confirmation cone-beam CT scan after each trocar insertion.

All procedures in this experiment were performed successfully by all participants. That is, the trocar did not breach the pedicle. Not surprisingly, the difference between the medical student and practicing physicians was reflected by the accuracy results. The fellow and attending exhibit similar accuracy with the medical student being less accurate. Table 2 summarizes this experiment.

4. DISCUSSION AND CONCLUSIONS

We have described an image-guided navigation system based on cone-beam CT and electromagnetic tracking. This system provides a fully integrated in-situ navigation solution for vertebroplasty, with 3D image acquisition seamlessly integrated with the navigation system. The software is based on the open source Image-Guided Surgery Toolkit (IGSTK).⁹

We evaluated the variability of fiducial localization in the 3D images. This was primarily motivated by the fact that our fiducials are needles and that we use a virtual point on the needle shaft that is indirectly identified by the user. From analyzing the variability of three engineers performing this task we conclude that the localization variability is on the order of $1mm$ which is on the same scale as our voxel sizes ($0.8mm^3$).

We then evaluated the accuracy of our system using an anthropomorphic phantom. Three medical professionals with different skill levels (student, fellow, attending), performed the procedure five times. All procedures were deemed successful with the trocar inserted through the pedicle without breaching it. The variability due to skill

level was reflected by the distance between the trocar tip and planned target point, with the more experienced operators being more accurate.

To improve these results, a semi-automatic method for needle localization is needed, removing the dependence of fiducial localization on the human operator. The next level of system validation should then be done on cadavers.

ACKNOWLEDGMENTS

We would like to thank David Lindisch for his help in conducting the experimental part of this work, Dr. Cory Golding for participating in the phantom experiments, and Neil Glossop of Traxtal Inc. for supplying the MagTrax needles and tracked trocar.

Noureen Khan was supported by a Crile fellowship from the Case Western Reserve School of Medicine.

This work was funded by US Army grant W81XWH-04-1-0078. The content of this manuscript does not necessarily reflect the position or policy of the U.S. Government.

REFERENCES

1. W. B. Morrison, L. Parker, A. J. Frangos, and J. A. Carrino, "Vertebroplasty in the united states: guidance method and provider distribution, 2001-2003," *Radiology* **243**(1), pp. 166–170, 2007.
2. V. Watson, N. D. Glossop, A. Kim, D. Lindisch, H. Zhang, and K. Cleary, "Image-guided percutaneous vertebroplasty using electromagnetic tracking," in *Proc. of Computer Assisted Orthopaedic Surgery*, pp. 492–495, 2005.
3. K. Gary, L. Ibáñez, S. Aylward, D. Gobbi, M. B. Blake, and K. Cleary, "IGSTK: an open source software toolkit for image-guided surgery," *Computer* **39**(4), pp. 46–53, 2006.
4. Z. Yaniv and K. Cleary, "Image-guided procedures: A review," Tech. Rep. CAIMR TR-2006-3, Computer Aided Interventions and Medical Robotics Division, Image Science and Information Systems Center, Georgetown University, April 2006.
5. X. Liu, H. Cevikalp, and J. M. Fitzpatrick, "Marker orientation in fiducial registration," in *SPIE Medical Imaging: Image Processing*, pp. 1176–1185, 2003.
6. W. Birkfellner, F. Watzinger, F. Wanschitz, R. Ewers, and H. Bergmann, "Calibration of tracking systems in a surgical environment," *IEEE Trans. Med. Imag.* **17**(5), pp. 737–742, 1998.
7. B. K. P. Horn, "Closed-form solution of absolute orientation using unit quaternions," *Journal of the Optical Society of America A* **4**(4), pp. 629–642, 1987.
8. E. Wilson, Z. Yaniv, H. Zhang, C. Nafis, E. Shen, G. Shechter, A. D. Wiles, T. Peters, D. Lindisch, and K. Cleary, "A hardware and software protocol for the evaluation of electromagnetic tracker accuracy in the clinical environment: a multi-center study," in *SPIE Medical Imaging: Visualization, Image-Guided Procedures, and Display*, K. Cleary and M. Miga, eds., pp. 65092T–1–65092T–11, SPIE, 2007.
9. K. Cleary, "Image-guided surgery toolkit (igstk)." <http://www.igstk.org/index.htm>, accessed December 19, 2007.

7.6 Ding 2008b: Robotically assisted ultrasound ...

Reprint begins on the next page and is eight pages.

Robotically assisted ultrasound interventions

Jienan Ding^{ac}, Dan Swerdlow^b, Shuxin Wang^c, Emmanuel Wilson^a, Jonathan Tang^a, Kevin Cleary^{a1}

^aISIS Center, Department of Radiology, Georgetown University, Washington, DC, USA

^bGeorgetown University Hospital, Washington, DC, USA

^cDept of Mechanical Engineering, Tianjin University, Tianjin, China

ABSTRACT

The goal of this project is to develop a robotic system to assist the physician in minimally invasive ultrasound interventions. In current practice, the physician must manually hold the ultrasound probe in one hand and manipulate the needle with the other hand, which can be challenging, particularly when trying to target small lesions. To assist the physician, the robot should not only be capable of providing the spatial movement needed, but also be able to control the contact force between the ultrasound probe and patient. To meet these requirements, we are developing a prototype system based on a six degree of freedom parallel robot. The system will provide high bandwidth, precision motion, and force control. In this paper we report on our progress to date, including the development of a PC-based control system and the results of our initial experiments.

Keywords: abdominal procedures, ultrasound guidance, medical robot, force control

1. INTRODUCTION

Ultrasound is routinely used for minimally invasive interventions such as biopsy to obtain a tissue sample for pathological analysis [1]. While typically these procedures can be completed satisfactorily, there are times when it can be difficult to precisely place the needle due to respiration. Finding a direct route to the target site while avoiding ribs and other obstacles can also be problematic. Small targets in particular can be difficult to hit. Finally, a successful biopsy also depends greatly on the hand-eye coordination of the physician, since they must hold the ultrasound probe in one hand and manipulate the needle with the other hand. The probe must be held still both while injecting local anesthesia and for the subsequent procedure needle which must closely follow the local anesthesia tract. Many other ultrasound guided procedures require two hands for manipulation of needles and other instruments. These procedures include placement of drainage catheters, fiducial markers for radiotherapy, and injection of agents such as thrombin or ethanol. Further, if a biopsy sample or aspirate requires handling such as making a cytologic slide it must be passed off to another individual or the ultrasound probe released requiring a second localization for additional samples. Often an assistant is needed to accomplish these procedures.

For these reasons, we are developing a robotic system to hold the ultrasound probe with the proper orientation and force against the abdomen. This system is intended to assist the physician with accurate placement of the needle in abdominal ultrasound-guided interventions. The system is based on an existing six degree of freedom (DOF) parallel robot called SMARTee [2]. This robot includes a force/torque sensor and can be used in both position control and force control applications.

Other researchers have investigated robotics for ultrasound interventions. Salcudean and colleagues at the University of British Columbia in Canada developed a robot-assisted system for ultrasound diagnosis [3]. The system consisted of a master hand controller, a slave manipulator that held the probe, and a computer control system. The system could be used both locally and in a teleoperated mode.

¹ Corresponding author: cleary@georgetown.edu

Hong and colleagues at the University of Tokyo developed an ultrasound based needle insertion robot for percutaneous cholecystostomy (drainage of the gall bladder). The robot included a 5-DOF passive arm to position the needle at the skin entry point and a 2-DOF needle-drive mechanism for automatic needle insertion. A spring mechanism was used to maintain the proper pressure on the skin to ensure good ultrasound images could be obtained.

A master-slave system for ultrasound teleoperation has also been constructed by Troccaz and colleagues in Grenoble, France [4]. The slave robot is a cable-driven non-rigid structure which consists of a parallel positioning mechanism and a serial orientation mechanism. The master robot is a PHANToM device (Sensable Technologies Inc.) which provides force feedback.

In addition to the three groups mentioned here, other researchers have proposed similar devices. However, to the best of the authors' knowledge, none of these devices have been commercialized. Therefore, we believe there is still a need for additional research in this area. In this paper, we present our work in developing a small parallel manipulator with force control for robotically assisted ultrasound procedures.

2. METHODS

2.1 Requirements

The hardware requirements for the robot were generated through a literature review for parameters that determine ultrasound image quality. Salcudean and colleagues measured the ultrasound probe movements and forces during carotid artery examinations [5]. The x, y, and z translational motions were estimated at 130 mm, 150 mm, and 100 mm respectively. Orientations about the x, y, and z axes were estimated as 35 to -50 degrees, ± 75 degrees, and ± 45 degrees. They also measured average velocities to be small, on the order of 5 mm/sec and 3°/sec. The x, y, and z probe forces were also measured and estimated as 3.8N, 4.2N, and 6.4N as sufficient for high ultrasound image quality.

The literature review provided a clear indication of basic hardware requirements. In addition to this, respiratory motion requires a force control ability so that the contact force between the probe and patient skin can be maintained. A successful implementation of the proposed system must therefore ideally have a bandwidth greater than 100Hz for force control. Since the workspace requirements were sufficiently small, the choice between a parallel or serial mechanism robot tended towards a system that could potentially be more accurate. These derived requirements were found to lie within the capabilities of an existing parallel mechanism robotic manipulator, called the SMARTee system. The SMARTee system was the result of research into a novel parallel mechanism manipulator with all revolute joints. The specifications of this system were found to satisfy those deduced from the literature review. To reduce development time and to keep prototyping cost to a minimum, it was decided to retrofit this robot to manipulate the ultrasound probe. The requirements deduced from the literature review and corresponding system specifications for the SMARTee system are summarized in Table 1.

Table 1: Summary of requirements for ultrasound diagnosis and comparable specifications of the SMARTee system.

Specification	Ultrasound diagnosis	SMARTee system
Workspace	100×100×100mm ³	90×90×100mm ³
Roll angle range	(-30,30) degrees	(-30,30) degrees
Yaw angle range	(-30,30) degrees	(-30,30) degrees
Pitch angle range	(-30,30) degrees	(-90,90) degrees
Force control bandwidth	> 100Hz	1000Hz

2.2 System architecture

Mechanical system setup

The SMARTee parallel mechanism system consists of a base plate and top plate connected together by three legs. Each leg consists of three joints and provides six degrees of freedom, a simplified diagram of operation is provided in Figure

1a. Each leg is actuated by two brushed motors (Model No.: D1H18-18-001Z, BEI Motion Systems Co., Goleta, CA, USA) and Hall Effect sensors are used as safety limit switches to sense the travel on each leg. A full description of the kinematic model is provided in [2].

Forces applied at the top plate are sensed by a 6-DOF force/torque sensor from ATI Industrial Automation Inc. (ATI-IA, Apex, NC, USA). The sensor offers high signal-to-noise ratio and provides a force sense limit of 30lbf and 100lbf along the X, Y and Z axes respectively. Torque sense limit is 100lb-in along all axes. A portable ultrasound device, Terason 2000 model (Teratech, Burlington, MA, USA) used in conjunction with the 4C2 model transducer (curved linear, 128 element probe) is used for image acquisition. The Terason was chosen for its lightweight, portable nature, and ease of use. The ultrasound probe is rigidly mounted to the ATI sensor using a straight tube linkage, so that the forces applied to the probe head can be directly measured. Figure 1b shows the retrofitted SMARTee system with the ultrasound probe holder and sensors in place.

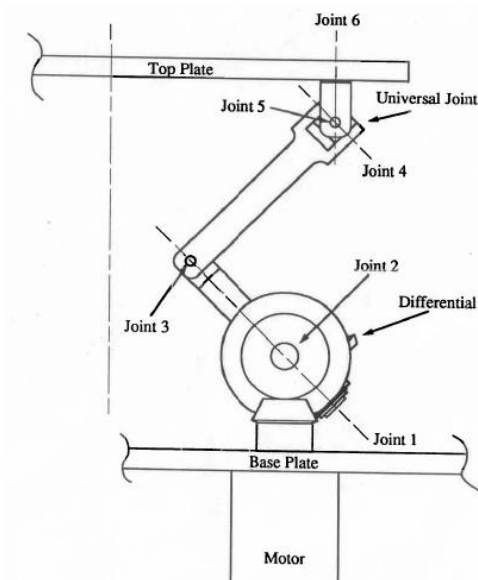


Figure 1a: Structure of each leg



Figure 1b: SMARTee robot retrofitted to hold the ultrasound probe

Control system setup

The original SMARTee configuration relied on a VME architecture running the VXWorks operating system (Wind River Systems, Alameda, CA, USA) utilizing a GreenSpring motion control board and servo amplifiers from Advanced Motion Control. The control system was updated to a PC-based controller system to bring the system up to date and make the system easier to program and use.

The PC-based system consists of a Galil 6-axis Accelera series motion controller card (Galil Motion Control, Rocklin, CA, USA) that communicates to the host PC over the PCI bus. The control system architecture is shown in Figure 2. The left side depicts the control PC which communicates with the ATI force sensor control box through serial (RS-232) connection. The encoders and Hall Effect sensors within the SMARTee robot communicate with the Galil motion control card to determine motor position and limit range respectively. The AMC servo amplifiers from the old system architecture were reused to power the motors, but with the Galil motion card communicating with the servo amplifiers for kinematic calculations and trajectory planning.

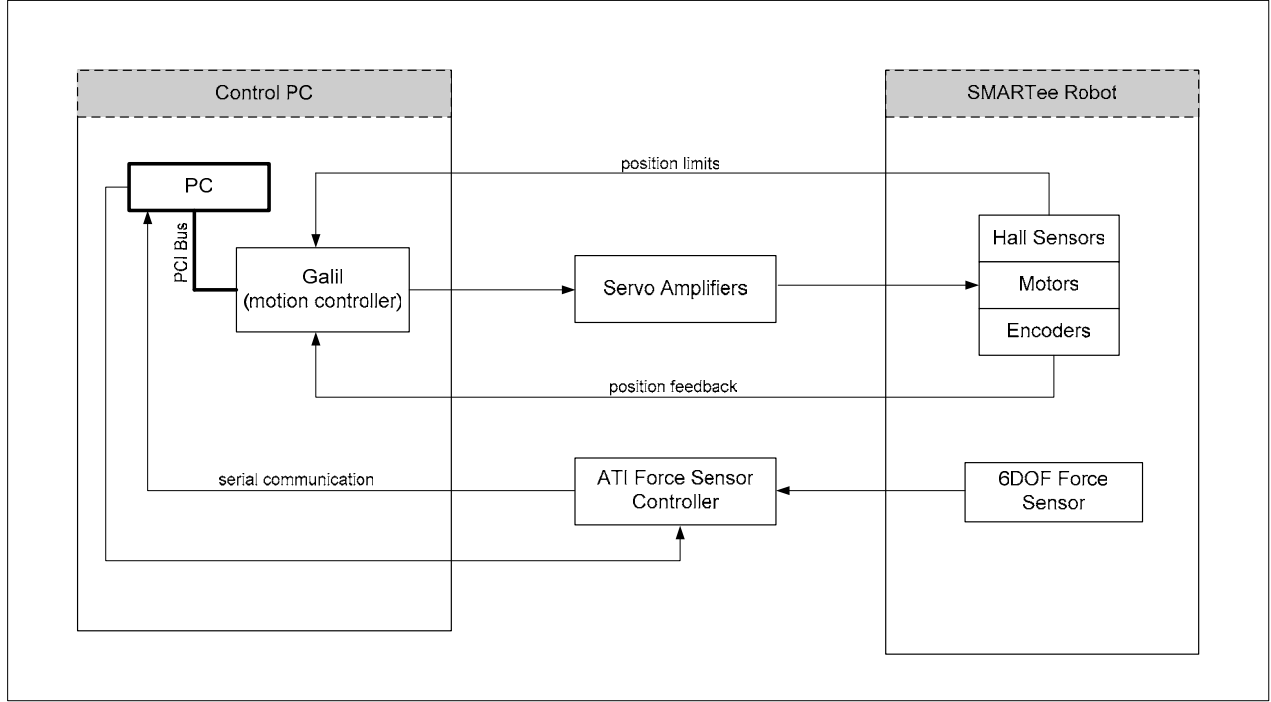


Figure 2: PC based robot control system

System software architecture

The long-term software implementation for the SMARTee system was intended to be built using open source resources and run on a real-time Linux operating system. As this is the first system iteration for ultrasound interventions and the purpose was largely to assess the feasibility of this approach using the SMARTee hardware, it was decided to build the first software release of the system on Microsoft Windows to save development time. This was done as the authors were more familiar with the Windows platform, although a real-time platform would be more suitable for clinical applications.

2.3 Robot kinematics

The notation used to describe the SMARTee kinematics is shown in Figure 3 and was described in [2]. The fixed global reference frame is called the base frame (X_b, Y_b, Z_b) and is located at the bottom center of the base plate. The z-axis is perpendicular to the base plate, the x-axis is in the plane of the bottom of the base plate and is directed toward the universal joint on the first leg, and the y-axis is given by the right hand rule. The base frame is offset a distance Z_{base_offset} from the plane containing the centers of the three universal joints. Another reference frame, called the top frame (X_t, Y_t, Z_t) is located at the top center of the top plate. The z-axis is perpendicular to the top plate, the x-axis is in the plane of the top of the top plate and is directed toward the spherical joint on the first leg, and the y-axis is given by the right hand rule. The top frame is offset a distance Z_{top_offset} from the plane containing the centers of the three spherical joints.

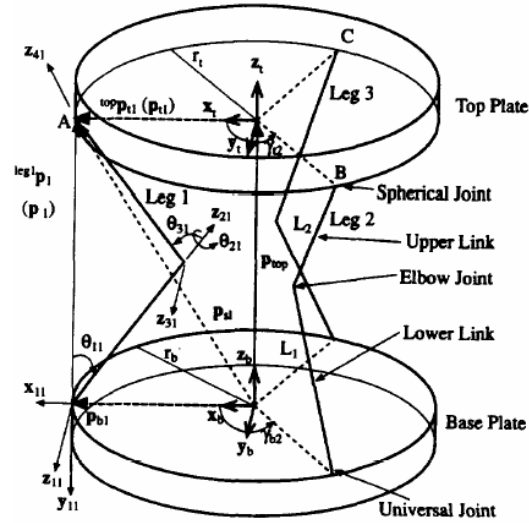


Figure 3: Kinematic model of SMARTee robot [2]

The inverse kinematics for parallel manipulators can typically be described in closed form and the forward kinematics are typically given numerically (the opposite is true for serial manipulators where the forward kinematics are straightforward and the inverse kinematics are more difficult). The inverse kinematics problem for SMARTee can be stated as: Given the position and orientation of the top plate, compute the joint angles on each of the legs. A closed form solution is available which yields the first two angles on the driven joints of each leg. The forward kinematics problem can be stated as: Given the two driven joint angles on each leg, compute the position and orientation of the top plate. As noted above, there usually is not a closed form solution for the forward kinematics of a parallel manipulator. A numerical solution was developed which involves solving a set of three nonlinear equations.

2.4 Impedance control algorithm

The impedance controller was first introduced by Hogan et al [6] and has since been used commonly in robot control including the admittance configuration used here. Since an impedance control algorithm works best when working with compliant surfaces, we chose to use this method to control the SMARTee end effector. In our application, encoders mounted on the motor shafts read the angles of the motors and are then converted to joint angles. The angles are then sent to a forward kinematics module inside the controller to determine the position of the tool tip. Meanwhile, the force sensor mounted on the end-effector will measure the contact force between the robot and patient. The desired move is computed by the impedance controller as a function of the contact force readings and current robot position. The flowchart shown in Figure 4 shows the data flow for the impedance controller. The impedance controller coefficients can be identified and defined in advance to implement a desired performance.

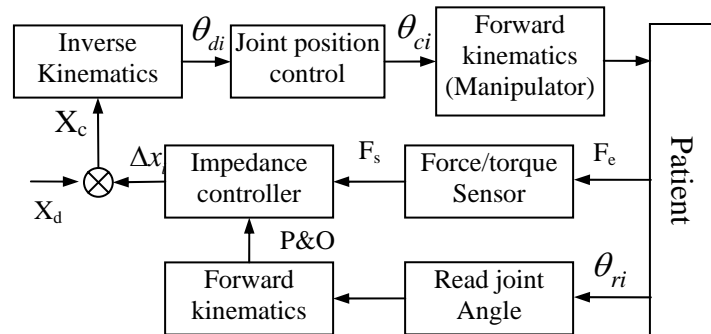


Figure 4: Impedance control data flow

3. RESULTS

Experimental verification of the functionality of the modified SMARTee system was conducted through the course of three tests. The first test was performed on an ultrasound phantom developed at our lab [7]. The phantom was placed directly in front of the robotic system and the robot commanded to apply a steady pressure of 0.6lb. The experimental setup is shown in Figure 5a and an image acquired with the Terason probe with the internal structures within the phantom clearly visible is shown in Figure 5b. Figure 6 provides a plot of the contact force, as measured by the ATI sensor, as the robot automatically adjusts to apply a constant force against the phantom. The impedance controller is able to stabilize the contact force in just less than ten seconds. The successful results from this test provided early validation that the retrofitted SMARTee robot, in conjunction with the impedance control algorithm, is viable for ultrasound imaging.

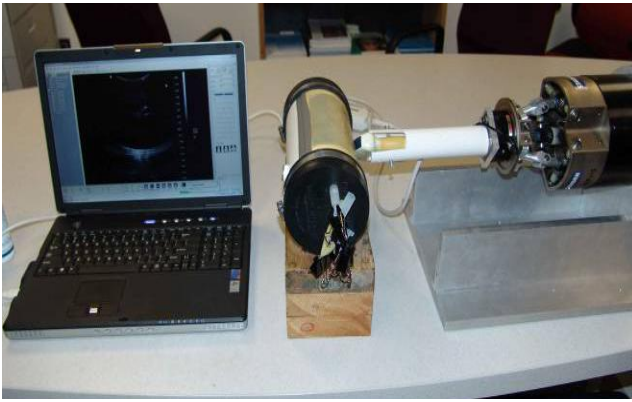


Figure 5a: Experiment setup

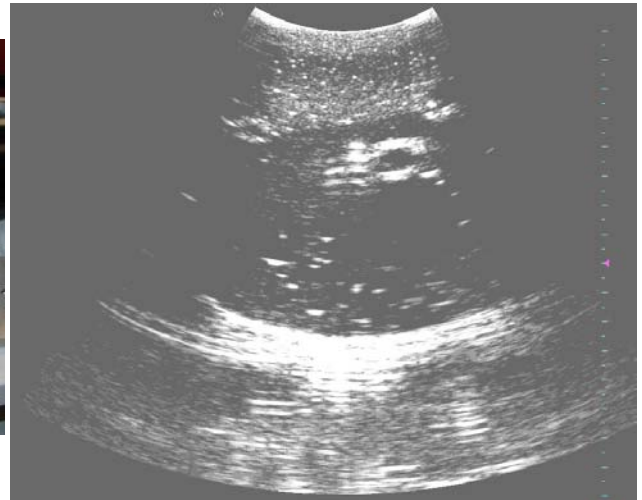


Figure 5b: Image of phantom from ultrasound probe

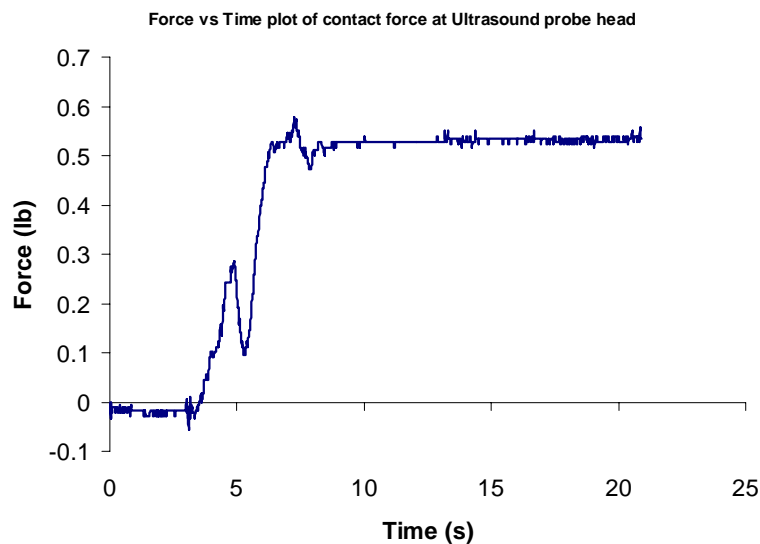


Figure 6: Applied contact force as the robot moves

The second test was conducted to test the reliability of the system under the influence of a varying contact force due to respiratory motion. An anthropomorphic phantom was connected to a variable respirator [8] as shown in Figure 7. The phantom was developed by the URobotics Laboratory at Johns Hopkins Medical Institutions. The robotic end-effector

with the ultrasound probe was positioned to apply a fixed pressure on the phantom. The phantom was then made to respirate at a rate of 20 breaths/min and the robot was able to successfully maintain the contact force.

The reading from the force sensor once the robot had stabilized is shown in Figure 8a. There is a variability of about 0.2lb in the contact force applied by the robot during respiration, which was deemed acceptable for this application. The respiratory rate was extrapolated from the force data by examining the power spectral density plot as shown in Figure 8b. The largest frequency peak exists at 0.24Hz, thereby implying a respiratory rate of 14 breaths/min, which was lower than expected. This discrepancy will be investigated further in future work.



Figure 7: Experimental setup with the anthropomorphic phantom, respiratory pump, and robot

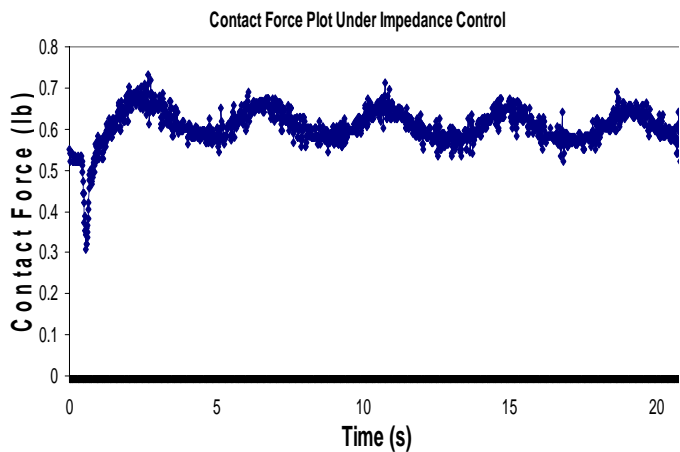


Figure 8a: Comparison of contact force with and without impedance control

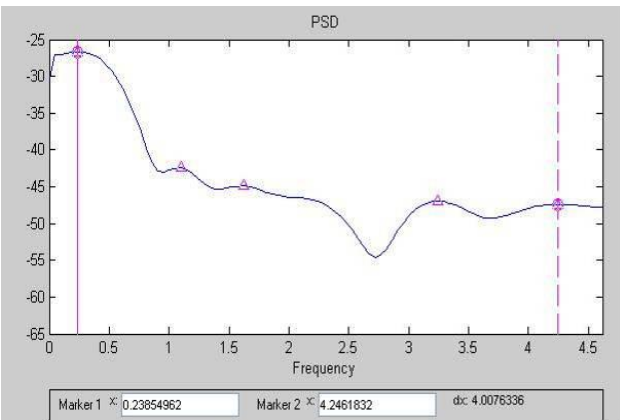


Figure 8b: Power spectral plot to find dominant frequency in force data

4. CONCLUSIONS

Robotically assisted ultrasound has the potential to improve the physician's ability to biopsy difficult targets in the abdomen. The force-controlled parallel mechanism system used here has shown to be a good architecture for this application. This iteration used the existing ATI sensor and controller to relay force and torque information from the sensor to the host PC via serial communication. Future iterations could include a Measurement Computing DAQ card used in conjunction with the Comdi open-source toolkit for digital I/O which would considerably speed up communications with the sensor.

5. ACKNOWLEDGMENTS

This project is part of a collaboration between Georgetown University and Tianjin University to develop medical robotics systems. This work was funded by U.S. Army grant W81XWH-04-1-007, administered by the Telemedicine and Advanced Technology Research Center (TATRC), Fort Detrick, Maryland. The content of this manuscript does not necessarily reflect the position or policy of the U.S. Government. We thank our colleague Craig Carignan for valuable assistance with the controls portion of the work.

REFERENCES

- [1] Sheth, S., Hamper, U.M., Stanley, D.B., Wheeler, J.H. and Smith, P.A., *US guidance for thoracic biopsy: a valuable alternative to CT*. Radiology, 1999, 210(3), 721-726.
- [2] Cleary, K. and Brooks, T., *Kinematic analysis of a novel 6-DOF parallel manipulator*. Robotics and Automation, IEEE International Conference, 1993, 708-713.
- [3] Abolmaesumi, P., Salcudean, S.E., Wen-Hong, Z., Sirouspour, M.R. and DiMaio, S.P., *Image-guided control of a robot for medical ultrasound*. Robotics and Automation, IEEE Transactions on, 2002, 18(1), 11-23.
- [4] Vilchis, A., Troccaz, J., Cinquin, P., Masuda, K. and Pellissier, F., *A new robot architecture for tele-echography*. Robotics and Automation, IEEE Transactions on, 2003, 19(5), 922-926.
- [5] Salcudean, S.E., Bell, G., Bachmann, S., Zhu, W.H., Abolmaesumi, P. and Lawrence, P.D., *Robot-Assisted Diagnostic Ultrasound - Design and Feasibility Experiments*. MICCAI, 1999, 1062-1071.
- [6] Hogan, N., *Impedance control - An approach to manipulation: Part I,II*. Int.J.of Rototics Res., 1985. **107**: p. 1-24.
- [7] Strulik, S., Cho, M., Collins, B., Khan, N., Banovac, F., and Cleary, K., *Fiducial movement following small peripheral lung tumor image-guided CyberKnife stereotactic radiosurgery*. To be published in this volume, Proceedings of SPIE Medical Imaging 2008, Visualization, Image-Guided Procedures, and Modeling, Vol. 6918, Paper 6918-45.
- [8] Lin, R., Wilson, E., Tang, J., Stoianovici, D., Cleary, K., *A computer-controlled pump and realistic anthropomorphic respiratory phantom for validating image-guided systems*. Proceedings of SPIE Medical Imaging 2007, Vol. 6509: 65090E.

7.7 Enquobahrie 2007: The image-guided surgery ...

Reprint begins on the next page and is 13 pages.

The Image-Guided Surgery Toolkit IGSTK: An Open Source C++ Software Toolkit

Andinet Enquobahrie,¹ Patrick Cheng,² Kevin Gary,³ Luis Ibanez,¹ David Gobbi,⁴ Frank Lindseth,⁵
Ziv Yaniv,² Stephen Aylward,¹ Julien Jomier,¹ and Kevin Cleary²

This paper presents an overview of the image-guided surgery toolkit (IGSTK). IGSTK is an open source C++ software library that provides the basic components needed to develop image-guided surgery applications. It is intended for fast prototyping and development of image-guided surgery applications. The toolkit was developed through a collaboration between academic and industry partners. Because IGSTK was designed for safety-critical applications, the development team has adopted lightweight software processes that emphasizes safety and robustness while, at the same time, supporting geographically separated developers. A software process that is philosophically similar to agile software methods was adopted emphasizing iterative, incremental, and test-driven development principles. The guiding principle in the architecture design of IGSTK is patient safety. The IGSTK team implemented a component-based architecture and used state machine software design methodologies to improve the reliability and safety of the components. Every IGSTK component has a well-defined set of features that are governed by state machines. The state machine ensures that the component is always in a valid state and that all state transitions are valid and meaningful. Realizing that the continued success and viability of an open source toolkit depends on a strong user community, the IGSTK team is following several key strategies to build an active user community. These include maintaining a users and developers' mailing list, providing documentation (application programming interface reference document and book), presenting demonstration applications, and delivering tutorial sessions at relevant scientific conferences.

KEY WORDS: Image-guided surgery, open source, visualization, registration, tracking and agile software development

INTRODUCTION

Minimally invasive procedures are becoming increasingly popular in today's healthcare system. Patients prefer these procedures to open

surgeries because they cause less trauma to the body and result in faster recovery times. Interventional radiologists and surgeons are also becoming more experienced and comfortable performing these procedures. Interventional radiologists use instruments such as needles and catheters to perform diagnostic and therapeutic procedures guided by images. Examples of diagnostic procedures include biopsy of suspicious lesions and injection of contrast agents for computed tomography (CT) angiography. Therapeutic procedures include using stents to open clogged arteries and radiofrequency ablation techniques to destroy tumor tissues.

In image-guided surgery procedures, the surgical instruments are placed through incisions guided by preoperative images. To track the position of the surgical instruments, a tracking system is used. The tracking system shows the position and orientation of the surgical instrument

¹From Kitware Inc., Clifton Park, NY, 12065, USA.

²From the Imaging Science and Information Systems (ISIS) Center, Department of Radiology, Georgetown University Medical Center, Washington, DC, 20007, USA.

³From the Division of Computing Studies, Arizona State University, Mesa, AZ, 85212, USA.

⁴From Atamai Inc., London, ON, N6B 2R4, Canada.

⁵From the SINTEF Health Research and the National Center for 3D Ultrasound in Surgery, Trondheim, Norway.

Correspondence to: Andinet Enquobahrie, Kitware Inc., Clifton Park, NY, 12065, USA; Tel: +1-1518-3713971; e-mail: andinet.enquobahrie@kitware.com

Copyright © 2007 by Society for Imaging Informatics in Medicine

doi: 10.1007/s10278-007-9054-3

in the context of preoperative images. The preoperative image is aligned with the patient coordinate system using a technique called registration. The tracking system is used to track the position of the surgical instrument. A typical image-guided system is shown in Figure 1.

The use of open source software for medical procedures like image-guided surgeries is gaining more acceptances in recent years. With US government agencies such as the National Institutes of Health (NIH) and the National Science Foundation encouraging open source software development, more research groups are developing and releasing software as open source. The Visualization Toolkit (VTK) and the Insight Toolkit (ITK) are prime examples of the success of open source software projects. VTK¹, originally developed at GE Global Research and now supported by Kitware, provides a wide range of algorithms in computer graphics, image processing, and visualization. The toolkit has a wide user base with thousands of users worldwide. VTK provides advanced multidimensional visualization algorithms and modeling techniques such as implicit modeling, polygon reduction, mesh smoothing, cutting, contouring, Delaunay triangulation, and parallel computing.

ITK², developed under the support of the US National Library of Medicine (NLM) at the NIH, provides advanced registration and segmentation algorithms. The toolkit contains state-of-the-art algorithms and continues to be updated and maintained with supports from NLM. Similar to VTK, the software is implemented in the C++

programming language and provides wrappers for Tcl, Python, and Java interpreters.

The composition of the ITK development team demonstrates the strength of a collaborative effort that is greatly emphasized in an open source project. The initial development team consisted of three commercial partners (GE Corporate R&D, Kitware, and MathSoft) and three academic partners (University of Tennessee, University of North Carolina, and University of Pennsylvania). Other developers have since joined the effort, and to date, over 50 developers have directly contributed code to the toolkit.

Several benefits have contributed to the increased popularity and acceptance of open source software. Some of the main benefits are listed below.

- 1) Open source software encourages collaboration between academic, commercial, and government institutions by providing a common software base and creating a sense of community.
- 2) Open source software saves resources by avoiding “reinventing the wheel.” Oftentimes, a researcher wastes valuable time and resources implementing basic infrastructure. Using open source implementations of basic functionality, researchers are able to focus on new research efforts.
- 3) Open source software provides a valuable resource for educational purposes. The best way to learn software development is by studying how other developers have done it and by attempting to improve it.



Fig 1. Image-guided system for brain surgery showing the optical tracking system at the *top right* and the display overlay on the *far left*. The patient is under the blue cover in the *middle*. (Photograph courtesy of Richard Bucholz, MD, St. Louis University).

- 4) Open source software provides implementation of reference or benchmark algorithms for validation and verification purposes.
- 5) Open source software, when distributed under the appropriate license, permits users to try out the technology without restrictions, and this ultimately encourages rapid dissemination of the technology and the growth of a user community.

With the above benefits, open source toolkits are making the transition into mission-critical applications. Forrester's study³ has shown that companies are rapidly expanding their use of open source software from simple applications (such as email) to mission critical applications (such as customer contact applications). In the medical field, software applications developed using open source toolkits have been submitted to the Food and Drug Administration (FDA) for approval in clinical studies. Although the FDA does not have any specific policy on open source software, the FDA requires that software included in medical devices should be developed following a process for which a quality control system is in place. As one example, the FDA recently approved a single center clinical trial for an electromagnetically tracked lung biopsy application developed using image-guided surgery toolkit (IGSTK) that will begin shortly at Georgetown University Medical Center.

IGSTK, the focus of this paper, is an open source software project developed with support from the National Institute of Biomedical Imaging and Bioengineering (NIBIB) at NIH. It is a cross-platform C++ library that provides the basic components necessary to develop an image-guided system. It is intended for fast prototyping and development of robust image-guided applications. The initial version of the software was released in February 2006 at the SPIE Medical Imaging Conference in San Diego, and an updated version was released at the same meeting in February 2007. The software and documentation is freely available for download at <http://www.igstk.org>.

The toolkit was developed through a collaboration between academic and industry partners. The principal investigator of the project is Kevin Cleary at the Imaging Science and Information Systems (ISIS) Center in Georgetown University. ISIS is a medical research and development

institute that specializes in information and imaging technology in healthcare. The commercial partner is Kitware, a small company specializing in open source software. Kitware also provides commercial consulting services for ITK and VTK. Expertise in tracking systems was provided by Atamai (Ontario, Canada). Experts from Arizona State University provide guidance in software process management and object-oriented technologies. The image-guided research group at Selskapet for Industriell og Teknisk Forskning ved Norges Tekniske Høegskole (SINTEF) in Trondheim, Norway, has also recently joined the project to provide a strong focus on end-user applications.

The remainder of the paper consists of five parts. "IMAGE-GUIDED MEDICAL PROCEDURES—BACKGROUND" presents background information about image-guided medical procedures. "IGSTK SOFTWARE PROCESS" describes the software process adopted for IGSTK development. This is followed by a discussion of the architecture in "IGSTK ARCHITECTURE." "BUILDING AN IGSTK COMMUNITY" outlines the strategies being followed to build the IGSTK user community. Finally, conclusions are presented in "CONCLUSION."

IMAGE-GUIDED MEDICAL PROCEDURES—BACKGROUND

Image-guided procedures are rapidly replacing open surgical procedures in clinical practice. The main driving forces behind the wide acceptance of image-guided procedures are technological advancements in medical imaging, registration algorithms, visualization technologies, and tracking systems.

To use medical images for surgical navigation, we first need to make them correspond with the patient's anatomy in a step called *registration*. Registration is the technique of computing a spatial transform that maps points from one coordinate system to another. When we can accurately register the image coordinate system with the patient coordinate system, we can use the images for virtual guidance of surgical instruments.

Registration categories include registration of preoperative images to intraoperative images, registration of preoperative images to the patient coordinate system, and registration of images from

different modalities. Registration techniques include image intensity-based, feature-based (fiducial landmarks or anatomical landmarks), surface-based, and stereotactic frame-based techniques⁴. For example, x-ray fluoroscopy, which accounts for more than 90% of intraoperative imaging for guidance, generates 2D projection images. An interventional radiologist has to mentally register these 2D projection images to the 3D patient body to perform the procedure. This can create ambiguity and inaccuracies in the procedure. However, by registering a preoperative 3D magnetic resonance or CT image to the x-ray fluoroscopic image, 3D image information can be used to guide the procedure.

Another essential component of an image-guided system is the tracking device. A tracking system measures the real-time position of surgical tools and fiducials attached to the patient's anatomy. Visual virtual feedback can be provided by generating computer graphic images where these changing positions of the surgeon's tools are superimposed on the preoperative or intraoperative images. This helps the surgeon navigate inside the patient's body by using the overlaid images. The main tracking technologies used in image-guided procedures are optical and electromagnetic tracking. Optical tracking systems require an unobstructed line of sight between the tracked sensors and tracking device. Electromagnetic tracking system uses small sensor coils that can be embedded in instruments and does not have the line of sight limitation. Thus, electromagnetic tracking can be used to track instruments inside the body. However, electromagnetic tracking is affected by ferromagnetic objects in its working volume, and

care must be taken to have a relatively metal-free environment. An example electromagnetic tracking system is shown in Figure 2.

To provide visual feedback to the clinician, computer graphic images are generated where registered information of the tracked instrument and preoperative or intraoperative image is presented in a meaningful manner. Visualization plays a key role in this regard. The visualization application typically displays the virtual anatomy around the location of the surgical instrument in real-time. Traditionally, slice-by-slice or multi-planar display views are used. The images can also be reformatted to create a view perpendicular to the direction or plane of the probe. With the increase in the resolution of medical images, surface and volume rendering techniques are commonly used to display 3D information of the surgical scene. Surface rendering techniques display surface structures identified within the image (the surface could be generated using contouring techniques). This may be augmented by texture mapping in which the original data is pasted on selective surfaces. For volume rendering, a ray-casting technique is commonly used where the displayed intensity of the image at each point is a function of the characteristics of the structures traversed by the ray. Advancement in these visualization algorithms and computing power has made interactive rendering of 3D scenes possible in surgical procedures.

IGSTK SOFTWARE PROCESS

IGSTK is designed to develop safety-critical applications. This has led us to adopt a lightweight



Fig 2. Aurora electromagnetic tracking system components, sensors, and measurement volume. The left picture shows (from left to right) the control unit, sensor interface device, and electromagnetic field generator. The middle picture shows the sensor coils (red objects in the middle of the figure). The right picture shows the measurement volume which is a 500 mm cube starting 50 mm from the front of the field generator (Image courtesy of Northern Digital, Inc.).

software process that emphasizes safety and robustness while also supporting geographically separated developers. The adopted software process is philosophically aligned with agile software development methods where lightweight, iterative, incremental, and test-driven development principles are applied. The IGSTK software process has four major components: source code version control system, build and release management, automated testing, and communication and documentation.

Version Control System

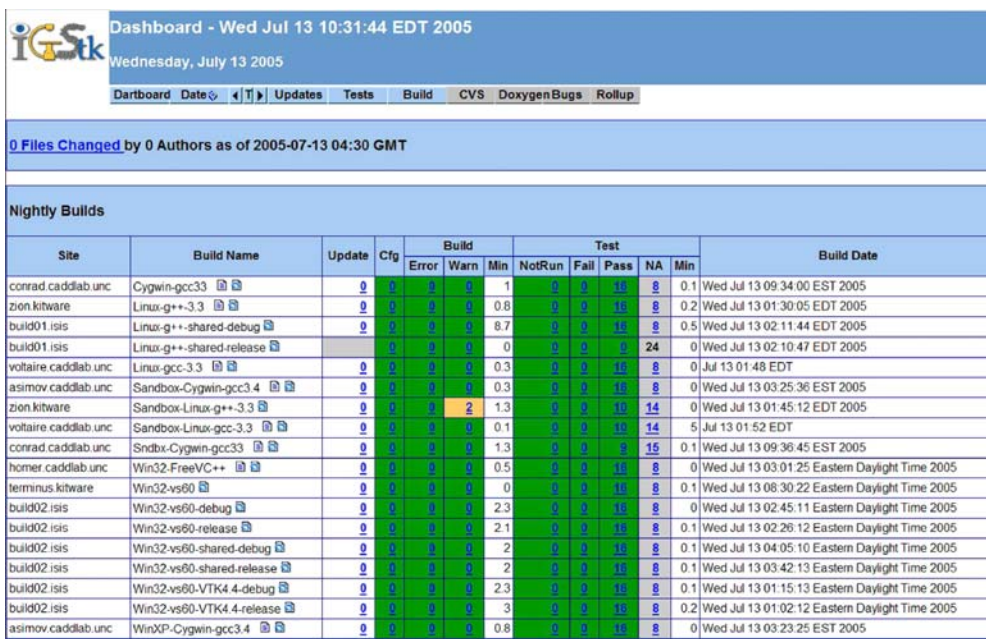
Managing source code versions is essential in an iterative software development process. IGSTK uses the concurrent versioning system (CVS). CVS follows a client-server model where a server maintains a central repository for developers to check out, modify, and merge changes back to the code base. CVS allows simultaneous edits and branching and makes releases easier. IGSTK has two code repositories: a main CVS and a sandbox. The main CVS repository contains the version of the code that has been reviewed, well-tested, and approved for integration. The code in the main CVS repository adheres to all the quality software policies established in IGSTK. On the other hand, the sandbox is a testbed for developers to

experiment on new ideas before integration with the rest of the toolkit, and it is subjected to less stringent quality requirements.

Build and Release Management System

Configuring and managing the build process of a large project is a challenging task in software development. Large projects employ various tools and libraries. Developers use different compilers and development environments for coding. The build process should be able to coordinate all these tools. The task is particularly formidable for a cross-platform toolkit like IGSTK. The cross-platform project configuration task includes selecting an appropriate compiler, finding required packages and libraries, specifying include header file and library file paths, and selecting the appropriate compiler flags and options consistently across platforms.

The IGSTK configuration and build process is controlled by Cmake⁵. CMake is a cross-platform build system. CMake simplifies the configuration process by using platform-independent configuration files to generate native build files such as UNIX makefiles and Visual Studio workspaces for the user-selected compiler. CMake automates the configuration process and makes it possible to



Dashboard - Wed Jul 13 10:31:44 EDT 2005
Wednesday, July 13 2005

Dashboard Date Updates Tests Build CVS Doxygen Bugs Rollup

0 Files Changed by 0 Authors as of 2005-07-13 04:30 GMT

Nightly Builds

Site	Build Name	Update	Cfg	Build			Test					Build Date
				Error	Warn	Min	NotRun	Fail	Pass	NA	Min	
conrad.caddlab.unc	Cygwin-gcc33	0	0	0	0	1	0	0	15	8	0.1	Wed Jul 13 09:34:00 EDT 2005
zion.kitware	Linux-g++-3.3	0	0	0	0	0.8	0	0	10	8	0.2	Wed Jul 13 01:30:05 EDT 2005
build01.isis	Linux-g++-shared-debug	0	0	0	0	8.7	0	0	10	8	0.5	Wed Jul 13 02:11:44 EDT 2005
build01.isis	Linux-g++-shared-release	0	0	0	0	0	0	0	24	0	0	Wed Jul 13 02:10:47 EDT 2005
voltaire.caddlab.unc	Linux-gcc-3.3	0	0	0	0	0.3	0	0	15	8	0	Jul 13 01:48 EDT
asimov.caddlab.unc	Sandbox-Cygwin-gcc3.4	0	0	0	0	1.3	0	0	10	8	0	Wed Jul 13 03:25:36 EST 2005
zion.kitware	Sandbox-Linux-g++-3.3	0	0	0	2	1.3	0	0	10	14	0	Wed Jul 13 01:45:12 EDT 2005
voltaire.caddlab.unc	Sandbox-Linux-gcc-3.3	0	0	0	0	0.1	0	0	10	14	5	Jul 13 01:52 EDT
conrad.caddlab.unc	Sndbx-Cygwin-gcc33	0	0	0	0	1.3	0	0	5	15	0.1	Wed Jul 13 09:36:45 EST 2005
homer.caddlab.unc	Win32-FreeVC++	0	0	0	0	0.5	0	0	10	8	0	Wed Jul 13 03:01:25 Eastern Daylight Time 2005
terminus.kitware	Win32-vs60	0	0	0	0	0	0	0	10	8	0.1	Wed Jul 13 08:30:22 Eastern Daylight Time 2005
build02.isis	Win32-vs60-debug	0	0	0	0	2.3	0	0	10	8	0	Wed Jul 13 02:45:11 Eastern Daylight Time 2005
build02.isis	Win32-vs60-release	0	0	0	0	2.1	0	0	10	8	0.1	Wed Jul 13 02:26:12 Eastern Daylight Time 2005
build02.isis	Win32-vs60-shared-debug	0	0	0	0	2	0	0	10	8	0.1	Wed Jul 13 04:05:10 Eastern Daylight Time 2005
build02.isis	Win32-vs60-shared-release	0	0	0	0	2	0	0	10	8	0.1	Wed Jul 13 03:42:13 Eastern Daylight Time 2005
build02.isis	Win32-vs60-VTK4.4-debug	0	0	0	0	2.3	0	0	10	8	0.1	Wed Jul 13 01:15:13 Eastern Daylight Time 2005
build02.isis	Win32-vs60-VTK4.4-release	0	0	0	0	3	0	0	10	8	0.2	Wed Jul 13 01:02:12 Eastern Daylight Time 2005
asimov.caddlab.unc	WinXP-Cygwin-gcc3.4	0	0	0	0	0.8	0	0	10	8	0	Wed Jul 13 03:23:25 EST 2005

Fig 3. Nightly dashboard for multi-platform quality control.

develop a cross-platform toolkit without too much additional effort.

IGSTK has official and interim release cycles. The official releases are generally planned once a year. Official releases contain completed major functionalities of the toolkit such as new components. In between official releases, the team aims for interim releases approximately 2 or 3 months. Interim releases typically include new features for some components. Release information is posted on the IGSTK Wiki and the website (<http://www.igstk.org>).

Automated Testing

Incremental development relies on a continuous and stable software code base. Testing is critical to maintain the quality of the software. Incremental development can benefit greatly from continuous and automated testing. Automated testing provides instant feedback on the impact of new additions to the code base or bug fixes on the rest of the toolkit. Because IGSTK is a cross-platform toolkit, it is tested on various combinations of hardware, operating systems, and compilers, and the results are reported back to the developers. This is made possible by using the combination of CTest and the Dart system. CTest is one of the components of CMake, and it is intended to orchestrate the configuration, building, and testing of the software by gathering and submitting the results of these processes to a Dart server.

Dart is an open source infrastructure tool designed for software quality control in the context of a geographically distributed development team. In the Dart system, the software that is being tested is run on multiple combinations of hardware, operating systems, and compilers, and the results are submitted to a central server, where they are made available for review and feedback in a publicly accessible web page. In addition to compilation and build results, code coverage, unit test, and dynamic analysis results are posted on the Dart dashboard. This mechanism ensures a continued quality control of the software during the development stage. The dashboard accepts nightly, experimental, and continuous build results. Every night at a specified time, the entire IGSTK toolkit is built on multiple machines, and all the tests are run, and the results are posted on the dashboard.

Figure 3 shows a screenshot of a nightly IGSTK dashboard. During the day, if new changes are committed to the repository, continuous builds are submitted automatically to the dashboard. In this way, changes are immediately tested without waiting for the nightly build, and the developer can easily trace problems that the new changes may have caused in the rest of the toolkit. Experimental builds are used to test locally modified versions of the toolkit. This provides the developer with feedback about the impact of the local change on the rest of the toolkit before committing it to the repository.

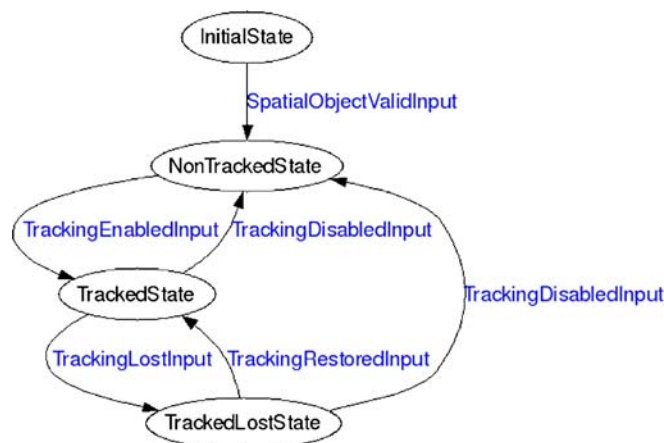


Fig 4. State machine for IGSTK tracker component showing the four states in black and the transitions in blue.

Communication and Documentation

Communication is essential for the success of a collaborative project, particularly for a geographically distributed development team. The IGSTK software process was designed to facilitate effective communication among developers and project leads. Biweekly teleconferences, idea sharing using Wiki pages, and mailing lists are powerful and effective tools for communication. Technical topics are discussed in great detail regularly during the teleconferences. Furthermore, the dashboard is reviewed at each teleconference to maintain the quality of the software.

Documentation is essential for the efficient and continued use of a toolkit. IGSTK follows the literate programming philosophy. Literate programming encourages developers to include human-readable documentation in the source code. IGSTK uses the Doxygen tool for automated document generation from the source code. Doxygen employs a simple mark up language that is embedded as comment statements in the source code. This mechanism has two main benefits. First, contrary to traditional software development approaches, developers will not have to spend time after code development writing documentation. Instead developers type the documentation as they continue implementing the code while the ideas are still fresh and while they are in the mindset of the code logic. In this way, the documentation will be ready when code development is finished. Secondly, when developers modify the code to add a new feature or fix a bug, they are required to update the markup comments accordingly so that the documentation will stay current with the code. In

IGSTK, the document generation process is also integrated with the nightly build system. Every night, the documentation is generated and made accessible from the dashboard. Hence, users always have access to the latest documentation.

To summarize the software process, here are the ten best practices adopted by the IGSTK team⁶:

- 1) Recognize that people are the most important mechanism available for ensuring high quality software
- 2) Facilitate constant communication among developers
- 3) Produce iterative releases
- 4) Manage source code from a quality perspective
- 5) Focus on 100% code and path coverage at the component level
- 6) Emphasize continuous builds and testing
- 7) Support the development process with robust tools
- 8) Manage requirements iteratively in lockstep with code management
- 9) Focus on meeting exactly the current set of requirements, and
- 10) Evolve the development process.

IGSTK ARCHITECTURE

IGSTK supports development of image-guided surgery applications that are classical examples of safety-critical applications. As a mechanism for preventing patient's harm, the architecture is based on the concept of safety-by-design. In particular, the IGSTK team followed a component-based

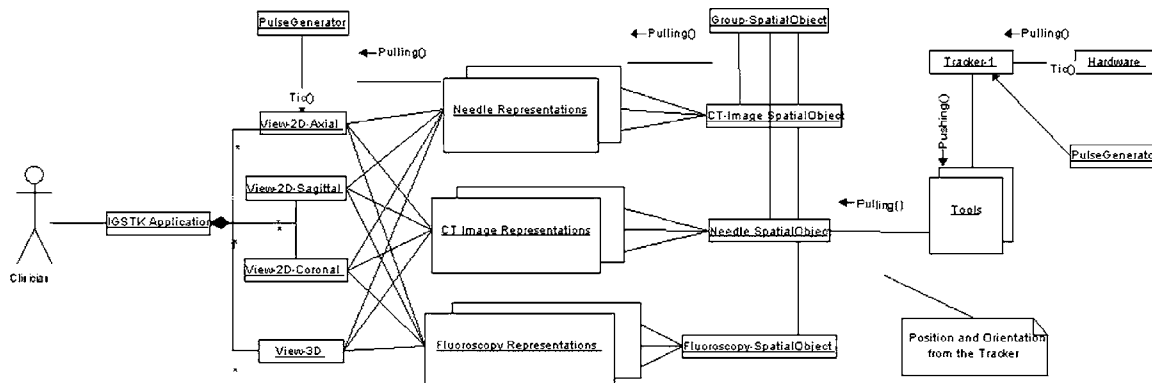


Fig 5. IGSTK component architecture.

architecture⁷ and used state machine⁸ software design methodologies. Every IGSTK component has a well-defined set of features that are governed by state machines. The state machine ensures that the component is always in a valid state and all state transitions are valid and meaningful. Figure 4 shows the state machine implementation for the tracker component (the IGSTK components will be described later in this section).

In a component-based architecture, the main capabilities are broken down into functional components with well-defined interfaces for inter-component communication. This type of architecture has several benefits when developing a reliable and robust toolkit. Breaking down the complex functionalities into smaller pieces makes implementation manageable and makes it possible to enforce higher standards of quality control. It is much easier to thoroughly test small components with well-defined interfaces than to test medium or large size components with myriads of features and convoluted interfaces. Consequently, complexity and implementation details are encapsulated in the component level and hidden from the application developer or user. This encapsulation allows IGSTK to better manage the inherent complexity of an image-guided surgery system. Furthermore, testing is easier at the component level compared to traditional procedural software thereby increasing the quality of the software. Application developers can also use some of the components independently in their application

without the need to integrate the full toolkit. This should increase the adoption of the software and subsequently benefit the user community. Lastly, a component-based architecture is suitable for structured toolkit extension. This will encourage users to extend the toolkit by adding new components and by contributing them back to the community.

A state machine is defined by a set of states, a set of inputs, and a set of directed transitions from state to state. Each IGSTK component is subjected to state machine control. Incorporation of state machines has enhanced the reliability of the toolkit for the following reasons. State machines can ensure that the components have deterministic behavior at all times and are always in a known and error-free state. Formal validation⁹ of the software can be undertaken because inputs, states, and transitions are well defined and are finite. This framework is suitable for automated testing. Interaction between the user and other applications can be explicitly defined using state machines reducing the possibility of design and implementation flows in application development. In summary, state machines ensure safety and reliability, cleaner design, application programming interface (API) simplicity, consistent integration pattern, and allow quality control. State machines can also prevent the misuse of components and help manage complexity, traceability, and testing.

IGSTK components are implemented using the C++ programming language. The component implementations are mostly based on ITK and

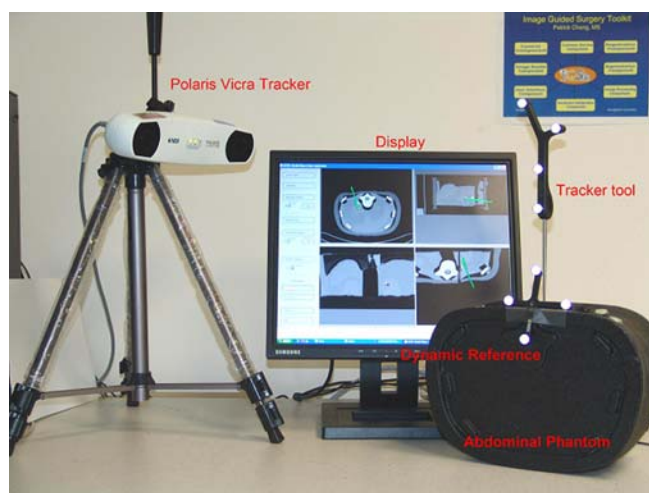


Fig 6. Needle biopsy application system setup.

VTK classes subjected to a strict state machine control. IGSTK components however do not expose ITK or VTK classes in their public interface. This exposure is avoided to increase the level of safety of the components. Interactions with the ITK and VTK classes are done only inside the IGSTK components and only under the supervision of the state machine.

The IGSTK architecture is shown in Figure 5. The main components in IGSTK are presented in the following list, and a short description of each component is given:

- View (Display)
- Spatial objects (geometric representation)
- Spatial object representation (visual representation)
- Trackers
- Readers

View (Display)

Viewers display the graphical representations of the renderings of surgical scenes. Surgeons perform their task by visualizing the information provided in the viewers. Furthermore, the view components serve as a link between the graphical user interface library and the rest of the IGSTK toolkit.

Spatial Objects (Geometrical Representation)

Spatial objects define a common structure for geometrical objects in IGSTK. The spatial objects hold the shapes and physical locations of objects in the surgical environment. IGSTK spatial objects encapsulate ITK spatial objects in a restrictive API. Spatial objects provided by IGSTK include objects such as axes, boxes, cones, cylinders, images, ellipsoids, meshes, tubes, and vascular networks.

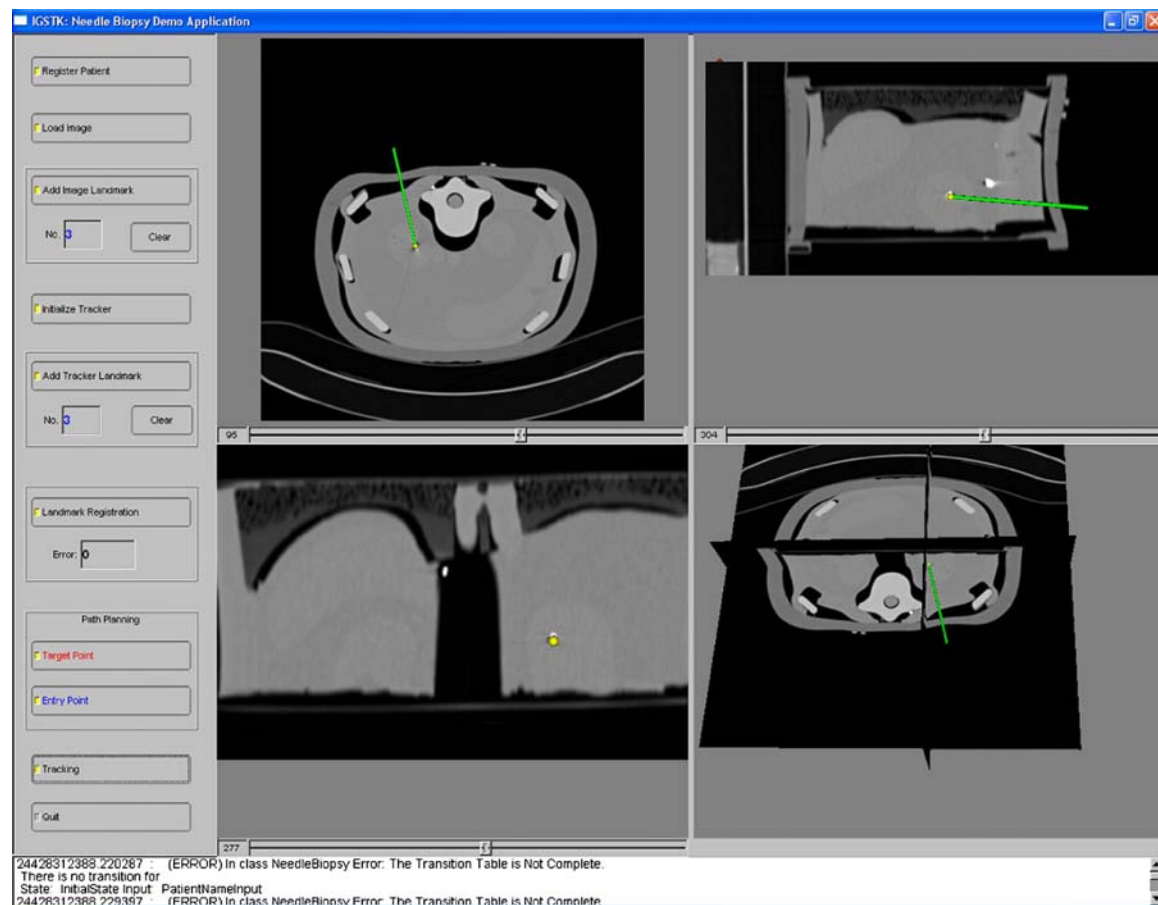


Fig 7. Graphical user interface for the needle biopsy application.

Spatial Object Representation (Visual Representation)

Spatial object representations characterize the graphical representations of the spatial object. The graphical representations dictate how an object should be displayed on the screen. This will include specifying color, opacity, and other rendering properties.

Trackers

The tracker component handles the communication between tracking tools and tracking devices to get position, orientation, and other relevant information from surgical instruments present in the scene. The tracking component encapsulates the tracking tool, tracking device, and all static and dynamic information associated with tracking.

Readers

Readers bring data into the scene generation and representation process. The most important readers in IGSTK are the Digital Imaging and Communications in Medicine (DICOM) image reader classes. These classes are used to read preoperative and intraoperative scans for surgical planning and guidance. Validity check logic is implemented in these classes to avoid incorrect file reads and 3D

volume generation. Additional readers are available also for loading mesh and calibration data.

In addition to the above main components, IGSTK has a collection of infrastructure and service classes. The infrastructure classes include state machines, events, pulse generators, and real-time clock generator classes. Service classes include loggers, registration, and calibration classes. Loggers are useful for post-analysis of surgical procedures and recovery from a failure. Integrating loggers into applications streamlines and expedites the application development process and also provides a suitable framework for verification and validation.

Another service class in IGSTK is the registration class. This class computes the spatial transformation between the patient and the coordinate systems of the multiple image data sets that may be present in the scene, including preoperative and intraoperative images. Finally, a calibration class is available to measure the most important point of a surgical instrument relative to the position of the tracked element on the tool attached to the instrument.

Putting It All Together

To demonstrate how the components can be integrated to develop an application, we will discuss an example image-guided needle biopsy application developed using IGSTK.



Fig 8. Robot assisted needle placement phantom study.

Needle biopsy is a medical procedure intended to take a sample of tissue from a lump or tumor or other abnormal growth in the body with the purpose of performing a pathological analysis. An interventional radiologist will insert a needle into the tumor and take a tissue sample. This is a common procedure for cancer diagnosis. It is critical to ensure that the needle reaches the target that has been identified from the images.

In this application, the patient is positioned on the CT table, a CT image is acquired, and the location of the pathological tissue is identified on the images. A landmark-based registration technique is then used for registering the image coordinate system to the patient coordinate system. During the biopsy procedure, a computer graphics-generated representation of the surgical scene is presented in the display and is updated with the current position and orientation of the needle as they are

continuously reported by a tracker. The workflow of this application is outlined below.

- 1) Record patient demographic information
- 2) Acquire and transfer CT image to the image-guided system
- 3) Identify landmark points in the image using the mouse. A minimum of three noncollinear landmark points are required.
- 4) Initialize the tracking device
- 5) Identify the corresponding landmarks in the physical body using the tracker pointing device
- 6) Perform registration to compute the transformation from patient to preoperative image
- 7) Identify entry point and target position for needle path planning
- 8) Start tracking.

When tracking is started, an updated position of the needle is displayed and overlaid on the CT

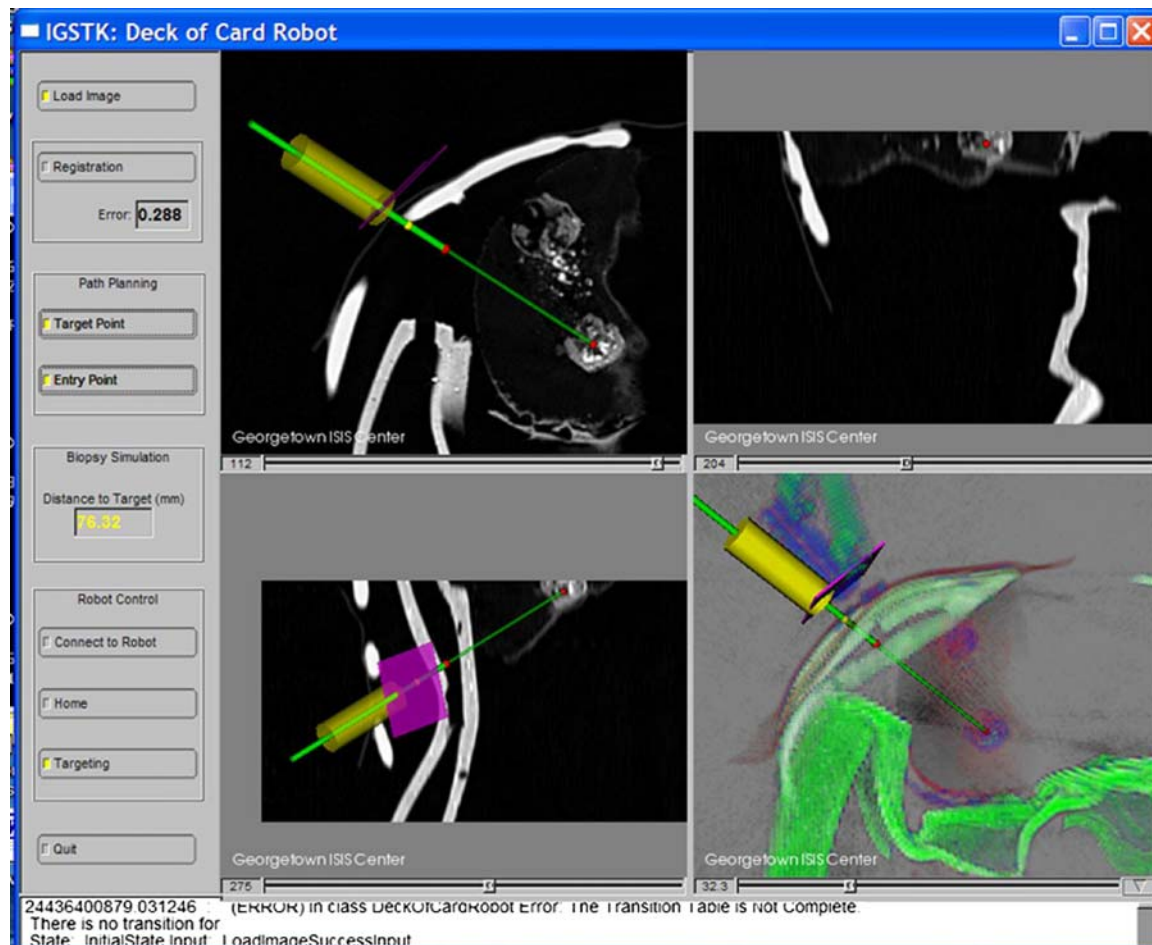


Fig 9. Graphical user interface for the robot assisted needle placement application.

image. The radiologist can then manipulate the needle, watching the virtual image, until the needle reaches the target. A confirming CT image can then be acquired.

For this example application, a Polaris Vicra optical tracker (Northern Digital, Ontario, Canada) was used. Testing was performed using an abdominal phantom (CIRS Model 57, Norfolk, VA). The application set up is shown in Figure 6. Figure 7 shows the user interface, which consists of a control panel and four standardized views: axial, sagittal, coronal, and a 3D view. The four view windows show CT images of the abdominal phantom with the overlay of the biopsy needle path. The green cylinder represents the needle as tracked by the Polaris Vicra Tracker. The four views automatically re-slice and update the images to show the needle tip position as it moves in the patient's anatomy.

BUILDING AN IGSTK COMMUNITY

The continued success and viability of an open source toolkit depends on strong user community support. High quality design and architectural robustness are significant factors that drive the adoption of open source software. However, for long-term success and continuous evolution of the software, contributions from the user community are equally vital. Beyond the first few years of development supported by funding agencies, the lifetime of the toolkit depends on dedicated users and volunteers who care about the toolkit. Hence, as part of the toolkit development effort, toolkit creators should treat building and supporting the user community as a very important task. Without a committed user community, any open source software fades away after just few years of existence. With this understanding, the IGSTK team has taken several key steps to build a strong IGSTK community.

Complete documentation encourages users to evaluate the toolkit and contribute modifications and bug fixes. Automated documentation generation techniques simplify this task in IGSTK. Users have access to the latest API documentation from the IGSTK website and from the dashboard. Furthermore, to provide a detailed description of the toolkit and technical explanation of the components, the IGSTK team has written and

published a book.¹⁰ The book is available in a PDF format for free download at the IGSTK website (<http://www.igstk.org>).

A users' mailing list has also been created. Questions posted in this mailing list are promptly answered by the developers of the toolkit. Furthermore, users post bug reports, make feature requests, and contribute suggestions on how to improve the toolkit. These suggestions are seriously studied by the development team, documented in the bug tracker, and considered for implementation as time and resources permit.

Demonstrations of the toolkit is another key dissemination effort undertaken by the group. The needle biopsy application described above was demonstrated at the SPIE Medical Imaging Conference in 2006 and 2007 at San Diego, CA. Similarly, at the 2007 Society of Medical Innovation and Technology Conference, a robotically assisted needle placement application was demonstrated. The application guides the insertion of a needle using the robot. Figures 8 and 9 show the robot set up and a screenshot of the graphical user interface. The application demonstrations have helped to introduce the toolkit to the medical research community. Related to this effort, tutorial sessions on IGSTK have been offered at the SPIE Medical Imaging conference as part of the medical image analysis course using open source software.

What users are allowed to do with any open source software is defined by the copyright holder in the specific terms of the distribution license. For this reason, the selection of an appropriate license for the toolkit is also essential in building a strong user community. The copyright of IGSTK is held by the Insight Software Consortium (<http://www.insightsoftwareconsortium.org>). IGSTK is released under a Berkeley Software Distribution-like license, which allows the use of the software free of charge for academic and commercial applications. It also allows users to redistribute the software, modify it, and distribute the modifications without requiring permissions from the copyright holders. An example of the IGSTK commitment for building a strong community is the new collaboration that was recently established with the SINTEF Health Research Center at Norway. The center conducts cutting edge research on developing advanced navigation and visualization technologies for image-guided surgery.¹¹ The

group is now actively involved in the development of new components of the IGSTK toolkit.

CONCLUSION

Image-guided interventions are increasingly becoming the medical procedure of choice among patients and clinicians. They cause less trauma to the body and patients recover more rapidly from these procedures. Software is a critical component of such systems. Developing reliable software for such safety-critical applications is a challenging task. Oftentimes, research institutions invest large amounts of resources to build basic software infrastructures to develop these applications. With the availability of the IGSTK toolkit that contains all the components needed to build image-guided applications, researchers will be able to focus their resource on the main scientific problems. IGSTK is designed based on software principles intended to ensure reliability and patient safety in medical applications. The automated build and test management system deployed in IGSTK makes it easy to accept and integrate contributions from the user community while maintaining the high software quality standards established in the project. This is essential for the continued success and viability of open source software.

ACKNOWLEDGMENTS

This project is a collaboration between Georgetown University, Kitware, Arizona State University, and Atamai. All of the software is freely available for download and can be used in research or commercial applications. More information can be found on the website at <http://www.igstk.org>.

This work was funded by NIBIB/NIH grant R01 EB007195 under project officer John Haller. Additional support was provided by US Army grant W81XWH-04-1-007, administered by the Telemedicine and Advanced Technology Research Center (TATRC), Fort Detrick, MD. The content of this manuscript does not necessarily reflect the position or policy of the US Government. We thank our other collaborators throughout the project, including Rick Avila and Will Schroeder of Kitware; Roland Stenzel of Georgetown University; Geir Arne Tangen, Ole

Vegard Solberg, Arild Wollf, Torleif Sandnes of SINTEF Health Research, Medical Technology (and the National Centre for 3D Ultrasound in Surgery), Trondheim, Norway; Ivo Wolf of the German Cancer Research Center, Heidelberg; Peter Kazantzides and Anton Deguet of Johns Hopkins University; Nobuhiko Hata of Brigham and Women's Hospital; Sohan Ranjan of GE Research; Mihai Mocanu of the University of Craiova; and Matt McAuliffe and Terry Yoo of the NIH.

REFERENCES

1. Schroeder W, Martin K, Lorensen B: The Visualization Toolkit: An object-oriented approach to computer graphics, 4th edition. Clifton Park, NY: Kitware Inc., 2006
2. Ibanez L, Schroeder W: The ITK Software Guide, 2nd edition. Clifton Park, NY: Kitware Inc., 2005
3. Forrester Consulting: Opensource software's expanding role in the enterprise, A Forrester Consulting study commissioned by Unisys Corporation, Forrester Research Inc., 2007
4. Hajnal JV, Hill D, Hawkes DJ: Medical Image Registration. Boca Raton, FL: CRC Press LLC, 2001
5. Martin K, Hoffman B: Mastering CMake: A Cross-Platform Build System, 3rd ed. Clifton Park, NY: Kitware Inc., 2006
6. Gary K, Blake MB, Ibanez L, Gobbi D, Aylward S, Cleary K: IGSTK: An open source software platform for image-guided surgery. *IEEE Computer* 39(4):46–53, 2006
7. Blake MB, Cleary K, Kim HS, Ranjan S, Gary K, Jomier J, Aylward S, Ibanez L: Component-Based Design and Development for Robust Medical Applications, High Confidence Medical Device Software and Systems (HCMDSS) Workshop, 2005
8. Ibanez L, Jomier J, Gobbi D, Avila R, Blake MB, Kim H-S, Gary K, Aylward S, Cleary K, IGSTK: A State machine architecture for an open source software toolkit for image-guided surgery applications, *Insight Journal—MICCAI Open-Source Workshop*, 2005
9. Gary K, Kokoori S, David B, Otoom M, Blake MB, Cleary K: An Architecture Validation Toolset for Ensuring Patient Safety in an Open Source Software Toolkit for Image-Guided Surgery Applications, *Insight Journal—MICCAI Open-Source Workshop*, 2006
10. Cleary K, IGSTK Team: IGSTK: An Open Source C++ Software Library. Gaithersburg, MD: Signature Book Printing, 2007
11. Rasmussen IA, Lindseth F, Rygh OM, Berntsen EM, Selbekk T, Xu J, Nagelhus Hernes TA, Harg E, Haberg A, Unsgaard G: Functional neuronavigation combined with intra-operative 3D ultrasound: Initial experiences during surgical resections close to eloquent brain areas and future directions in automatic brain shift compensation of preoperative data. *Acta Neurochir (Wien)*, 149(4):365–378, 2007

7.8 Lin 2008: Phantom evaluation of an image-guided ...

Reprint begins on the next page and is seven pages.

Phantom Evaluation of an Image-Guided Navigation System based on Electromagnetic Tracking and Open Source Software

Ralph Lin^{a*}, Peng Cheng^a, David Lindisch^a, Filip Banovac^a, Justin Lee^b, Kevin Cleary^a

^aImaging Science and Information Systems Center, Department of Radiology, Georgetown University, Washington DC

^bGeorgetown University Hospital, Washington DC

ABSTRACT

We have developed an image-guided navigation system using electromagnetically-tracked tools, with potential applications for abdominal procedures such as biopsies, radiofrequency ablations, and radioactive seed placements. We present the results of two phantom studies using our navigation system in a clinical environment. In the first study, a physician and medical resident performed a total of 18 targeting passes in the abdomen of an anthropomorphic phantom based solely upon image guidance. The distance between the target and needle tip location was measured based on confirmatory scans which gave an average of 3.56 mm. In the second study, three foam nodules were placed at different depths in a gelatin phantom. Ten targeting passes were attempted in each of the three depths. Final distances between the target and needle tip were measured which gave an average of 3.00 mm. In addition to these targeting studies, we discuss our refinement to the standard four-quadrant image-guided navigation user interface, based on clinician preferences. We believe these refinements increase the usability of our system while decreasing targeting error.

Keywords: abdominal procedures, image-guided therapy, validation

1. INTRODUCTION AND BACKGROUND

Image guidance has become increasingly important in minimally invasive procedures, in which physicians cannot directly visualize the underlying anatomy. Previous image-guided systems have relied upon optical tracking for real-time tool location information. These optical systems use a series of cameras to triangulate on optical reflectors placed on a tool and provide high spatial accuracy at the cost of requiring line-of-sight between the cameras and reflectors to be maintained. Electromagnetic tracking systems, on the other hand, rely on electromagnetic fields generated by a field generator which are received by coils of wire located inside the tool. Recent developments in electromagnetic tracking technologies, particularly the miniaturization of sensor coils, have allowed researchers to create image-guided systems that can track instruments inside the body.

Despite the benefits of electromagnetically-tracked systems, they have not been widely adopted for use in image-guided applications. This may be due to their susceptibility to electromagnetic interference caused by ferromagnetic substances placed within the measurement field. Several groups have quantified these errors in laboratory and clinical environments^{1,2}. However, current versions of these electromagnetic systems are more resistant to small amounts of metal in the operative environment. In addition, recent systems such as the 3D Guidance Flat Transmitter from Ascension Technology (Burlington, VT) have also been developed for operation in metal filled environments such as an operating room.

Our research group has developed an image-guided system based upon an open source software toolkit³ and the Aurora electromagnetic tracking system (Northern Digital Incorporated, Waterloo, Ontario, Canada). This system provides real-time tool location information overlaid on a pre-procedural CT, MRI, or other 3D volumes. The paper presents the results of two phantom studies using this system within a clinical environment.

* Current affiliation: Department of Bioengineering, University of Washington, Seattle, WA
Email: ralphlin@u.washington.edu

2. MATERIALS AND METHODS

The first study was designed to investigate targeting accuracy in an abdominal phantom as performed by an interventional radiologist and a medical resident. The second study was designed to determine the performance of our image-guided system using targets placed at different surface depths to simulate liver tumors located at different distances from the skin. Both studies were performed at the Georgetown University Hospital in the angiography suite equipped with a Siemens Axiom dFA angiography system with a flat-panel detector.

In the first study, we used a human torso phantom built by our colleagues at Johns Hopkins University made from silicone (TC-5005, BJB Enterprises Inc., Tustin, CA) and incorporating a synthetic skeleton⁴. We placed a foam liver inside the abdominal cavity with several spherical (approximately 3 cm in diameter) contrast-enhanced nodules to simulate tumors (see Figures 1 and 2). To gain access to the foam liver with our electromagnetically-tracked tools, we cut a 2 cm x 4 cm rectangular opening in the chest of the torso phantom and filled it with gelatin (Knox Gelatine, Kraft Foods, Northfield, IL).

After an initial rotational angiography acquisition and 3D reconstruction (DynaCT), we performed landmark-based registration using adhesive skin fiducials (Multi-Modality Markers, IZI Medical Products, Baltimore, MD) placed on the surface of the torso phantom. Care was taken to not disturb the field generator orientation and placement in relationship to the torso after initial set up. The average RMS registration error was 0.82 mm.

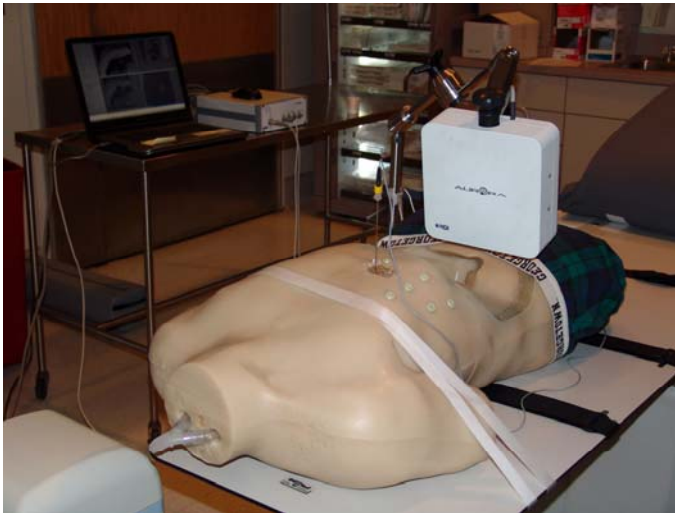


Figure 1: Anthropomorphic phantom and experimental set-up (phantom constructed by URobotics Laboratory, Johns Hopkins University)

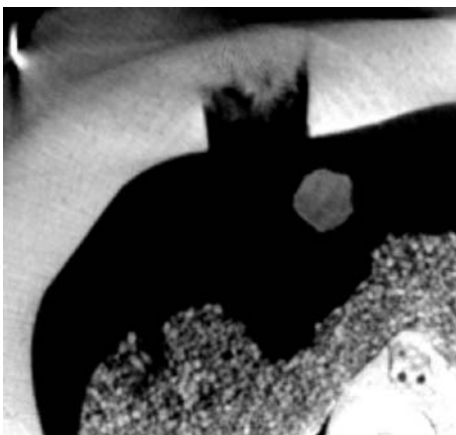


Figure 2: Axial DynaCT slice of anthropomorphic phantom with simulated tumor

The physician or resident then chose a skin entry location and target location in the phantom by clicking points on the DynaCT volume displayed on our image-guidance workstation. Using electromagnetically-tracked needles the physician or resident attempted to place the needle at the target location based solely upon image guidance. After needle placement, another 3D acquisition was obtained. This volume was used to measure the final needle location in relation to the selected target point. Nine passes each were performed by an interventional radiologist and medical resident (for a total of 18 passes) within the interventional radiology suite at Georgetown University Hospital.

In the second study, we attempted to evaluate the effect of tumor depth on accuracy for our image-guided system. We created several contrast-enhanced foam nodules (Flexfoam, Smooth-On, Easton, PA) to simulate liver tumors and suspended them in a gelatin-filled container (Knox Gelatine, Kraft Foods, Northfield, IL, see Figure 3). Three foam nodules were placed at three depths in the gelatin (approximately 3 cm, 7.5 cm, and 11 cm from the surface). As in the first study, we took an initial 3D acquisition and used landmark-based registration using adhesive fiducials (see Figure 4). The average RMS registration error was 0.76 mm. We then performed 10 passes in each tumor and acquired a DynaCT volume to measure distance from target to needle tip location. Unfortunately, we were not able to collect data from the shallow tumor due to the tendency of the needle to move between final needle placement and confirmatory scan. The gelatin was not stiff enough to hold the needle at that depth.



Figure 3: Picture of contrast-enhanced tumors and experimental set up with tumors in gelatin phantom

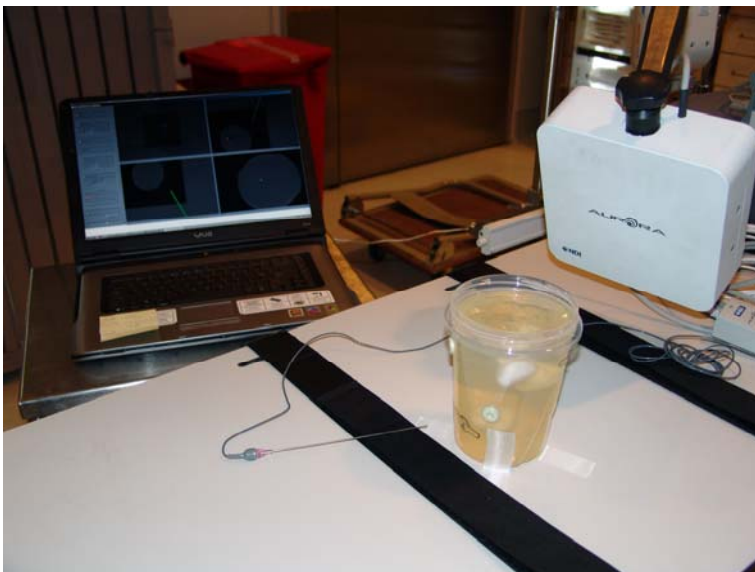


Figure 4: Experimental set up with tumors in gelatin phantom for study 2

In both studies, we used a software application based on an open source image-guided surgery toolkit (IGSTK) developed by Georgetown University and partners³. Instead of using the standard four-quadrant view, we worked closely with several radiologists to create new views to facilitate higher targeting accuracy and greater ease of use (Figure 5). A patient-centric perspective was chosen to closely mimic the clinical perspective. In addition to an axial view, we resliced the dataset to create an off-axial and off-sagittal viewing plane centered on the patient's skin surface while containing the electromagnetically-tracked needle (Figure 6). These planes followed the real-time position of the tracked needle position allowing the user to make more realistic adjustments to the needle trajectory. Finally, we created a view (bottom right-hand view in Figure 5) that is fixed to be perpendicular to the planned path. This view included graphical indicators for both the needle tip and needle hub position and was found to be the most useful by both the clinical and research staff for needle placement in the target. Each needle targeting pass in the studies was started by placing the needle tip (green ball) in the center of the target (red ball). Once the needle was oriented such that the needle hub (yellow ball) was co-located with the red and green ball, the needle was advanced until the desired depth was reached. All views were generated taking into account the position of the screen relative to the physician and patient--all movements on the screen matched the actual movement of the physician.

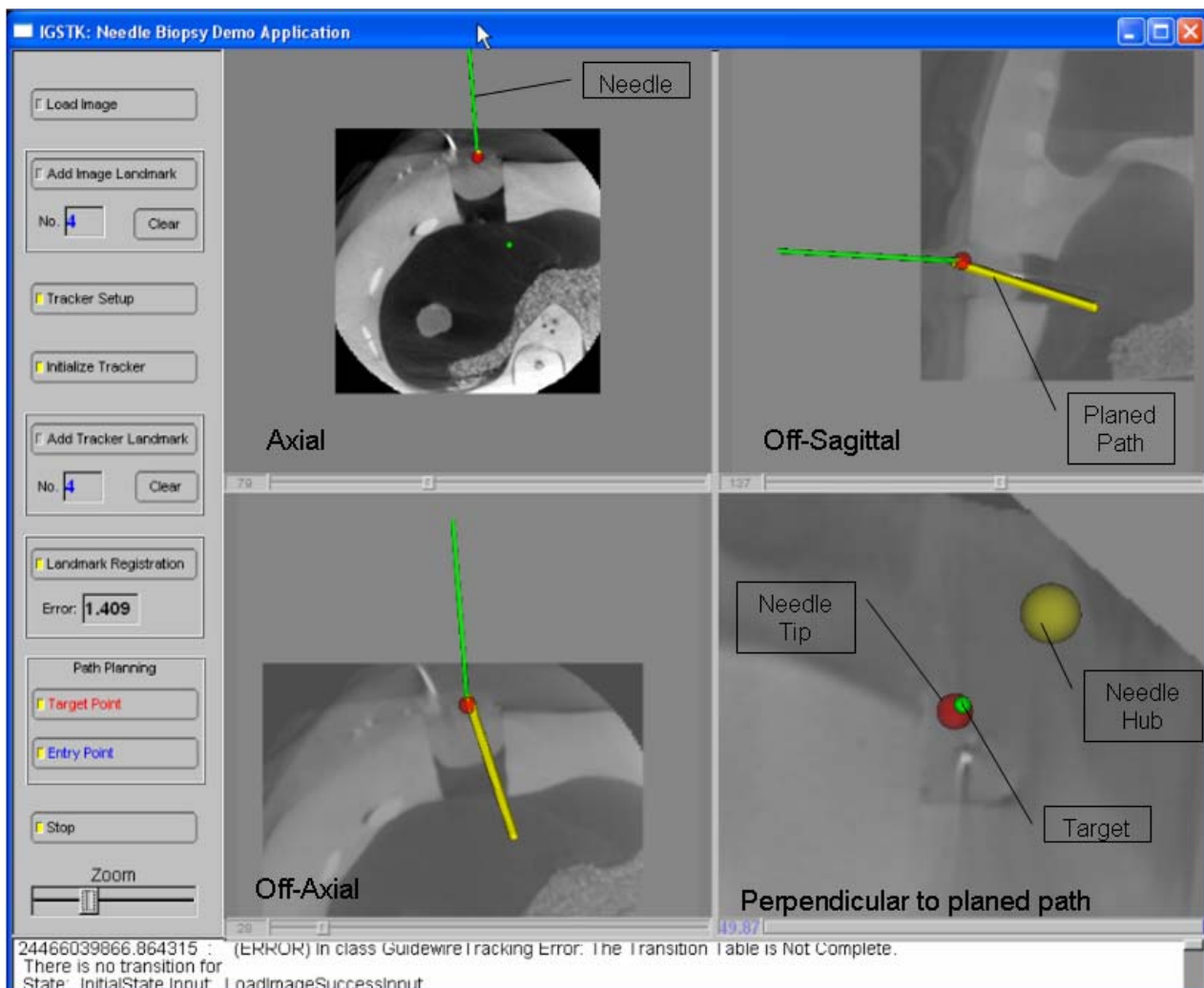


Figure 5. Screenshot of user interface showing axial, off-sagittal, off-axial, and targeting windows.

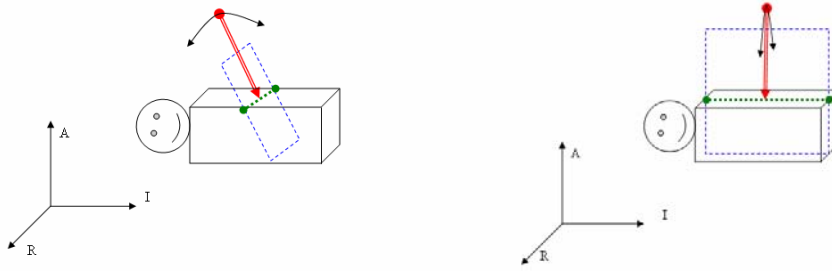


Figure 6. Diagrams of off-axial and off-sagittal views. Red lines denote needle. Blue dashed lines indicate viewing plane. Green dashed lines indicate axis of rotation.

3. RESULTS

For each pass in study 1, we calculated the reported RMS error as displayed by the image guidance workstation after each needle placement in the target and the actual RMS error between needle tip and target position in the confirmatory dataset. The reported error was calculated in the electromagnetic coordinate space, while the actual error was calculated by manually segmenting the needle tip position in each confirmatory scan and comparing it to the selected target position in image coordinate space. The average over all passes for actual error between final needle tip position and target was 3.56 mm (SD 1.93 mm) and the average reported error was 2.15 mm (SD 0.78 mm). All passes were performed by the clinical authors (FB, JL) in the interventional suite at Georgetown University Hospital.

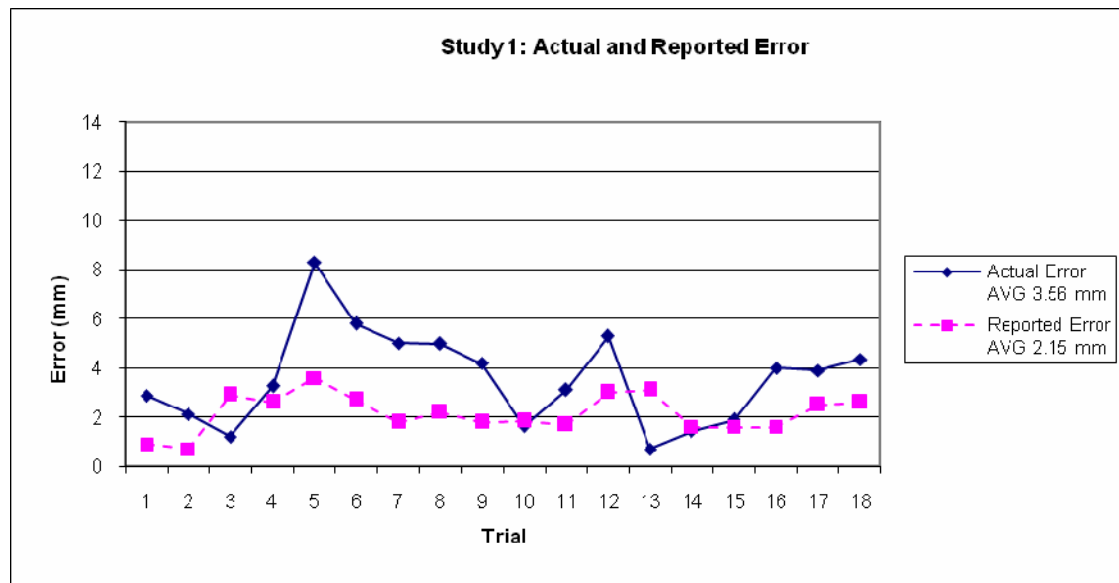


Figure 7: Errors for Study 1

All passes in the second study were performed in the interventional suite at Georgetown University Hospital. We surprisingly measured a smaller needle tip placement error for the deep target compared to middle target and more consistent accuracy (denoted by the smaller standard deviation) when compared to study 1.

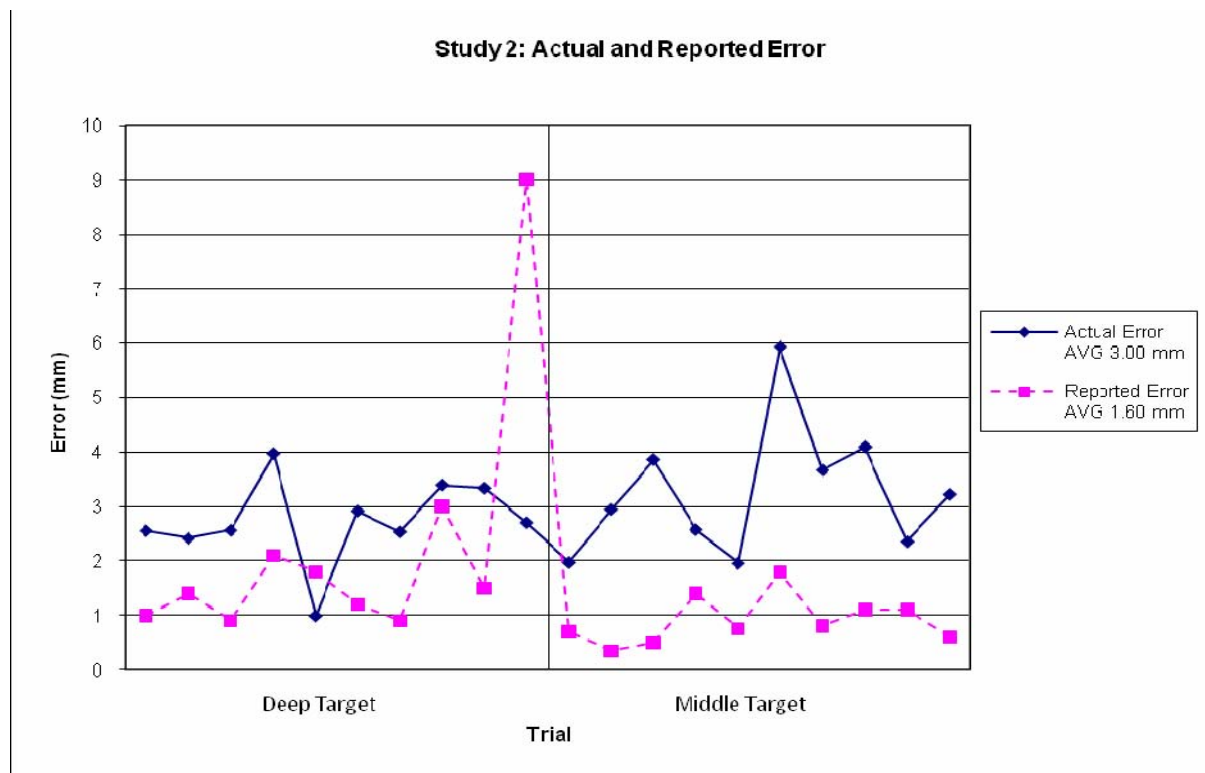


Figure 8: Errors for study 2

Results for Study 2*	
Average RMS error over 20 passes	3.00 mm (SD 1.03 mm)
Average RMS error for deep target (10 passes)	2.74 mm (SD 0.79 mm)
Average RMS error for middle target (10 passes)	3.26 mm (SD 1.21 mm)

* Shallow target was not able to be targeted due to the instability of the gelatin and the tendency of the needle to drift between placement and confirmatory scan

4. DISCUSSION

We present a refined image-guided navigation system based upon an open source framework and evaluate the accuracy of the system in two phantom studies. Previous studies^{1,2} have shown electromagnetic interference in the hospital environments to be approximately 2-3 mm, at best, and we estimate human error in needle placement to be 1-2 mm, at best. The results of our two phantom studies show an overall accuracy of 3.26 mm which include these accumulated errors of electromagnetic interference, registration error, and human error in placement of the needle.

Although there is a surprising tendency in the second study showing increased error in the middle target, located 7.5 cm from the surface, compared to the deep target, located 11 cm from the surface, we still see an overall RMS target error of 3.00 mm. We hypothesize that the increase in error for the middle target was due to the needle shift between placement and confirmatory scan. Further examinations with a stiffer substrate may be able to explain this trend.

5. CONCLUSION

We have successfully developed an image-guided navigation system based upon an open source software framework. By using electromagnetic tracking, we are able to overlay real-time instrument locations on pre-procedural DynaCT volumes thereby guiding physicians to precisely place the needle in desired locations. Surveys among the clinical staff at

Georgetown University Hospital show a greater ease of use with the refined four-quadrant display developed for these studies as compared to previous iterations of the software toolkit.

Our studies show, over all 38 targeting passes, an average RMS distance from actual needle tip location to planned needle tip location of 3.26 mm. Considering this figure represents all accumulated error from the environment and software, we believe this could be a promising platform for increasing the effectiveness of existing therapies and enabling new therapies currently limited by the spatial accuracy of non-image-guided procedures. We have already begun to investigate using this platform for radioactive seed placement in brachytherapy, radiofrequency ablation, vertebroplasty and biopsy while also investigating real-time registration to account for movement between the time of the pre-procedural scan and the procedure itself.

Use of an image-guided planning system such as the one described above would reduce overall radiation exposure to the patient and physician, especially compared to the current advance-and-check technique of percutaneous access to the thoraco-abdominal cavity. These systems could be particularly useful in treating cancers using radiofrequency ablations requiring multiple ablations to completely ablate the tumor⁵. Combined with computerized path planning based on pre-procedural imaging, image guidance could potentially improve the ability to treat cancer in these situations by more precisely locating ablated regions and guiding physicians towards untreated tumor tissue.

ACKNOWLEDGEMENTS

This work was funded by U.S. Army grant W81XWH-04-1-0078 and administered by the Telemedicine and Advanced Technology Research Center (TATRC), Fort Detrick, Maryland, USA. The content of this manuscript does not necessarily reflect the position or policy of the U.S. Government.

REFERENCES

- [1] Shen E., Shechter G., Kruecker J. and Stanton D. "Quantification of AC electromagnetic tracking system accuracy in a CT scanner environment." Proc. SPIE 6509, DOI: 10.1117/12.710836 (2007).
- [2] Nafis C., Jensen V., Beauregard L. and Anderson P. "Method for estimating dynamic EM tracking accuracy of surgical navigation tools." Proc. SPIE 6141, DOI: 10.1117/12.653448 (2006).
- [3] Gary K., Ibanez L., Aylward S., Gobbi D., Blake M.B. and Cleary K., "IGSTK: An open source software toolkit for image guided surgery," IEEE Computer, 39(4), 46-53 (2006).
- [4] Lin R., Wilson E., Tang J., Stoianovici D. and Cleary K., "A computer-controlled pump and realistic anthropomorphic respiratory phantom for validating image-guided systems," Proc. SPIE 6509, DOI: 10.1117/12.712226 (2007).
- [5] Zhang H., Banovac F., Munuo S., Campos-Nanez E., Abeledo H. and Cleary K., "Treatment planning and image guidance for radiofrequency ablation of liver tumors," Proc. SPIE 6509, DOI: 10.1117/12.711489 (2007).

7.9 Shah 2008: Robotically assisted needle driver: ...

Reprint begins on the next page and is seven pages.

Robotically assisted needle driver: evaluation of safety release, force profiles, and needle spin in a swine abdominal model

S. Shah · A. Kapoor · J. Ding · P. Guion ·
D. Petrisor · J. Karanian · W. F. Pritchard ·
D. Stoianovici · B. J. Wood · K. Cleary

Received: 10 January 2008 / Accepted: 25 April 2008
© CARS 2008

Abstract

Objective The objective of this study was to evaluate two features of a new rotating needle driver in a domestic swine model: (1) a quick release safety mechanism and (2) the impact of spinning the needle on the force profile.

Materials and methods The experiments were conducted in a multi-modality interventional suite. An initial CT scan was obtained to determine the location of the target, in the liver or lung. The robotic arm was positioned directly over the marked skin entry point. Control parameters were set to rotation speeds of 0, 90, or 180 rpm. The breakaway force magnitude was also preset to a predetermined force. The physician used the joystick to drive the needle towards the target while the system recorded needle insertion depth and forces.

The mention of commercial products, their source, or their use in connection with material reported herein is not to be construed as either an actual or implied endorsement of such products by the U.S. Food and Drug Administration, the Department of Health and Human Services or the Public Health Service.

S. Shah (✉) · A. Kapoor · P. Guion · B. J. Wood
National Institutes of Health Clinical Center,
Diagnostic Radiology Department,
Bethesda, MD, USA
e-mail: shahsap@cc.nih.gov

J. Ding · K. Cleary
Imaging Science and Information Systems (ISIS) Center,
Department of Radiology, Georgetown University,
Washington, DC, USA
e-mail: cleary@georgetown.edu

D. Petrisor · D. Stoianovici
URobotics Laboratory, Department of Urology,
Johns Hopkins Medicine, Baltimore, MD, USA

J. Karanian · W. F. Pritchard
Laboratory of Cardiovascular and Interventional Therapeutics,
FDA, Laurel, MD, USA

Results Sixteen insertions were completed (14 in liver and 2 in lung) and 12 released the needle upon the desired set force. The mean response time of the quick release mechanism was 202 ± 39 ms. Needle rotation resulted in reduced insertion force.

Conclusion The robot-assisted needle insertion system was shown to be functional in a multimodality imaging clinical environment on a swine model. The system has potential future applications in precision minimally invasive procedures including biopsy and radiofrequency ablation.

Keywords Robotics/instrumentation · Safety · Minimally invasive · Rotating needle driver

Introduction

Minimally invasive procedures have become standard medical practice in many settings due to numerous advantages such as decreased recovery time, cost, trauma, and complications in comparison to conventional surgery. The applications of these procedures range over a variety of specialties including but not limited to urology, cardiology, neurosurgery, orthopedics, radiation oncology, oncology, and interventional radiology. Many of these minimally invasive procedures rely upon accurate insertion of a needle to an anatomical target to deliver therapy or obtain tissue samples from a pre-determined specific location.

A few common examples of needle-based procedures include biopsy, radiofrequency ablation (RFA), and prostate brachytherapy. The outcome of minimally invasive procedures such as RFA depends on the size and location of the target lesion and the experience of the physician. For a complete zone of ablation, RFA requires the diameter of the ablation sphere to be 2 cm greater than the tumor to obtain a 1 cm margin [1]. Prostate brachytherapy is another needle-based

procedure that requires placement of radioactive seeds at pre-planned locations around the prostate. Typically about 100 radioactive seeds are placed to provide adequate coverage of the tumor site. Currently, needles or electrodes are manually inserted into a target by the physician, primarily under image guidance. This requires a significant amount of training, coordination, and 2D to 3D extrapolation. Procedures such as these also potentially expose the patient and physician to significant radiation. Inaccuracies in needle or electrode placement for these procedures and lack of navigation devices to aid placement may result in increased procedure time, morbidity, inaccurate diagnosis, or tumor recurrence [2].

In recent years, robot-assisted needle insertion has attracted attention because of its capabilities to provide assistance in minimally invasive procedures. Computers and robots have been used in combination with these procedures and have demonstrated enhanced performance under direct physician guidance simultaneous with human input as compared to the more conventional method of the physician alone, without robotic assistance [3]. Feasibility studies have been presented by Solomon et al. [4] to develop a tumor ablation treatment system that utilizes the Acubot robot system for accurate applicator placement tested in patients. A robotically assisted needle insertion system for prostate brachytherapy has also been tested in phantoms by Fichtinger et al. [5]. The system consists of a transrectal ultrasound (TRUS) and a spatially co-registered robot. A few other robotic systems such as iGuide [6,7], Innomotion [8], Pinpoint from Philips Healthcare Inc. [9], Hata's Semi-Active robot [10], compatible with CT and MRI, are under active development by various researchers as well (see reviews [11,12] for a more exhaustive list). These systems may provide a safer working environment for the physician by limiting the amount of radiation exposure. More importantly, they are capable of enhancing outcomes by improving repeatability and accuracy which could in turn help address standardization of surgeon skill variability.

Aside from accurate placement of the needle, a major safety concern is the risk of tissue laceration due to respiratory, organ, or patient movement when using a rigid robotic needle driver. When the needle is inserted into the body, patient movement due to breathing or shift may cause laceration or trauma. Respiration can cause tissue movement of 1–20 mm or more in the area of interest [13], greatly hampering accuracy. Currently physicians try to stop patient breathing during needle insertions for up to 20–25 s time intervals [14] and advance the needle at a consistent phase of the respiratory cycle. However, this is primarily based on physician judgment and is highly variable. The problem of variability in determining a consistent phase of respiratory cycle becomes more relevant when the needle is held by a rigid device such as a robotic needle driver.

For robot-assisted needle insertion systems to be used in the clinical setting, they must overcome these safety issues. One solution is to use just a passive guide and have the physician insert the needle, as in the Neuromate [15] robotic system (Integrated Surgical Systems Inc., Davis, California, USA). At the other end of the spectrum is a fully active robotic system such as the Robodoc [16] (Integrated Surgical System Inc.) for total hip replacement. These robotic systems have addressed safety concerns, but only in clinical settings with predominantly rigid structures. Safety concerns for minimally invasive robot assisted needle insertions must take into account mobile soft tissue characteristics and dynamic tissue deformations common in non-rigid anatomy.

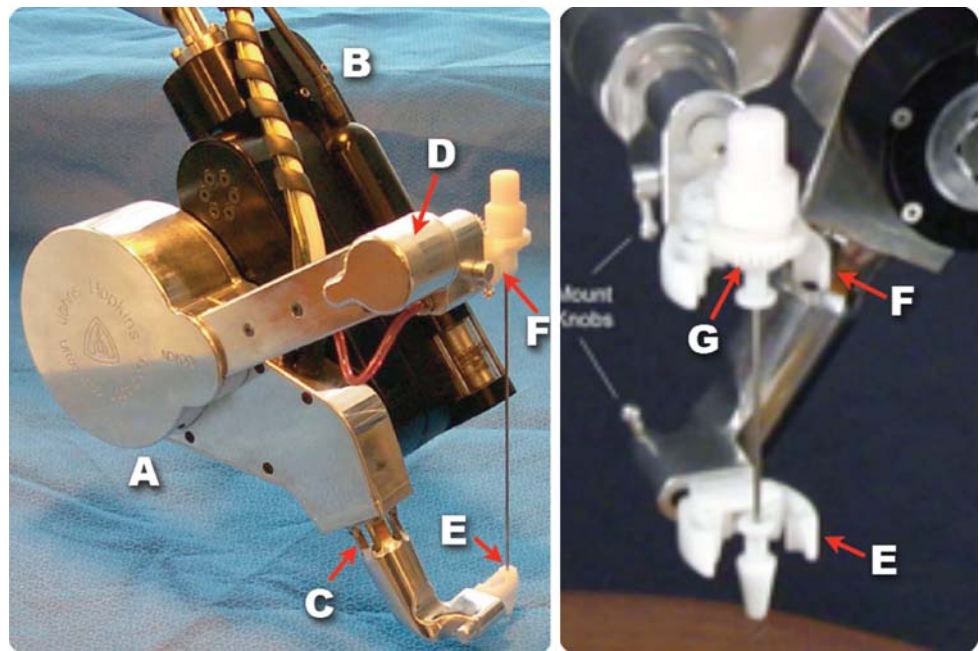
Tissue deformation and needle deflection are also effects which must be addressed for optimal robotic assistance. Frictional forces between the needle shaft and tissue are one of the causes of tissue deformation [17–19]. Some other factors that also affect tissue deformation include axial insertion rate and tip geometry. Force modeling has been applied to measure the stiffness, friction, and needle geometry effects during needle insertion in soft tissues [18,20]. Rotation of the needle during insertion has been explored by multiple groups [21,22] including ours, to reduce deformation and thereby decrease needle tip displacement. The effect of needle rotation during insertion has resulted in less tissue damage, indentation, and frictional forces. High-speed needle rotation in a robot assisted prostate brachytherapy system has also been shown to increase the accuracy of targeting in agar phantoms [22]. Such rotating needle driving systems may allow for more accurate needle insertions.

The aim of this paper is to evaluate the feasibility and safety capability of a new robotic-needle driving system in a swine model. The two updated mechanisms: (1) a quick release safety mechanism and (2) a rotating needle driver (RND) were evaluated by exploring the reliability of needle release and impact of spin on tissue deformation. The time to detect force overload and needle release was tested as a performance measure of the quick release safety mechanism. To test the impact of spin on tissue deformation, needle displacement and force values were compared for predetermined spin speeds. The capabilities of the robotic system demonstrated in this preclinical animal study can potentially be applied to a wide range of other needle-based, minimally invasive procedures.

Materials and methods

The robotic system used in these experiments is an updated version of the “AcuBot” system built by the Urology Robotics Laboratory at Johns Hopkins Medical Institutions [11,23]. The original AcuBot comprises the “PAKY” (Percutaneous Access of the KidneY) needle driver, the “RCM” (Remote

Fig. 1 *a* Rotating Needle Driver (RND), *b* Remote Center of Motion (RCM) orientation module. *c/d* Force sensor, *e/f* Head and Barrel grippers, *g* Needle hub



Center of Motion) orientation module, and joystick control. A three degree of freedom Cartesian stage, passive positioning S-arm, and “bridge frame” enable the system to achieve a compact and flexible design for interventions at multiple points along the body.

Prior experiences using the AcuBot system in clinical trials for spinal nerve blocks showed the need for some system enhancements [24]. The main focus of these enhancements was a complete redesign of the needle driver. Three new components were added to the needle driver: (1) a mechanism to spin the needle, (2) force sensors, and (3) a needle release mechanism. The updated system is referred to as the “AcuBot1 V2-RND” and shown in Fig. 1.

The compact RND holds the needle from two points for enhanced support and accurate insertions. This design prevents buckling of long thin needles. Moreover, it is capable of spinning the needle during insertion in either direction. Rotation of the needle may help to reduce the resistive forces by the “drilling effect.” Needle rotation may also be favorable by changing a higher static friction between tissue and needle to a lower kinetic friction thus reducing insertion forces.

One unique feature of the needle driver is the built-in force sensing capability. There is a custom force sensor built into the lower arm that holds the nozzle (Fig. 1). As can be seen in Fig. 2 the mechanical structure of the lower arm has been machined so that it will deflect very slightly when any force is applied to the nozzle holding the needle. Strain gages have been mounted on the lower arm to sense this deflection. Through a calibration process and calibration matrix, the output of these strain gages is converted into three orthogonal

forces at the nozzle tip. Therefore, this force sensing capability measures the interaction between the needle shaft and the surrounding tissue.

The needle driver can also measure the axial force along the needle. This force is calculated by sensing the torque applied to the mechanism driving the upper arm of the needle. This torque is then converted to a force along the needle direction by accounting for the kinematics of the drive train mechanism. There is some noise from friction in this measurement, but by pressing manually along the direction of the needle and observing the reported force, it has been observed that this capability provides a reasonable representation of the actual force.

A safety mechanism is also built into the needle driver to release the needle which can be triggered manually or upon a desired force level measured by the force sensors. The needle is quickly released from the two grippers, one at the head of the needle and one close to the skin as shown in Fig. 1. The gripper at the head of the needle controls the spin and inserts the needle while the second gripper, close to the skin, guides its direction. Both grippers were fabricated from Delrin plastic and were designed to include two finger-like arms which clip together to hold the needle and swing aside during release as shown in Fig. 1. These grippers are low cost and can be easily manufactured to accommodate standard needle sizes. They can be sterilized and are disposable.

Experiments to test the AcuBot1 V2-RND system were performed on domestic swine in a multi-modality interventional suite, specifically designed for translational and

Fig. 2 Custom force sensor built into the lower arm and based on strain gage readings as shown in the right hand figure. The darker colors indicate higher strains

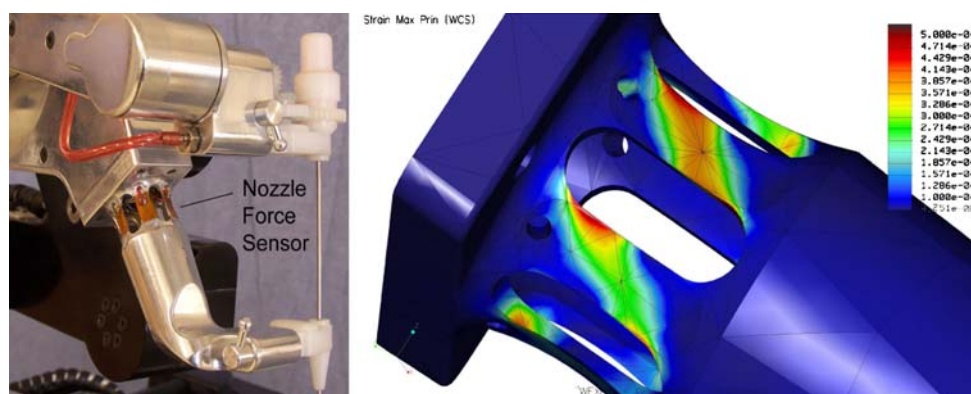
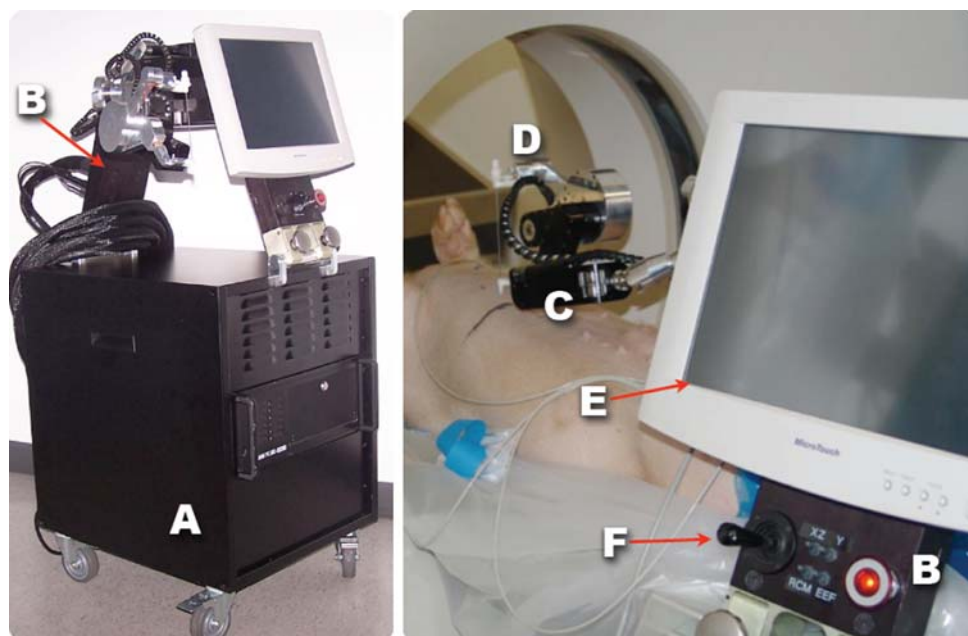


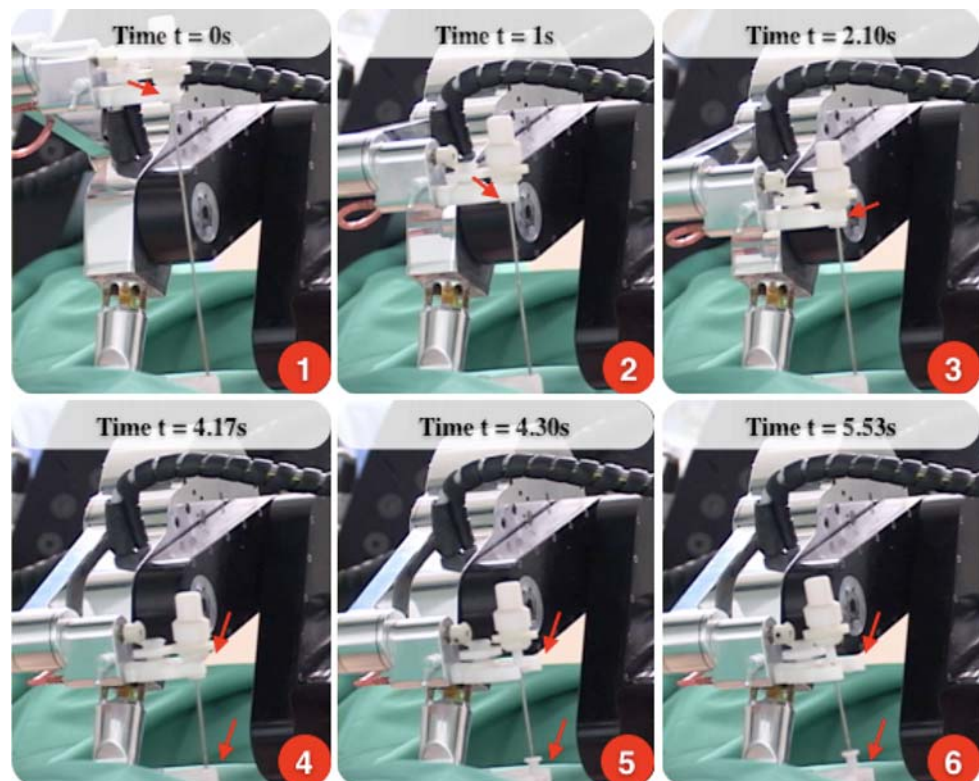
Fig. 3 *a* AcuBot1 V2-RND mounted on the control cabinet, *b* Custom “bridge frame”, *c* Needle driving unit, *d* Needle driver, *e* Computer system screen, *f* Joystick control



pre-clinical evaluation of image-guided devices. All animal care and use procedures were approved by the Institutional Animal Care and Use Committee. A domestic swine (100–125 lbs) was initially sedated with a mixture of ketamine, xylazine, telazol, and butorphanol, then intubated and maintained under general anesthesia with isoflurane. Once the animal was placed supine on the CT table, the AcuBot1 system was mounted onto the table using a custom designed mount and “bridge frame”, shown in Fig. 3a. Figure 3b shows the animal setup with the system positioned over the animal on the CT table. A preliminary CT scan was obtained to determine the location of the target in the liver. For each insertion, a different target and skin entry point were determined by the physician. The physician then marked the skin entry point on the pig. After proper securing of an 18 gauge 15 cm Diamond GREENE tip (COOK Biotech) needle within the needle driver, the robotic arm was positioned directly over the marked skin entry point.

The control parameters were then set to one of the three different rotation speeds: 0, 90, or 180 rpm. Other literature has published work with max spin values up to 2,000 rpm [25] however, for this system the maximum spin is 180 rpm. Thus, we chose this to be our maximum rotation speed and an intermediate rotation speed of 90 rpm was also selected. At each of these speeds 6, 7, and 3 needle insertions were performed respectively. A breakaway force magnitude was also selected so that needle release would always occur due to respiratory motion. This value was enough to accommodate respiratory forces but then releasing the needle at greater forces might cause laceration. The physician also created a small incision at the marked point to facilitate needle advancement. This is not a standard practice in the clinical setting. However, due to the thickness of porcine skin compared to human skin, this was necessary to allow the needle to be inserted. The pig's breath was held at the end of inspiration while the physician used the joystick to drive the needle towards the target.

Fig. 4 A sequence of images capture the insertion of the needle using the rotating needle driver, and the subsequent smooth, quick release of the needle at the end of insertion. 1–3 display of needle insertion, 4–5 beginning and end time of needle breakaway, 6 end of needle release



The control software of the robot then recorded the needle insertion depth and forces in the X , Y , and Z directions for analysis as described later.

Figure 4 shows a typical smooth, continuous insertion of the needle and its release after reaching the target, triggered by the sensed forces. Sequences 1–3 show the needle being inserted into the pig, while sequences 4 and 5 display the beginning and end time of complete needle release from the system. Alternatively, the release could also be manually triggered by the radiologist once the insertion is completed.

Results

A total of 16 insertions, 14 in liver and 2 in lung, were performed. The two lung insertions were performed to see if there was a difference with the needle driver performance between lung and liver. There was no significant difference in the two lung trials (insertions 15 and 16 in Fig. 5b) and the liver trials. Nonetheless, of these insertions 12 released completely upon the desired set force and four failed. Two of the four failures were released before reaching proper depth during insertion and two did not release at all. Needle release prior to achieving proper depth was due to the needle interaction with more compact tissue, specifically muscle. Though the experiments were not explicitly designed to evaluate sen-

sitivity of the force measures, these two failures suggest that the quick release mechanism should be adjusted to account for tissue variation based on CT image data. Other models to determine force profiles for this safety mechanism are being investigated. The other two failures that did not release were primarily due to excessive use and deterioration of the Delrin grippers. However, in the clinical setting, this would not be an issue because such low cost, easily manufactured parts can be disposed of after a certain number of insertions.

The response time of the quick release mechanism is also a crucial factor in ensuring safety during needle insertions. To determine the response time, we analyzed the norm of lateral forces (both x and y directions). The number of clock ticks between the controller detecting the pre-determined release threshold and the norm of the nozzle force falling below 0.1 N was recorded. The periodicity of the clock was 30 ms. Figure 5a shows a typical profile of the recorded nozzle force annotated with the start of needle release and instance when the needle is floating freely. Figure 5b displays the time between detection of a predetermined breakaway force and needle release. The mean for this measurement was 202 ± 39 ms.

A plot of the force versus needle displacement curve and average values of area under this curve with respect to needle rotation speed is shown in Fig. 6. Also shown in Fig. 6b are the maximum and minimum values for each of the spin rates.

Fig. 5 **a** A typical profile of nozzle force recorded by the strain gauges. **b** Time between breakaway force and needle release

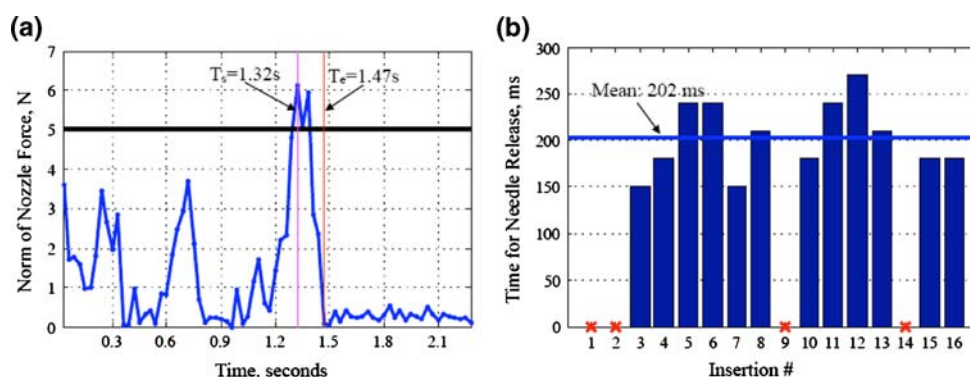
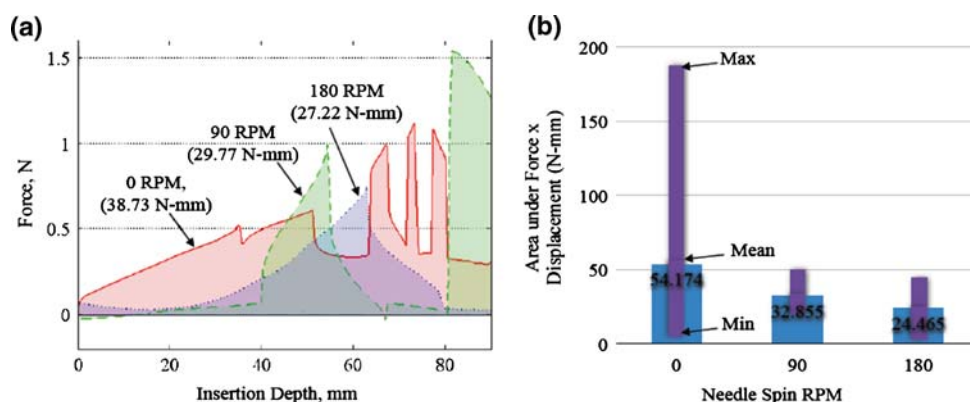


Fig. 6 **a** Force versus needle displacement curve, **b** Average areas under the Force versus Needle displacement curves of 12 successful insertions for three different spin rates. Thin bars represent the Range of values obtained for this metric



As seen, there is a marked reduction in the variability of this metric with rotation. This data shows the potential for needle rotation to reduce insertion force.

Discussion and conclusions

The effects of needle rotation and orientation reversal at half of the insertion depth have also been shown to increase the accuracy of targeting by other researchers [17,22]. This gain in accuracy has been shown to be due to reduced frictional forces between the needle shaft and the tissue. However, in in vivo animal models difficulties arise when measuring the contributions obtained from needle rotation, due to factors such as respiratory motion and organ movement. The effect of needle rotation is also likely to be related to tissue type, needle beveling and tip shape. Furthermore, the inhomogeneous mechanical properties of soft tissue make direct measurement of these frictional forces between the needle shaft and tissue complex and noisy as seen by the nozzle force sensor. Thus, to evaluate the effect of needle rotation we looked at the area under the force profile with respect to the needle insertion depth. The intuition behind this metric is that it can act as a proxy for the work done by the needle driver in inserting the needle. This measurement was collected at different points in the swine liver and values were averaged to reduce the effect of tissue inhomogeneity.

It has been suggested [21] that continuous rotation of the needle might cause more tissue damage as a result of defects in the shape of the needle. Our observations have been in line with this suggestion at high speeds, though not necessarily at lower speeds. However, our design provides two contact struts or points of support for the needle, one at the head and the second close to the skin entry point. This reduces the chance of buckling or deformation of the needle due to insertion forces.

In conclusion, a novel robotic needle driver was presented as applied to an in vivo swine model. The system was shown to be functional in a multimodality imaging clinical environment and provided a compatible workflow. The quick release safety mechanism of the system was demonstrated as a safety tool which may prevent tissue laceration and trauma, and could be a solution to a major hurdle facing active needle drivers for standard clinical practice in needle-based procedures. Safety mechanisms such as these are necessary for wider acceptance of robotic assistance in needle-based procedures. The response time for the quick release safety mechanism was sufficient for this proof of concept study. The RND may also provide an advantage by reducing tissue deformation and increasing the accuracy of needle targeting. Although the focus of this study was based on biopsy procedures, this robotic system can potentially be applied to a wide range of other needle-based minimally invasive procedures.

Acknowledgments Portions of this work were funded under NIH/NCI grant 5R33CA094274 and U.S. Army grant W81XWH-04-1-007, administered by the Telemedicine and Advanced Technology Research Center (TATRC), Fort Detrick, MD, USA. This research was also supported in part by the Intramural Research Program of the NIH.

References

1. Strasberg SM, Linehan D (2003) Radiofrequency ablation of liver tumors. *Curr Probl Surg* 40(8):459–498
2. Wood BJ, Locklin JK, Viswanathan A, Kruecker J, Haemmerich D, Cebal J, Sofer A, Cheng R, McCreedy E, Cleary K, McAuliffe MJ, Glossop N, Yanof J (2007) Technologies for guidance of radiofrequency ablation in the multimodality interventional suite of the future. *J Vasc Interv Radiol* 18:9–24
3. Wood BJ, Banovac F, Friedman M, Varro Z, Cleary K, Yanof J et al (2003) CT-integrated programmable robot for image-guided procedures: comparison of free-hand and robot-assisted techniques. *J Vasc Interv Radiol* 14:S62
4. Solomon SB, Patriciu A, Stoianovici DS (2006) Tumor ablation treatment planning coupled to robotic implementation: a feasibility study. *J Vasc Interv Radiol* 17(5):903–907
5. Fichtinger G, Fiene J, Kennedy CW, Kronreif G, Iordachita I, Song DY, Burdette EC, Kazanzides P (2007) Robotic assistance for ultrasound guided prostate brachytherapy. *Med Image Comput Assist Interv* 10(1):119–127
6. Stenzel R, Lin R, Cheng P, Kronreif G, Kornfeld M, Lindisch D, Wood BJ, Viswanathan A, Cleary K (2007) Precision instrument placement using a 4-dof robot with integrated fiducials for minimally invasive interventions. In: Cleary KR, Miga MI (Eds) *Proceedings of SPIE*. vol. 6509, no. 1. SPIE, 2007, p 65092S. <http://link.aip.org/link/?PSI/6509/65092S/1>
7. Kettenbach J, Kronreif G, Figl M, Fürst M, Birkfellner W, Hanel R, Ptacek W, Bergmann H (2005) Robot-assisted biopsy using computed tomography-guidance initial results from in vitro tests. *Invest Radiol* 40(4):219–228
8. Jantschke R, Haas T, Madoer P, Dziergwa S (2007) Preparation, assistance and imaging protocols for robotically assisted mr and ct-based procedures. *Minim Invasive Ther Allied Technol* 16(4):217–221
9. Hevezi J, Blough M, Hoffmeyer D, Yanof JH (2002) Brachytherapy using CT PinPoint. *MEDICAMUNDI* 46(3):22–27
10. Hata N, Hashimoto R, Tokuda J, Morikawa S (2005) Needle guiding robot for mr-guided microwave thermotherapy of liver tumor using motorized remote-center-of-motion constraint. In: *IEEE International Conference on Robotics and Automation*, pp 1652–1656
11. Cleary K, Melzer A, Watson V, Kronreif G, Stoianovici D (2006) Interventional robotic systems: applications and technology state-of-the-art. *Minim Invasive Ther Allied Technol* 15(2):101–113
12. Taylor RH (2006) A perspective on medical robotics. *Proc IEEE* 94(9):1652–1664
13. Muller SA, Maier-Hein L, Mehrabi A, Pianka F, Rietdorf U, Wolf I, Grenacher L, Richter G, Gutt CN, Schmidt J, Meinzer HP, Schmied BM (2007) Creation and establishment of a respiratory liver motion simulator for liver interventions. *Med Phys* 34(12):4605–4608
14. Riviere C, Thakral A, Iordachita II, Mitroi G, Stoianovici D (2001) Predicting respiratory motion for active canceling during percutaneous needle insertion. In: *Proc 23rd Annual Intl Conf IEEE Engineering in Medicine and Biology Society*, October, pp 3477–3480
15. Badano F, Danel F (1995) The NEURO-SKILL robot: a new approach for surgical robot development. In: *MRCAS*, pp 318–323
16. Kazanzides P, Mittelstadt BD, Musits BL, Bargar WL, Zuhars JF, Williamson B, Cain PW, Carbone EJ (1995) An integrated system for cementless hip replacement. *IEEE Eng Med Biol Mag* 14(3):307–313
17. Abolhassani N, Patel RV, Ayazi F (2007) Minimization of needle deflection in robot-assisted percutaneous therapy. *Int J Med Robot* 3(2):140–148
18. Okamura AM, Simone C, O’Leary MD (2004) Force modeling for needle insertion into soft tissue. *IEEE Trans Biomed Eng* 51(10):1707–1716
19. Nath S, Chen Z, Yue N, Trumpore S, Peschel R (2000) Dosimetric effects of needle divergence in prostate seed implant using 125I and 103Pd radioactive seeds. *Med Phys* 27(5):1058–1066
20. DiMaio SP, Salcudean SE (2005) Needle steering and motion planning in soft tissues. *IEEE Trans Biomed Eng* 52(6):965–974
21. Abolhassani N, Patel R, Moallem M (2004) Experimental study of robotic needle insertion in soft tissue. *Int Congr Ser CARS—Comput Assist Radiol Surg* 1268:797–802
22. Wei Z, Ding M, Downey D, Fenster A (2005) 3D TRUS guided robot assisted prostate brachytherapy. *Med Image Comput Comput Assist Interv* 8(2):17–24
23. Stoianovici D, Cleary K, Patriciu A, Mazilu D, Stanimir A, Craciunoiu N, Watson V, Kavoussi L (2003) Acubot: a robot for radiological interventions. *IEEE Trans Robot Autom* 19(5):927–930
24. Cleary K, Watson V, Lindisch D, Taylor RH, Fichtinger G, Xu S, WC S, Donlon J, Taylor M, Patriciu A, Mazilu D, Stoianovici D (2005) Precision placement of instruments for minimally invasive procedures using a “Needle Driver” robot”. *Int J Med Robot* 1(2):40–47
25. Neuenfeldt EM (2003) Method and device to reduce needle insertion force. U.S. Patent Number 6626848, Tech Rep

7.10 Wilson 2008: A buyer's guide to ...

Reprint begins on the next page and is 12 pages.

A Buyer's Guide to Electromagnetic Tracking Systems for Clinical Applications

Emmanuel Wilson, Ziv Yaniv, David Lindisch, Kevin Cleary

Imaging Science and Information Systems (ISIS) Center, Dept. of Radiology,
Georgetown University Medical Center, Washington, DC, USA

ABSTRACT

When choosing an Electromagnetic Tracking System (EMTS) for image-guided procedures, it is desirable for the system to be usable for different procedures and environments. Several factors influence this choice. To date, the only factors that have been studied extensively, are the accuracy and the susceptibility of electromagnetic tracking systems to distortions caused by ferromagnetic materials. In this paper we provide a holistic overview of the factors that should be taken into account when choosing an EMTS. These factors include: the system's refresh rate, the number of sensors that need to be tracked, the size of the navigated region, system interaction with the environment, can the sensors be embedded into the tools and provide the desired transformation data, and tracking accuracy and robustness. We evaluate the Aurora EMTS (Northern Digital Inc., Waterloo, Ontario, Canada) and the 3D Guidance EMTS with the flat-panel and the short-range field generators (Ascension Technology Corp., Burlington, Vermont, USA) in three clinical environments. We show that these systems are applicable to specific procedures or in specific environments, but that, no single system is currently optimal for all environments and procedures we evaluated.

Keywords: image-guided therapy, electromagnetic tracking, accuracy analysis, usability study

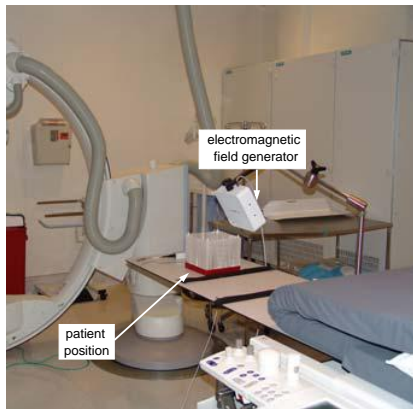
1. INTRODUCTION

To date Electromagnetic Tracking Systems (EMTS) evaluation has only focused on system accuracy and stability in the clinical environment.¹⁻³ In this paper we identify a comprehensive set of factors that influence the applicability of an EMTS in the clinical environment. We then evaluate two commercially available systems based on these factors as they pertain to several medical procedures.

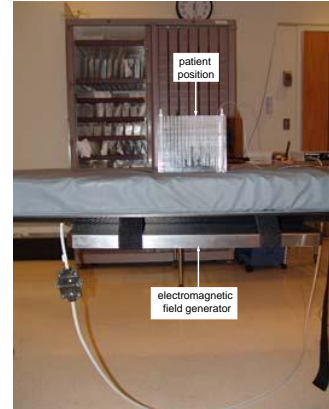
We have previously developed image-guidance systems based on electromagnetic tracking for a variety of procedures. These include Radio Frequency Ablation (RFA) of liver tumors,⁴ creation of a Transjugular Intrahepatic Portosystemic Shunt (TIPS),⁵ carotid stent deployment,⁶ vertebroplasty,⁷ needle biopsies of liver lesions,⁸ and transbronchial biopsies.⁹

These procedures are performed in three different environments: an interventional radiology suite, a CT suite, and a pulmonology suite (Figure 1). Our primary environment is the interventional radiology suite. It houses a floor mounted C-arm based cone-beam CT system, the Siemens Axiom Artis dFA, which provides both volumetric images and projection images. The first four procedures, RFA, TIPS, carotid stent deployment, and vertebroplasty, are performed in this room. They utilize tracked needles, catheters, and vertebroplasty trochars. The liver lesion biopsies are performed in the CT suite, and utilize needles. This suite houses a Siemens Somatom Volume Zoom CT machine that provides volumetric data and also real time single slice imaging, CT-fluoroscopy. Finally, the transbronchial biopsies are performed in the pulmonology suite, using biopsy forceps inserted through the flexible bronchoscope's working channel. The bronchoscope we use in this suite is the Pentax EB-1530T2. Figure 2 shows the various tools used in these procedures.

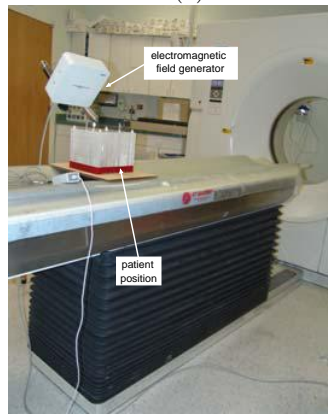
E-mail: {wilsone, zivy}@isis.georgetown.edu



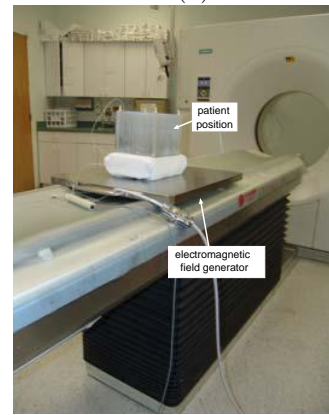
(a)



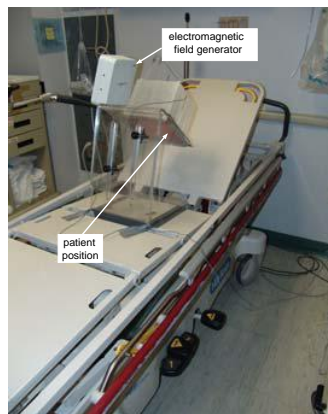
(b)



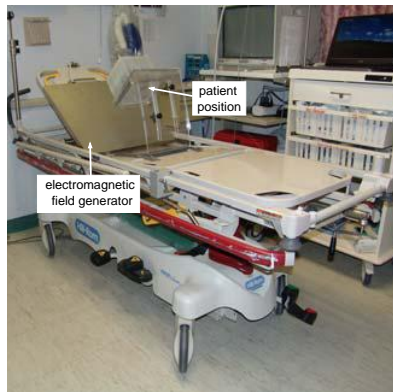
(c)



(d)



(e)



(f)

Figure 1. Setup of electromagnetic tracking systems in the interventional environments in which we assess their usability (a,b) interventional radiology suite, (c,d) CT suite, and (e,f) pulmonology suite. Left column shows the setup with the Aurora system. 3D Guidance short-range field generator setup is similar. Right column shows the setup with the 3D Guidance flat-panel field generator.



Figure 2. Tools used in the clinical procedures we study. From left to right, needle, catheter, vertebroplasty trochar, biopsy forceps.

Ideally, we would like to have a single EMTS that is applicable across procedures and environments. Based on the set of procedures enumerated above we define the following requirements from this ideal EMTS:

1. Speed: refresh rate of 100Hz with a latency of less than 1ms, regardless of the number of deployed sensors.
2. Concurrency: tracks up to 30 sensors concurrently (note that a flexible tool may contain multiple sensors).
3. Working volume: has an effective work volume of 5^3m (room sized).
4. Obtrusiveness: sensors are wireless and can function for several hours, all hardware components can be positioned so that they do not restrict the physical access to the patient, and the system does not have any effect on other devices used during the procedure.
5. Completeness: sensors are small enough to embed in any tool and provide all six degrees of freedom (6DOF sensors).
6. Accuracy: resolution less than $1mm$ and 0.1° .
7. Robustness: not affected by the environment (light, sound, ferromagnetic materials, etc.).

Having established the requirements from the ideal EMTS we are now ready to evaluate existing EMTS, based on the way they address these requirements.

As far as we are aware, there are only three vendors for stand-alone EMTS, Northern Digital Inc. (Waterloo, Ontario, Canada),¹⁰ Ascension Technology Corp. (Milton, Vermont, USA),¹¹ and Polhemus (Burlington, Vermont, USA).¹² In this study we evaluated the Aurora (Northern Digital Inc.), and 3D Guidance (Ascension Technology Corp.) systems. We did not evaluate any of the tracking systems from Polhemus, as the sensor size used by these systems is on the scale of several centimeters which precludes embedding them in any of the medical devices which we need to track.

2. MATERIALS AND METHODS

In this work we assess the Aurora and 3D Guidance EMTS. Both EMTS consist of three basic components, the field generator, a system control unit that interfaces with a PC, and tracked sensor coils and their respective interface to the system control unit. Note that the 3D Guidance system is evaluated in two configurations, using the flat-panel and the short-range field generators. Figure 3 shows the system components for both EMTS as used in this study.



Figure 3. Electromagnetic tracking systems and their components, as used in this study, (a) Aurora and (b) 3D Guidance.

From our prior experience with assessing the accuracy of electromagnetic tracking systems³ we have observed variable performance. We thus believe that, while electromagnetic tracking is a viable option for tracking in the clinical environment its applicability should be evaluated per environment, and even more specifically on a per procedure basis.

We thus evaluate each requirement with respect to the specific environments or procedures where relevant.

2.1. Speed

The maximal refresh rate for the Aurora system according to manufacturer specifications is 40Hz. We empirically evaluated this by acquiring time stamped measurements using a single five degree of freedom (5DOF) sensor. Data was acquired with a program developed in house using the system's API. The refresh rate we obtained was 39.86Hz which concurs with the manufacturer's specifications. When an additional 5DOF sensor was attached the refresh rate dropped to 20-25Hz. Attaching additional sensors after this initial decrease in refresh rate did not have any effect. For our purposes this refresh rate is just sufficient as our display is updated at 25-30Hz. System latency was not assessed quantitatively. We have qualitatively observed that it was not an issue in any of our image-guidance applications.

The maximal refresh rate for the 3D Guidance system according to manufacturer specifications is 160Hz with the flat-panel field generator and 375Hz with the short-range field generator. Interestingly, the factory default refresh rate, set for optimal accuracy, for the flat-panel field generator is about 40Hz and for the short-range field generator about 68Hz. We empirically evaluated the refresh rates both for the flat-panel and short-range field generators by acquiring time stamped measurements using six degree of freedom (6DOF) sensors. Data was acquired using a custom program from Ascension. The refresh rate we obtained for the flat-panel field generator was approximately 160Hz irrespective of the number of tracked sensors. The configuration with the short-range field generator was also unaffected by the number of tracked sensors, with an acquisition rate of 190Hz.

2.2. Concurrency

The Aurora system supports tracking of up to eight 5DOF sensors or four 6DOF sensors. The 3D guidance system supports tracking of up to 12 5DOF sensors and eight 6DOF sensors. For all of our applications we have found these numbers to be sufficient, as less than eight tracked tools are used at the same time.

2.3. Working volume

The Aurora system provides a working volume of $500 \times 500 \times 500$ mm. The 3D guidance system's working volume is dependent upon the electromagnetic field generator. With the flat-panel field generator the working volume is similar to the Aurora work volume. With the short-range field generator the work volume is

1000 × 1000 × 1000mm but manufacturer specifications state that optimal accuracy is limited to a sub-volume of approximately 200 × 200 × 200mm.

The work volume provided by the 3D Guidance short-range field generator will require special consideration when positioning it relative to the patient. For all of our procedures, except for carotid stent deployment a work volume of 500 × 500 × 500mm is sufficient. For carotid stent deployment the initial part of the navigation, starting at the femoral artery, was performed using the current clinical approach, and once the tracked volume was reached the physician was able to use our navigation system.

2.4. Obtrusiveness

As this requirement consists of several sub-categories it can be partially assessed independently from the procedure and environment. Both the Aurora and 3D Guidance systems are wired. That is, the tracked tools are connected via wires to the control unit. While this does not preclude any of the procedures we are investigating it does make them more cumbersome. More importantly, these additional wires require caution on the part of the medical staff when moving around the patient. If the procedure also involves moving imaging apparatus such as the rotating C-arm in the case of cone-beam CT, one must exercise caution in placing the wires as they are not an obstacle during navigation but they may be in the path of the rotating arm.

Interventional radiology suite

In all procedures performed in the interventional radiology suite the Aurora EMTS is placed such that the systems field generator is mounted on a passive mechanical arm positioned approximately 150mm from the patient (Figure 1(a)). This restricts physical access from certain directions but has not been a limiting factor in any of the procedures. The 3D Guidance system with the short-range field generator is positioned similarly. It is slightly less intrusive than the Aurora system due to the smaller form factor of the field generator. The 3D Guidance system with the flat-panel field generator does not change the physical access to the patient from current clinical practice, as the field generator is placed underneath the patient (Figure 1(b)).

In the RFA, TIPS and stent deployment procedures preoperative CT data is used for navigation and C-arm fluoroscopy is potentially used for intraoperative imaging, validating the information presented by the navigation system. The Aurora's field generator precludes imaging from certain C-arm poses. This is not a limiting factor as long as imaging and tracking are not required simultaneously, as the field generator can be easily moved out of the way. For the vertebroplasty procedure preoperative cone-beam CT data acquired with the C-arm is used for navigation. This requires additional care in positioning the field generator so that it is not in the path of the rotating C-arm. Again, this was found to be a minor inconvenience.

The 3D Guidance system with the short-range field generator is similar to the Aurora system. When configured with the flat-panel field generator we have found that because the field generator cannot be easily moved in and out of tracking position image quality is degraded. This was assessed by imaging an interventional 3D Abdominal Phantom (CIRS, Norfolk VA, USA). This phantom is composed of materials that mimic the X-ray attenuation of human tissue. We acquired both 2D projection images and a C-arm cone-beam CT reconstruction, with and without the flat-panel field generator in j

CT suite

In the needle biopsy procedures performed in the CT suite the Aurora EMTS is placed such that the system's field generator is mounted on a passive mechanical arm positioned approximately 150mm from the patient (Figure 1(c)). This restricts physical access to one side of the patient but has not been a limiting factor in this procedure as the mechanical arm and field generator are on the opposite side of the CT bed from the physician. As was the case in the interventional radiology suite, the 3D Guidance system with the short-range field generator is similar to the Aurora system. When using the flat-panel configuration, the field generator is placed underneath the patient (Figure 1(d)). This requires that the standard mattress be replaced with one which will support the patient. This is due to the shape of the patient couch, which is curved with the flat-panel field generator raising the patient above the bed. This will also cause problems with obese patients, as the effective bore size is reduced.

In the needle biopsy procedures there are two modes of imaging, acquisition of a preoperative CT scan and intraoperative CT fluoroscopy, real time single slice imaging. The Aurora and 3D Guidance with short-range field generator are not in the field of view when imaging and thus do not effect image quality. When using the

3D Guidance system with the flat-panel field generator the images always included the field generator as it is placed underneath the patient. We performed the same imaging experiment as in the interventional radiology suite, showing that the image quality was degraded by the field generator’s presence. Detailed results are given in section 3.

Pulmonology suite

In the transbronchial biopsy procedure the patient is lying on a stretcher at a 45° upright angle, with the mechanical arm holding the Aurora field generator attached to the stretcher’s rail (Figure 1(e)). This restricts physical access to one side of the patient. This is not a limiting factor as the physician stands on the opposite side of the stretcher facing the bronchoscopy monitor. Again, the 3D Guidance system with the short-range field generator was similar to the Aurora system, and the flat-panel field generator is unobtrusive as it is placed under the patient’s back (Figure 1(f)).

None of the systems caused any noticeable distortions of the video imaging.

2.5. Completeness

Both the Aurora and 3D Guidance system support 5DOF and 6DOF sensors. For the Aurora system the smallest 5(6)DOF sensors have a diameter of $0.55(1.8)mm$. For the 3D Guidance system the smallest 5(6)DOF sensors have a diameter of $0.3(1.3)mm$.

Interventional radiology suite

The tools that require tracking in our procedures are 18 gauge (diameter of $1.02mm$) needles for RFA, and TIPS, 22 gauge (diameter of $0.6mm$) needles for vertebroplasty, a catheter with a diameter of $2.3mm$ for stent deployment, and a vertebroplasty trochar with a diameter of $4.2mm$. All of these tools are similar in that they are used in a way that allows us to model them as cylinders. That is, the rotation around the tool axis is unimportant. This is why 5DOF sensors are sufficient for all of these procedures.

CT suite

The tools required for the biopsy procedures performed in the CT suite are 18 gauge needles as used in the procedures performed in the interventional radiology suite.

Pulmonology suite

The tool that we need to track for the transbronchial biopsy is a forcep that must fit through the bronchoscope’s working channel. In our case the working channel has a diameter of $2mm$, and the forceps have a sheath diameter of $1.8mm$. For this procedure we cannot use the same cylindrical model as done for other procedures. Navigation is performed using a preoperative CT in which a virtual camera is positioned in the same pose as the bronchoscope’s camera which is tracked relative to the forceps. The tracked forceps are thus required to provide all six degrees of freedom. As the unknown rotation around the sensor axis is similar to an unknown camera rotation around the view direction. While the 6DOF sensors are close to the sheath diameter it has been shown that it is possible to use a 5DOF sensor to perform the tracking in combination with video-to-CT registration to compensate for the unknown rotation.¹³

2.6. Accuracy

The accuracy of each system was evaluated using the protocol described in.³ A plexiglass phantom is used to acquire data measurements at 225 locations. At each location, 100 measurements are acquired and their average is used as the point’s coordinates. We also record the distance of each of these 100 samples from the EMTS origin and the range of the distance variability, reflecting the system’s stability. We then register the acquired point set to the phantom’s coordinate system using paired-point rigid registration and compute the distance between the known point location and the reported point location after it is transformed. For the distance variability data we report on the maximal variability range:

$$\max[\max\{d_i\}_j - \min\{d_i\}_j], \quad i = 1 \dots 100, \quad j = 1 \dots 225$$

where d_i is the distance from the EMTS origin to the i ’th point. For the registered point set data we provide the following descriptive statistics: RMS error, mean error, standard deviation, error range, maximal error and 95 percentile. This experiment was performed in each of the environments described in this paper. Detailed results are described in section 3.

2.7. Robustness

Interventional radiology suite

In the interventional radiology suite the device that is potentially most disruptive to electromagnetic tracking is the C-arm. To evaluate its effect on the stability of the tracking we performed the following experiment. We first placed two tracked sensors at an unknown fixed distance from each other. We then acquired data with the C-arm in its home position away from the patient and tracking systems. The C-arm was then moved into imaging position, and an image and tracking data were simultaneously acquired. Finally, we acquired tracking data during a cone-beam CT scan. For each of these data acquisitions we computed the distance between the two sensors based on their respective transformations. Detailed results are given in section 3.

CT suite

In the CT suite both the patient couch and CT gantry are potentially disruptive to electromagnetic tracking. Both these components are active while a CT scan is acquired. When CT fluoroscopy is used only the gantry rotates and the couch remains stationary. To evaluate the effect of these elements on the stability of the tracking we performed the following experiment. We first placed two tracked sensors at an unknown fixed distance from each other. We then acquired data at the spatial location where we expect to perform tracking, away from the gantry. This was followed by tracking data acquisition during CT fluoroscopy imaging, and finally tracking data acquisition while a CT scan was performed. For each of the data acquisitions we computed the distance between the two sensors based on their respective transformations. Detailed results are given in section 3.

Pulmonology suite

In the pulmonology suite the potentially problematic equipment is the patient's stretcher itself. In our institute the procedure is performed with the patient lying on the stretcher at an angle of 45° . Unlike the interventional radiology and CT suites where the patient couches are fixed, the stretcher model varies, as the procedure is performed on whichever stretcher the patient is being transported with. This may result in performance variability based on the stretcher type. In our case we tested with a single stretcher type, the Hill-Rom (Batesville, Indiana, USA) P8000 transport stretcher, and thus cannot provide comprehensive conclusions.

3. EXPERIMENTAL RESULTS

We now describe our experimental results with regard to the effect the EMTS have on imaging, and our accuracy and robustness evaluations of these systems.

3.1. Effect on imaging

To assess the effect of the electromagnetic tracking systems on imaging we acquired images while tracking. In the interventional radiology suite we acquired cone-beam CT and projection images, in the CT suite we acquired a CT scan and CT-fluoroscopy, and in the pulmonology suite we acquired video images.

In all suites the Aurora and 3D Guidance with short-range field generator had no noticeable effect on image quality, as they were easily moved away from the imaged region. The 3D Guidance with flat-panel field generator did result in a noticeable degradation in image quality when acquiring cone-beam CT data, projection X-ray images, CT-fluoroscopy and standard CT data. The main cause for the loss in image quality is the presence of the field generator in the imaged region. As these images are used in subjective interpretation of the anatomical structures, we cannot determine if the lower image quality precludes the use of the flat-panel field generator. This is left up to the physician's discretion. Figure 4 summarizes these experiments.

3.2. Accuracy

The accuracy of each of the tracking systems was evaluated as described above. The interventional radiology suite was found to be the optimal environment for tracking. This is the only environment that can be controlled so that the distortion of the EMTS magnetic field is minimal. The C-arm, which is a potential cause for distortion can be placed in its home position far from the patient. In addition, the region of the patient table over which the EMTS work volume is positioned is suspended in mid-air. Table 1 summarizes the accuracy evaluation in the interventional radiology suite. The 3D Guidance with short-range field generator was the most accurate in this environment, with the Aurora and 3D Guidance with flat-panel field generator having comparable accuracy.

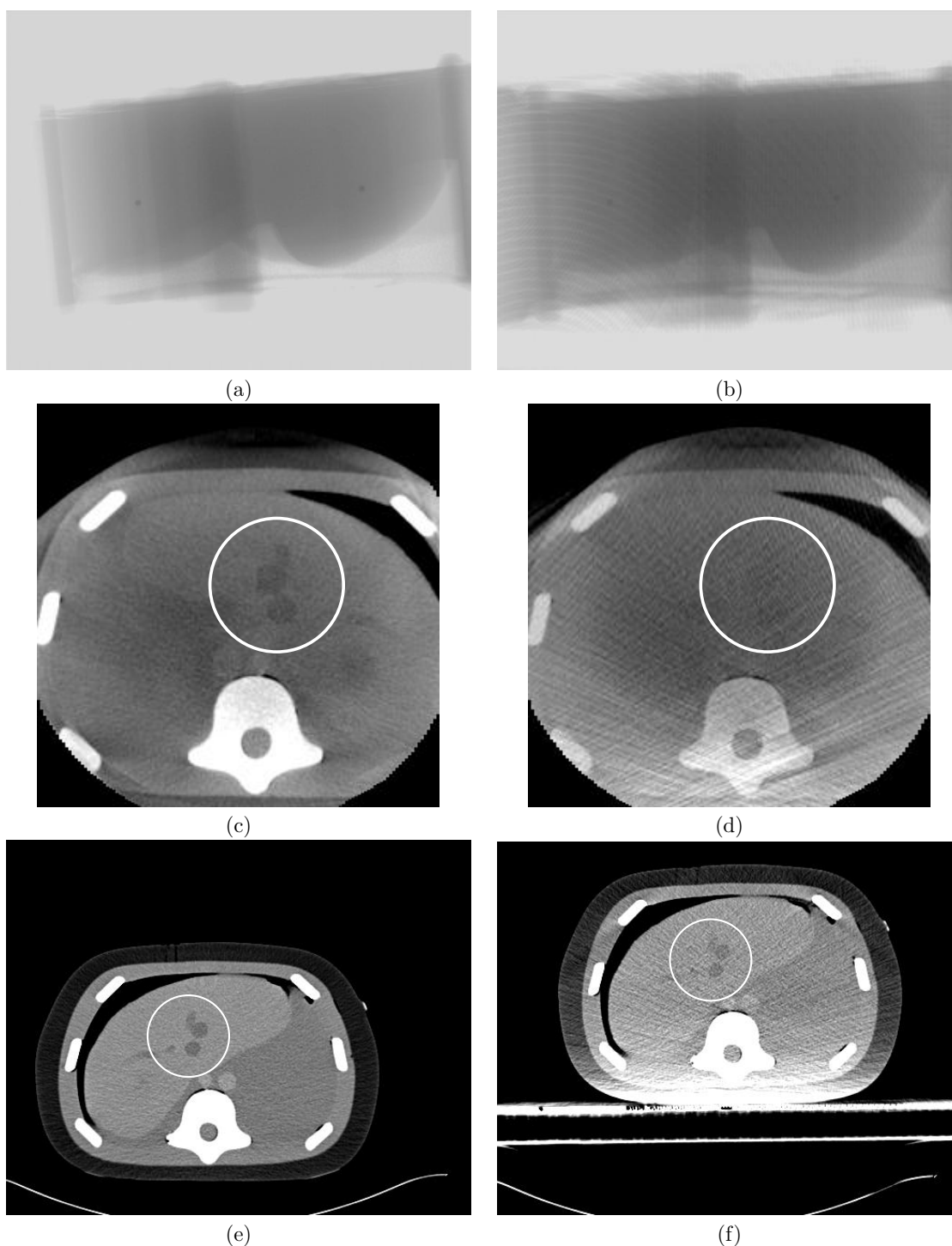


Figure 4. Effect of flat-panel field generator on image quality, all images are of the CIRS abdominal phantom. Notice deteriorated image quality in marked regions. (a,b) X-ray projection images without and with field generator. (c,d) Cone-beam CT axial slice without and with field generator. (e,f) CT axial slice without and with field generator. CT-fluoroscopy images were similar to images (e,f).

On the other hand the 3D Guidance with short-range field generator was the worst in terms of stability. That is, measurements fluctuated considerably but when averaged gave excellent accuracy.

	Aurora	3D Guidance short-range	3D Guidance flat-panel
maximal sample distance variability	0.26	4.48	0.67
RMS	1.01	0.38	0.77
mean	0.76	0.34	0.61
standard deviation	0.67	0.18	0.48
range	3.87	0.87	2.30
max	3.91	0.90	2.39
95 percentile	2.20	0.69	1.91

Table 1. Results of accuracy experiments in interventional radiology suite. All measurements are in millimeters.

In the CT suite there are two primary causes of electromagnetic distortion, the patient couch and the CT gantry. In practice, navigation is performed as far as possible from the CT gantry, so that the couch is the primary cause of distortion. Table 2 summarizes the accuracy evaluation in the CT suite. In this environment the 3D Guidance with flat-panel was the most accurate. Note that the main cause of the distortion is the couch mechanism that is underneath the field generator, which complies with the system’s assumptions. The 3D Guidance with short-range field generator and the Aurora system had comparable accuracy.

	Aurora	3D Guidance short-range	3D Guidance flat-panel
maximal sample distance variability	0.54	2.54	0.30
RMS	5.76	6.49	1.08
mean	5.14	5.67	1.02
standard deviation	2.62	3.17	0.36
range	18.33	17.34	1.76
max	19.24	18.14	1.96
95 percentile	10.83	12.29	1.56

Table 2. Results of accuracy experiments in CT suite. All measurements are in millimeters.

In the pulmonology suite the primary source of distortion is the patient stretcher. In our case we evaluated accuracy with the Hill-Rom (Batesville, Indiana, USA) P8000 transport stretcher. Table 3 summarizes the accuracy evaluation in the pulmonology suite. In this environment the Aurora and 3D Guidance with short-field generator were comparable and more accurate than the 3D Guidance with flat-panel field generator.

	Aurora	3D Guidance short-range	3D Guidance flat-panel
maximal sample distance variability	0.26	1.85	2.43
RMS	1.16	1.00	3.14
mean	0.95	0.89	2.78
standard deviation	0.67	0.45	1.46
range	5.70	3.76	10.02
max	5.83	3.92	10.40
95 percentile	2.19	1.54	5.78

Table 3. Results of accuracy experiments in pulmonology suite. All measurements are in millimeters.

3.3. Robustness

Robustness of the EMTS was evaluated in the CT and interventional radiology suites as described in section 2.7.

In the CT suite when acquiring data far from the gantry the mean(std) distance between the two tracked sensors for the Aurora system was 46.73(0.04)*mm*, for the 3D Guidance with flat-panel field generator the mean(std)

distance was $55.82(0.10)mm$ and with the short-range field generator $58.03(0.38)mm$. We then acquired tracking data during acquisition of a single CT-fluoroscopy image and during a CT scan. For the Aurora system 30% of the data was not reported for the single image case, and 93.4% of the data during the CT scan. Figure 5 summarizes the data acquired using the 3D Guidance system during single image acquisition and during a complete CT scan. Based on these results we conclude that all three systems cannot be used during image acquisition.

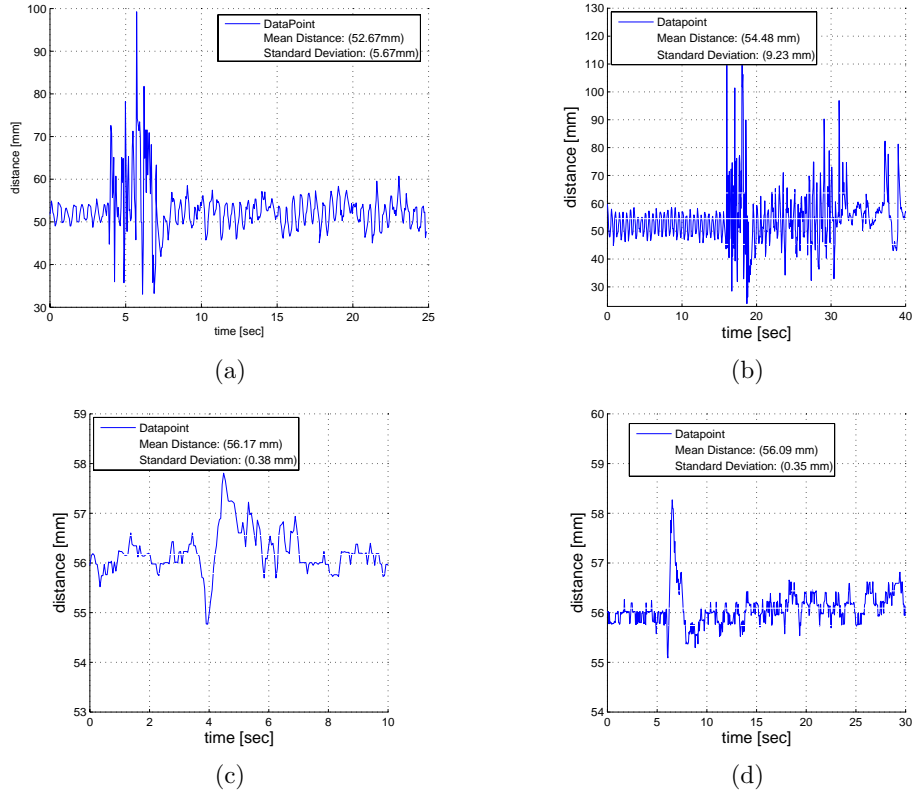


Figure 5. Distances between two fixed sensors during single CT-fluoroscopy image acquisition (left column) and during CT scan (right column). (a,b) 3D Guidance with short-range field generator, and (c,d) 3D Guidance with flat-panel field generator.

In the interventional radiology suite when acquiring data with the C-arm away from the tracking location the mean(std) distance between the two tracked sensors for the Aurora system was $21.84(0.06)mm$, for the 3D Guidance with flat-panel field generator the mean(std) distance was $52.28(0.12)mm$ and with the short-range field generator $52.63(0.61)mm$. Note that for each system the distance can be different as the sensors are placed in an arbitrary position. Figure 6 summarizes this experiment, with data for each of the systems as recorded during a single fluoroscopic image acquisition and during a rotation of the C-arm for cone-beam CT data acquisition. Based on our results we conclude that the Aurora and 3D Guidance system with short-range field generator should not be used in conjunction with imaging, and the 3D Guidance system with flat-panel field generator can be used during imaging, although it does have a detrimental effect on the images as described above.

4. DISCUSSION AND CONCLUSIONS

We have presented a holistic approach to evaluating electromagnetic tracking systems in the clinical environment that takes into account requirements beyond measurement accuracy.

In the past electromagnetic tracking system evaluation has focused on the system's accuracy and ability to deal with the presence of electromagnetic field distorting objects. This type of assessment is insufficient for the

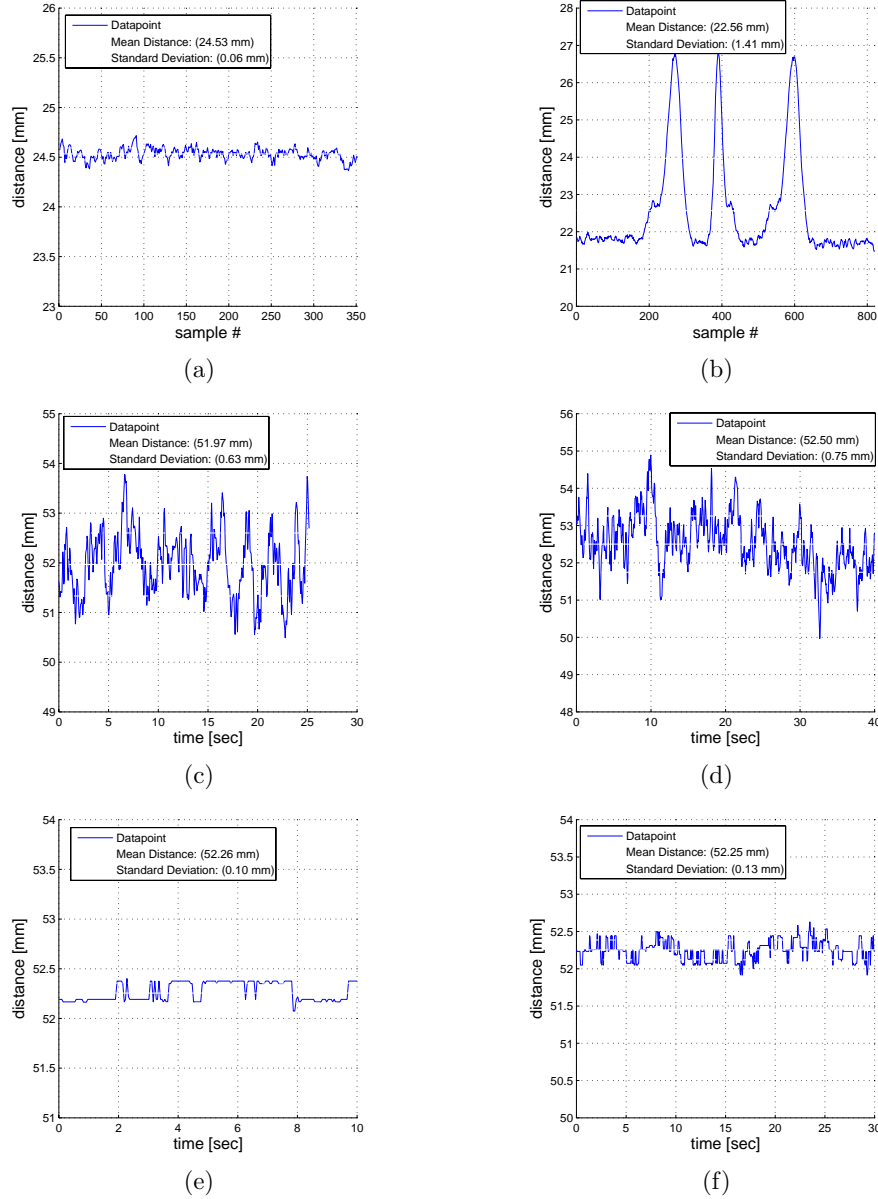


Figure 6. Distances between two fixed sensors during single X-ray image acquisition (left column) and during C-arm rotation for cone-beam CT data acquisition (right column). (a,b) Aurora system, (c,d) 3D Guidance with short-range field generator, and (e,f) 3D Guidance with flat-panel field generator.

clinical environment. For example, the 3D Guidance system using the flat-panel configuration was found to be the most accurate in the CT suite environment, but because it is placed underneath the patient it degrades the quality of the CT and CT-fluoroscopy images. Thus if accuracy were the only requirement this would be the system of choice. Given that imaging is at the heart of these interventions it is up to the physician to decide if the quality of the images is sufficient.

Based on our experience using electromagnetic tracking in the clinical environment we have compiled a comprehensive list of requirements. These requirements should be assessed on a per-procedure basis and include,

the system's refresh rate, the number of sensors that need to be tracked, the size of the navigated region, system interaction with the environment, can the sensors be embedded into the tools and provide the desired information (5DOF vs. 6DOF), and tracking accuracy and robustness in the specific interventional environment. We assessed the Aurora EMTS, and the 3D Guidance EMTS with short-range and flat-panel field generator configurations using these requirements. Each of the systems was found to have certain strengths and weaknesses, but none of them was optimal across environments and procedures.

ACKNOWLEDGMENTS

This work was funded by US Army grant W81XWH-04-1-0078. The content of this manuscript does not necessarily reflect the position or policy of the U.S. Government.

REFERENCES

1. J. B. Hummel, M. R. Bax, M. L. Figl, Y. Kang, C. R. Maurer, Jr., W. W. Birkfellner, H. Bergmann, and R. Shahidi, "Design and application of an assessment protocol for electromagnetic tracking systems," *Med. Phys.* **32**(7), pp. 2371–2379, 2005.
2. C. Nafis, V. Jensen, L. Beauregard, and P. Anderson, "Method for estimating dynamic EM tracking accuracy of surgical navigation tools," in *SPIE Medical Imaging: Visualization, Image-Guided Procedures, and Display*, pp. 61410K–1–61410K–16, 2006.
3. E. Wilson, Z. Yaniv, H. Zhang, C. Nafis, E. Shen, G. Shechter, A. D. Wiles, T. Peters, D. Lindisch, and K. Cleary, "A hardware and software protocol for the evaluation of electromagnetic tracker accuracy in the clinical environment: a multi-center study," in *SPIE Medical Imaging: Visualization, Image-Guided Procedures, and Display*, K. Cleary and M. Miga, eds., pp. 65092T–1–65092T–11, SPIE, 2007.
4. F. Banovac, J. Tang, S. Xu, D. Lindisch, H. Y. Chung, E. B. Levy, T. Chang, M. F. McCullough, Z. Yaniv, B. J. Wood, and K. Cleary, "Precision targeting of liver lesions using a novel electromagnetic navigation device in physiologic phantom and swine," *Med. Phys.* **32**(8), pp. 2698–2705, 2005.
5. E. B. Levy, J. Tang, D. Lindisch, N. Glossop, F. Banovac, and K. Cleary, "Implementation of an electromagnetic tracking system for accurate intrahepatic puncture needle guidance: Accuracy results in an in vitro model," *Academic Radiology* **14**(3), pp. 344–354, 2007.
6. F. Banovac, B. Wood, T. Popa, D. Lindisch, H. Zhang, K. Cleary, and N. Glossop, "Feasibility of carotid stent deployment in swine using an electromagnetic navigation device for catheter guidance," in *Proc. Computer Assisted Radiology and Surgery*, p. 1308, 2005.
7. J. Ding, N. Khan, P. Cheng, E. Wilson, V. Watson, K. Cleary, and Z. Yaniv, "Accuracy analysis of an image-guided system for vertebroplasty spinal therapy based on electromagnetic tracking of instruments," in *SPIE Medical Imaging: Visualization, Image-Guided Procedures, and Display*, 2008.
8. F. Banovac, E. Wilson, H. Zhang, and K. Cleary, "Needle biopsy of anatomically unfavorable liver lesions with an electromagnetic navigation assist device in a computed tomography environment," *Journal of Vascular and Interventional Radiology* **17**(10), pp. 1671–1675, 2006.
9. J. Choi, L. Gruionu, T. Popa, E. Anderson, and K. Cleary, "Transbronchial biopsy based on electromagnetic tracked biopsy forceps," *Int. J. Computer Assisted Radiology and Surgery* **2**(Suppl. 1), pp. S143–S145, 2007.
10. <http://www.ndigital.com/>, Northern Digital Inc. (Waterloo, Ontario, Canada), accessed January 8, 2008.
11. <http://www.ascension-tech.com/>, Ascension Technology Corporation (Milton, Vermont, USA), accessed January 8, 2008.
12. <http://www.polhemus.com/>, Polhemus (Burlington, Vermont, USA), accessed January 8, 2008.
13. K. Mori, D. Deguchi, K. Akiyama, T. Kitasaka, C. R. M. Jr., Y. Suenaga, H. Takabatake, M. Mori, and H. Natori, "Hybrid bronchoscope tracking using a magnetic tracking sensor and image registration," in *Medical Image Computing and Computer-Assisted Intervention*, pp. 543–550, 2005.

7.11 Wong 2007: PET/CT-guided interventional ...

Reprint begins on the next page and is two pages.

PET/CT-guided interventional procedures: rationale, justification, initial study, and research plan

Kenneth Wong^a, Sara Petrillo^b, Filip Banovac^{a,b}, Joseph Rahill^a, Elliot Levy^{a,b}, Raj Shekhar^c, David Earl-Graef^b, Kevin Cleary^a

^aComputer Aided Interventions and Medical Robotics (CAIMR), Imaging Science & Information Systems (ISIS) Center, Department of Radiology, Georgetown University Medical Center, Washington, DC, USA

^bDepartment of Radiology, Georgetown University Hospital / MedStar Health, Washington, DC, USA

^cDepartment of Radiology, University of Maryland Medical Center, Baltimore, MD, USA

Abstract Positron-emission tomography (PET) and PET/CT (computed tomography) are becoming increasingly important for diagnosis and treatment of cancer. Clinically relevant changes can sometimes be seen on PET that are not seen on other imaging modalities. However, PET is not suitable for guiding biopsy as the images are not obtained in real-time. Therefore, our research group has begun developing a concept for PET/CT-guided interventional procedures. This paper presents the rationale for this concept, outlines our research plan, and includes an initial study to evaluate the relative sensitivity of CT and PET/CT in detecting suspicious lesions.

Keywords PET · PET/CT · Image guidance · Cancer · Interventional procedures

1. Introduction

In recent years, PET (positron-emission tomography) and PET/CT (computed tomography) have become important tools in cancer management and treatment [2]. PET can provide information on functional or metabolic characteristics of tumors, whereas CT and MRI (magnetic resonance imaging) predominately assess the tumor's anatomical and morphological features, such as density, size, and shape. PET can sometimes detect clinically relevant changes that are not seen on CT or MRI.

Given this rising importance of PET imaging in the staging of cancer, our research group has begun to develop a methodology for PET-guided interventional procedures. Our goal is to combine respiratory corrected PET images with rotational angiography images in the interventional suite for precision image-guided biopsy. This paper describes some of our initial work in this area, including some background on image-guided biopsy, example images, and an initial study of the sensitivity of CT alone versus PET/CT for detecting malignant lesions.

2. Methods

2.1. Image-guided biopsy

Although biopsy remains the gold standard for diagnosis and identification of disease, it still has several key limitations. First, tumors can often be heterogeneous in composition, requiring multiple sampling attempts to get sufficient tissue for pathological evaluation. Second, as tumors are being detected at earlier and earlier stages, the biopsy needle must hit smaller and smaller targets, which can be quite challenging when directing a percutaneous needle. Third, percutaneous biopsy is often performed using solely X-ray guidance, which is limited to showing structural details of the anatomy such as bones, organ boundaries, and the

circulatory system. Finally, even when a diagnostic PET/CT is available, it is typically only available on a separate computer workstation, forcing the physician to mentally integrate and register the images. Although many physicians are quite skilled at this process, it is challenging and potentially subject to significant errors, as shown in Fig. 1 below.

2.2. Minimally invasive tumor ablation therapies

Minimally invasive therapies, particularly radiofrequency ablation (RFA), are seeing increasing use because of their ability to treat tumors effectively with minimal side effects and relatively short recovery times [1, 3, 4]. Certain populations of patients, such as those for whom open surgery is contraindicated, may find that a minimally invasive approach is their only treatment option. PET-guided interventional radiology is an ideal technology partner for minimally invasive therapy. Minimally invasive therapy allows physicians to precisely target small regions of the anatomy, and PET images provide the information necessary to treat only the functionally active lesion.

It is well known that tumors are heterogeneous and that the different regions of the tumor are often not readily apparent on structural imaging such as CT or MRI. Based on our clinical experience, we can immediately identify two strong impacts of PET-guided interventional radiology therapies. First, as tumors outgrow their blood supply, portions of the tumor may become necrotic. PET information would be useful to identify the viable fraction of specific tumor(s) for targeted therapy. Second, many tumors respond partially to chemotherapy, so PET imaging would be useful to identify chemo-resistant tumor tissue for second-line or salvage therapy using a minimally invasive approach.

2.3. Challenges to combining PET/CT and interventional radiology

Despite the significant capabilities of PET/CT imaging, clinically viable solutions for PET-guided interventional radiology have not yet been developed. Obviously, the most direct method for accomplishing PET guided interventional radiology would be to perform the intervention with the patient on the PET/CT scanner table. Our clinical partners at Georgetown University Hospital have in fact done a small number of biopsy procedures on our current scanner. However, this early work has uncovered several reasons why this solution is impractical and unlikely to be widely implemented.

1. PET and CT scanners are designed for producing diagnostic snapshot images of a patient, rather than the sustained real time imaging required for image guidance.

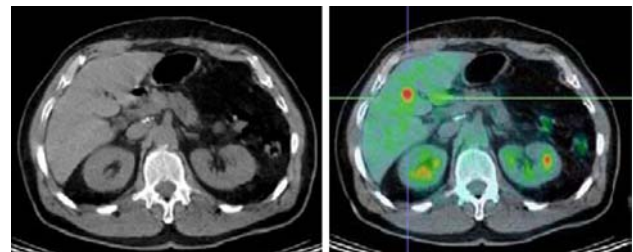


Fig. 1 CT image (*left*) and PET/CT fused image (*right*). With CT alone, the tumor in the liver is inconspicuous, but with PET/CT the tumor is easily seen as the bright red spot indicated by the crosshairs (there is also a second lesion in the kidney at lower right on the PET/CT image). These images clearly illustrate the challenge of attempting image-guided biopsy using only CT or X-ray fluoroscopy for navigation

2. Images from the PET/CT scanner are displayed on workstations located outside the room with the scanner itself, so using these workstations for guidance involves a lot of tedious movement back and forth from the patient table to the display workstation.
3. Infrastructure requirements for an interventional radiology suite (e.g., a large number of complex instruments and the ability to maintain a sterile field around the patient) are very different from those of a CT scanner suite, necessitating either a duplication of equipment or laborious relocation of that equipment during procedures.
4. Even on CT systems that support a fluoroscopic mode, the utilization time for interventions remains a major financial impediment. The time required for a successful intervention (including setup, the procedure, and cleanup) can extend into multiple hours, and therefore significantly decreases the normal billable imaging time for the system.

2.4. Clinical rationale and preliminary study

To investigate the clinical rationale for developing this system, we completed a preliminary study to evaluate the relative sensitivity of CT and PET/CT in detecting lesions suspicious for malignancy in whole body studies. A retrospective analysis of 53 consecutive whole body FDG PET/CT studies with a total of 164 lesions was completed. Negative studies and studies with only head or neck findings were excluded. A single reader retrospectively analyzed first the CT data alone, then the fused PET/CT images. PET positive lesions were categorized based on CT appearance in relation to possible malignancy. Six categories of CT findings were defined. Grade 0: no lesion on CT; grade 1: benign-appearing lesion on CT; grade 2: suspicious lesion on CT; grade 3: definite malignancy on CT; grade R/0: benign appearing CT lesion seen only in retrospect; grade R/1: suspicious appearing CT lesion seen only in retrospect. Grade 0, 1, R/0 and R/1 were classified as “discordant,” in that the CT data alone did not identify a PET/CT positive lesion.

3. Results

Of the 164 reviewed lesions, the total discordant number is 68, or 41.5%. Of the 42 grade 0 lesions (25.6% of the total), 16 were located in bone, 12 lymph nodes, 6 soft tissues, 3 gastrointestinal track, and 1 each in the breast, lung, vulva, cervix, and prostate. Of the 18 grade 1 lesions (11.0% of the total), 7 were located in lymph nodes, 4 soft tissues, and 1 each in both lung and bone. Of the 6 R/0 lesions (3.7% of the total), 2 were located in the lung, and 1 in each the liver, lymph node, pelvic mass, and soft tissue. Of the 4 R/1 lesions (2.4% of the total), 2 were located in the lung, and one in each the rectum and bone. There were also 30 grade 2

lesions (18.3% of the total), and 62 grade 3 lesions (37.8% of the total).

The conclusion of the preliminary study was thus that CT alone underestimates 41.5% of PET/CT positive cases of whole body scans for the detection of malignancy. Soft tissue and lymph node lesions were the lesions most likely to be missed by CT alone.

4. Conclusions and summary

Considering these potential applications and the challenges posed by the existing state-of-the-art, we believe that the best course is to devise a means for integrating the PET/CT information into the interventional radiology workspace. This approach allows us to optimize the acquisition of PET/CT images and the actual intervention on the patient separately, thereby avoiding the compromises required by trying to perform all of these procedures on a single piece of equipment.

Our work will provide accurate registration of the PET/CT images into the interventional radiology coordinate system, making the functional data readily accessible at the time of the intervention. In summary, this project will combine leading-edge technologies in PET/CT, image registration, and interventional radiology to address the pressing clinical needs of image-guided biopsy and minimally invasive therapies.

Acknowledgments

This work was funded by US Army grant W81XWH-04-1-0078 and administered by the Telemedicine and Advanced Technology Research Center (TATRC), Fort Detrick, Maryland, USA. The content of this manuscript does not necessarily reflect the position or policy of the US Government. This study was also supported in part by the Intramural Research Program of the NIH.

References

1. Brown DB (2005) Concepts, considerations, and concerns on the cutting edge of radiofrequency ablation. *J Vasc Interv Radiol* 16(5):597–613
2. Juweid ME, Cheson BD (2006) Positron-emission tomography and assessment of cancer therapy. *N Engl J Med* 354(5):496–507
3. Lencioni R, Della Pina C et al (2005) Percutaneous image-guided radiofrequency ablation in the therapeutic management of hepatocellular carcinoma. *Abdom Imaging* 30(4):401–408
4. Sutherland LM, Williams JA et al (2006) Radiofrequency ablation of liver tumors: a systematic review. *Arch Surg* 141(2):181–190